UNIVERSITY OF CALIFORNIA

Los Angeles

Numerical Simulations of the Mechanics of Vitrectomy

A dissertation submitted in partial satisfaction of the
requirements for the degree Doctor of Philosophy
in Biomedical Engineering

by

Ethan Keane Young

2015

ABSTRACT OF THE DISSERTATION

Numerical Simulations of the Mechanics of Vitrectomy

by

Ethan Keane Young

Doctor of Philosophy in Biomedical Engineering

University of California, Los Angeles, 2015

Professor Jeffrey D. Eldredge, Chair

Vitreous is the clear, gel-like substance that fills the cavity between the lens and retina in the eye. Treating certain eye abnormalities requires removing this substance using a minimally-invasive device called a vitreous cutter. Understanding the behavior of this viscoelastic biofluid during surgeries is essential to improving the effectiveness of the procedure. In this study, three-dimensional computational models of vitreous cutters are investigated using an immersed boundary method paired with a viscoelastic constitutive model. The solver uses a fractional-step method to satisfy continuity and traction boundary conditions to simulate the applied suction. The current work extends previous efforts to accurately model the rheological parameters measured by Sharif-Kashani et

al. using the Giesekus constitutive equation [Retina, 2013]. The simulations were used to quantify both the average and time-varying flow rate through the device. Values for flow rate are compared with experimental results from Hubschman et al. [Retina, 2009]. Flow features associated with the cutting dynamics are of particular interest, as is the geometry of the cutter itself. These operational and design changes are a target for improving cutter efficacy while minimizing potential tissue damage.

The dissertation of Ethan Keane Young is approved.

Jean-Pierre Hubschman

Pirouz Kavehpour

Dino Di Carlo

Jeffrey D. Eldredge, Committee Chair

University of California, Los Angeles

2015

In honor of my little brother,

who I miss every day.

Contents

List of Figures

List of Tables

Biographical Sketch

Ethan is currently a Ph.D. candidate in the department of Bioengineering at the University of California, Los Angeles. He received his Bachelor of Science in Mechanical Engineering from Kansas State University in 2009. In 2010, he received his Master of Science in Biomedical Engineering from the University of California, Los Angeles.

His research is conducted in the Simulation of Flow Physics and Acoustics Laboratory, a part of the Mechanical and Aerospace Engineering Department, under the direction of Professor Jeffrey D. Eldredge. His research area is computational fluid dynamics, with a particular interest in exploring biomedical flows and devices.

Chapter 1

Introduction

1.1 Background

1.1.1 Eye Anatomy and Physiology

The human eye is a slightly irregular hollow sphere, as shown in the Figure 1.1 cross-section. Its cavities are filled with fluids called humors that, among other things, help the eye maintain its shape. The lens, the adjustable focusing apparatus of the eye, is supported vertically within the organ, dividing it into anterior (toward the front of the body) and posterior (toward the back of the body) cavities.

Filling the posterior cavity between the lens and retina is a clear, gel-like substance known as vitreous humor, often simply referred to as vitreous. As noted earlier, the primary function of this fluid is to maintain the shape of the eye. Specifically, this

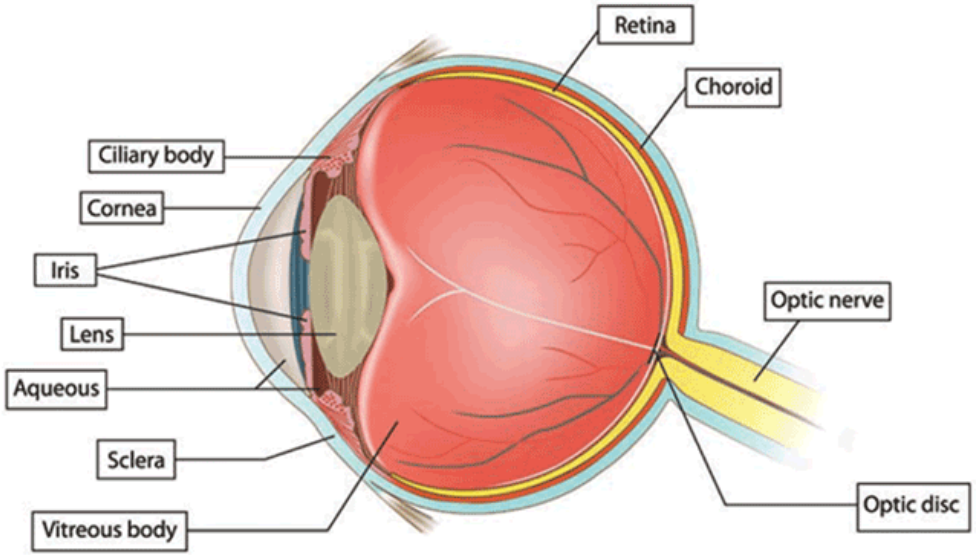

Figure 1.1: Illustrated cross section of the eye, highlighting the major internal structures [1].

means that the vitreous is responsible for supporting the posterior surface of the lens and holding the retina firmly against the interior eyeball surface. Light must be allowed to pass freely between the lens and retina, so the vitreous must also be perfectly clear while providing this support. The vitreous also contributes to intraocular pressure, which counteracts the pulling forces of muscles attached to the outer surface of the eyeball responsible for eye movement [33].

The treatment of certain eye abnormalities necessitates the removal of the vitreous, in a surgical procedure called a vitrectomy. Generally speaking, a vitrectomy is appropriate when a procedure requires access to the posterior cavity of the eye or when the vitreous suffers a reduction in its ability to permit the passage of light. Common indications include:

- Vitreous Hemorrhage
- Retinal Detachment
- Epiretinal Membrane
- Macular Hole
- Proliferative Vitreoretinopathy
- Endophthalmitis
- Intraocular Foreign Body Removal

Performing a successful vitrectomy requires an understanding of the nature of this gel-like fluid, which is introduced in the following section.

1.1.2 Vitreous

As noted in Section 1.1.1, the vitreous fulfills an essential mechanical function in the physiology of healthy eyes. Its role as a structural support is evident in its gel-like consistency, which is the result of a macromolecular, hydrated network [48]. Vitreous is composed almost entirely of water—99% by weight. The remainder is comprised of salts, heterotypic collagen fibrils (type II, V/XI, and IX), and a hyaluronan network [48]. This complex organization is illustrated in Figure 1.2.

It is the presence of the collagen and hyaluronan molecules that gives vitreous its viscoelastic properties and complicates its removal [48]. As a viscoelastic material, vitreous

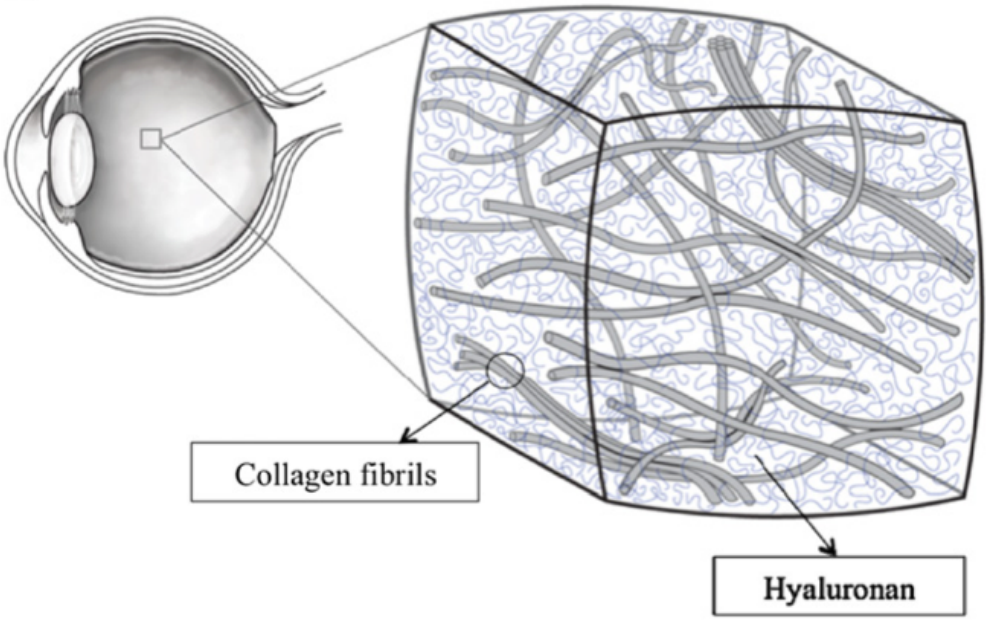

Figure 1.2: Illustration of the macromolecular composition of vitreous [48].

exhibits both an elastic and a viscous response when subjected to stress. More will be said about this dual-natured behavior in Section 2.3.1. In order to perform a vitrectomy, the collagen macromolecules must be severed or somehow fragmented, which diminishes the elastic nature of the vitreous and produces a "chopped" consistency that behaves more like a liquid. This liquid-like substance can then be smoothly suctioned out of the eye.

The notion of fragmenting vitreous to aid in its removal has been developed and refined over the years since the very first vitrectomies were performed. The history and continual refinement of the procedure will be developed in the following sections.

1.2 Vitrectomy

1.2.1 Early Development of Tools and Technique

During the late 1960s, Kasner began developing his technique to surgically remove vitreous from the eye to treat patients with opacification of the vitreous due to amyloidosis [26]. Kasner's so-called "open sky" technique began with a large incision and the folding back of an anterior section of the cornea. Through this incision, the lens itself could be extracted, allowing access to the vitreous in the posterior segment of the eye. The occluded vitreous was drawn out using forceps, which were later replaced with surgical sponges, and severed from the bulk with scissors. A diagram of Kasner's open sky vitrectomy technique is shown in Figure 1.3.

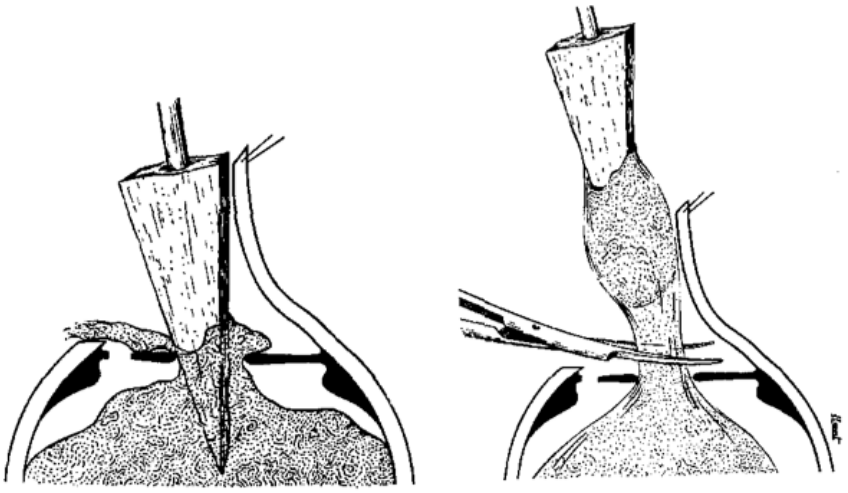

Figure 1.3: Illustration of Kasner's "open sky" technique for vitrectomy [32].

This technique was not without its shortcomings. Accessing the vitreous in the posterior

cavity through the pupil as shown in Figure 1.3 caused considerable irritation of the surrounding iris, as the pupil was often too small and required incisions to expand the working area. After observing Kasner's technique, Machemer began wondering how it could be improved; specifically, if replacing large instruments like the surgical sponge and scissors with smaller tools could reduce damage to the iris.

Machemer's first idea for such a surgical tool came in 1969, when he envisioned a spinning drill bit enclosed in a stationary tube such that only the tip of the drill bit was exposed. He hypothesized that the spinning tip would be sufficient to cut the vitreous, which would then be transported up through the fluted shaft. *In vitro* testing with egg white showed that, indeed, the drill bit could both cut and draw fluid up through the enclosure tube. Construction on a prototype device began shortly after this preliminary result. The main components of the prototype were a blunted hypodermic needle and small drill bit. The stationary hypodermic needle enclosed the rotating drill bit, with only a small portion at the tip left exposed. The drill bit was driven with a small electric motor housed in the plastic body of the syringe. Testing the vitreous cutter on rabbit eyes led to further design improvements, such as adding suction on the proximal (relative to the operator) end to more quickly remove the vitreous and adjusting the aperture through which the drill bit was exposed to the surrounding fluid. The various elements, and the final assembly, are shown in Figure 1.4 [32].

For the first time, the large sponge and scissors of Kasner's technique were replaced with a single tool, allowing the surgeon to simultaneously grab and cut vitreous. In

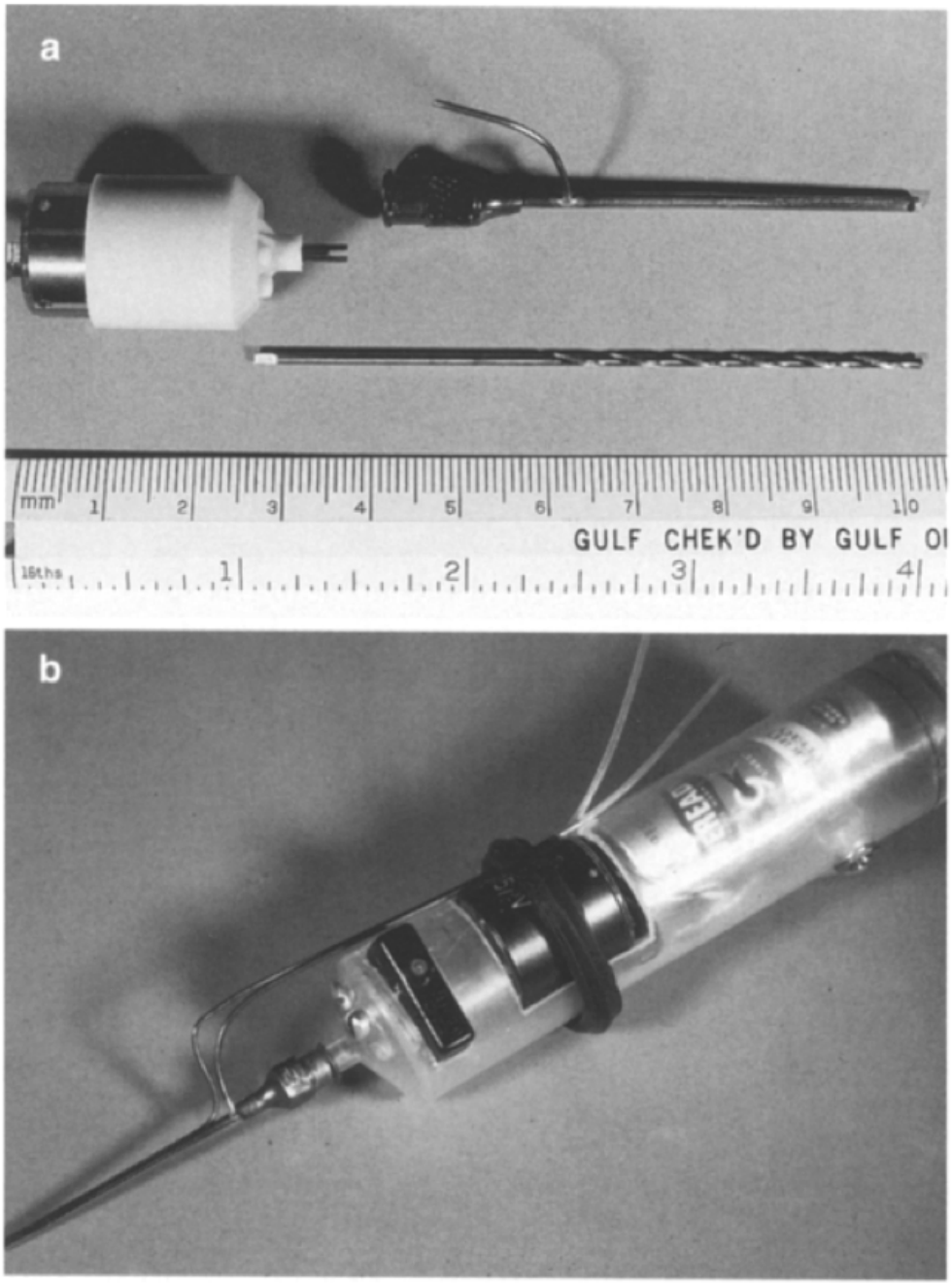

Figure 1.4: (a.) The motor, drill bit, and hypodermic needle of Machemer's first vitreous cutter (b.) the assembled tool with its plastic syringe housing [32].

early 1970, Machemer's tool was ready for human testing. After surgery, the patient's eye showed less irritation than similar eyes treated with the open sky technique [32]. At this point, the surgery was still performed by folding back an anterior section of the cornea, removing the lens, and operating the device through the pupil, being careful not to unnecessarily irritate the iris. Machemer wondered if it would be possible to perform the surgery by entering the eye through the pars plana, near the region where the iris meets the sclera (see Figure 1.1). Having experimented with this approach in primate models, Machemer was confident that vitrectomy could be performed in humans through a pars plana approach [32].

The first pars plana vitrectomy (PPV) was performed in 1970 to clear a vitreous hemorrhage from a diabetic patient. The surgery was completed without complication, and the patient improved his visual acuity from 2/200 to 20/50 [32]. As PPV continued to mature, the list of patients expanded to include those with problems previously deemed incurable, such as retinal detachment and so-called "giant" retinal tears [32, 30].

With the PPV technique gaining higher adoption rates, the focus again shifted to improving cutter design. Working with Parel, Machemer replaced the still relatively crude drill bit and hypodermic needle enclosure with a stationary 17-gauge (1.5 mm) outer tube and a rotating inner tube. Both tubes included a single lateral orifice such that the rotation of the inner tube caused the aspiration port to slide smoothly between open and closed states. When the holes were aligned, suction would draw vitreous through the tube and out of the eye. Further rotation of the inner tube would cause the inner

and outer wall to shear past each other, producing a scissor-like cutting action. This improved cutting design is shown in Figure 1.5

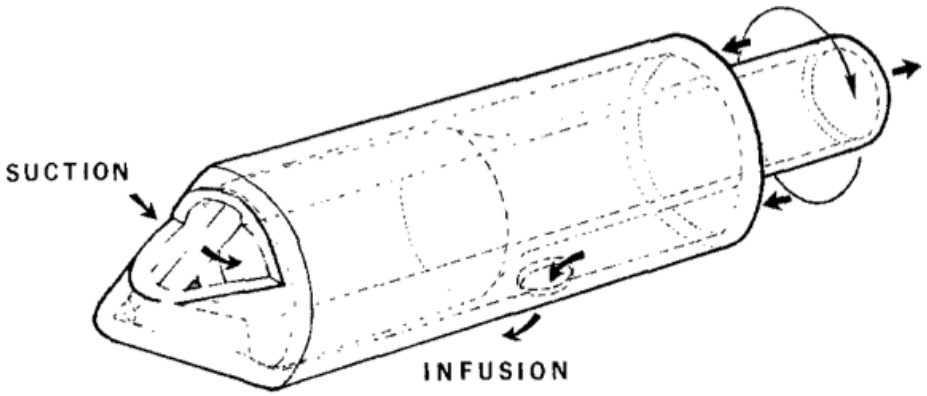

Figure 1.5: Illustration of the cutting portion of Machemer and Parel's improved design [32].

Recall that the original motivation for the design of a vitreous cutter was to combine the features of Kasner's sponge and scissors into a single instrument that could remove and cut vitreous while simultaneously backfilling the eye with a suitable support fluid (note the infusion port in Figure 1.5). However, as surgeons gained experience with PPV, they found that it was helpful to have a second instrument inside the posterior cavity to help stabilize and direct movement during surgery. Thus, surgeons turned toward a two-instrument technique with separate cutting and infusion tools, as depicted in Figure 1.6.

In 1974, O'Malley and Heintz presented their design for a vitreous cutter, which replaced what was then the state-of-the-art rotary-shearing action with an up-and-down reciprocating motion [39]. The new cutting design eliminated the lateral port on the

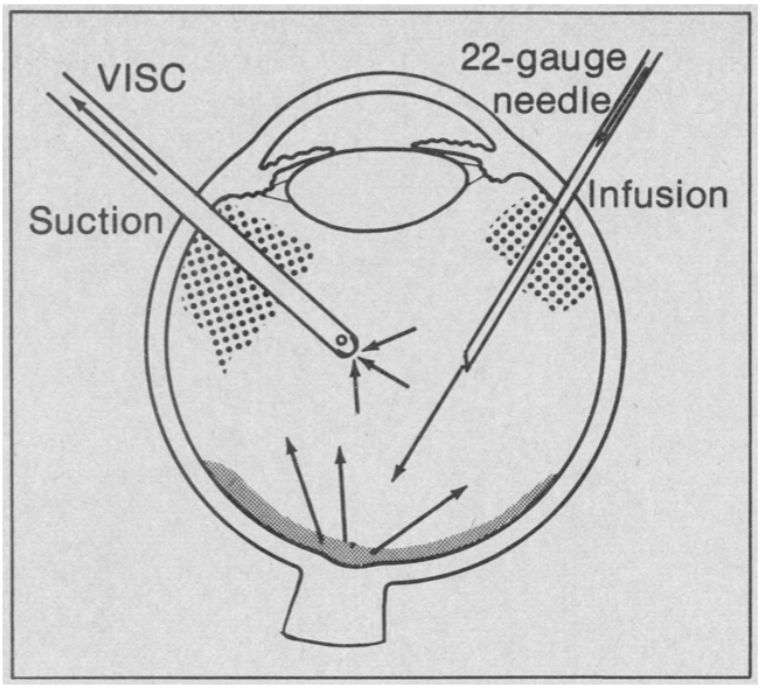

Figure 1.6: Illustration of the function and positioning of tools in a two-instrument PPV [31].

moving inner tube. Their lightweight design was driven pneumatically, with air pulses actuating the reciprocating inner shaft across the outer orifice, resulting in a guillotine-like cutting motion. A modern implementation of this cutting mechanism is depicted in Figure 1.7.

Rather than try to combine multiple functions into a single tool, they embraced the idea of a multi-instrument PPV. As a result, the vitreous cutter itself could be quite thin: 20 gauge (0.89 mm). The multi-instrument procedure involved making three incisions: one for the vitreous cutter, another for the infusion tube, and a third for an illumination probe. Their simple reciprocating design, and the concept of a three-port PPV, proved quite successful, becoming the gold standard for vitreous surgery [19, 45].

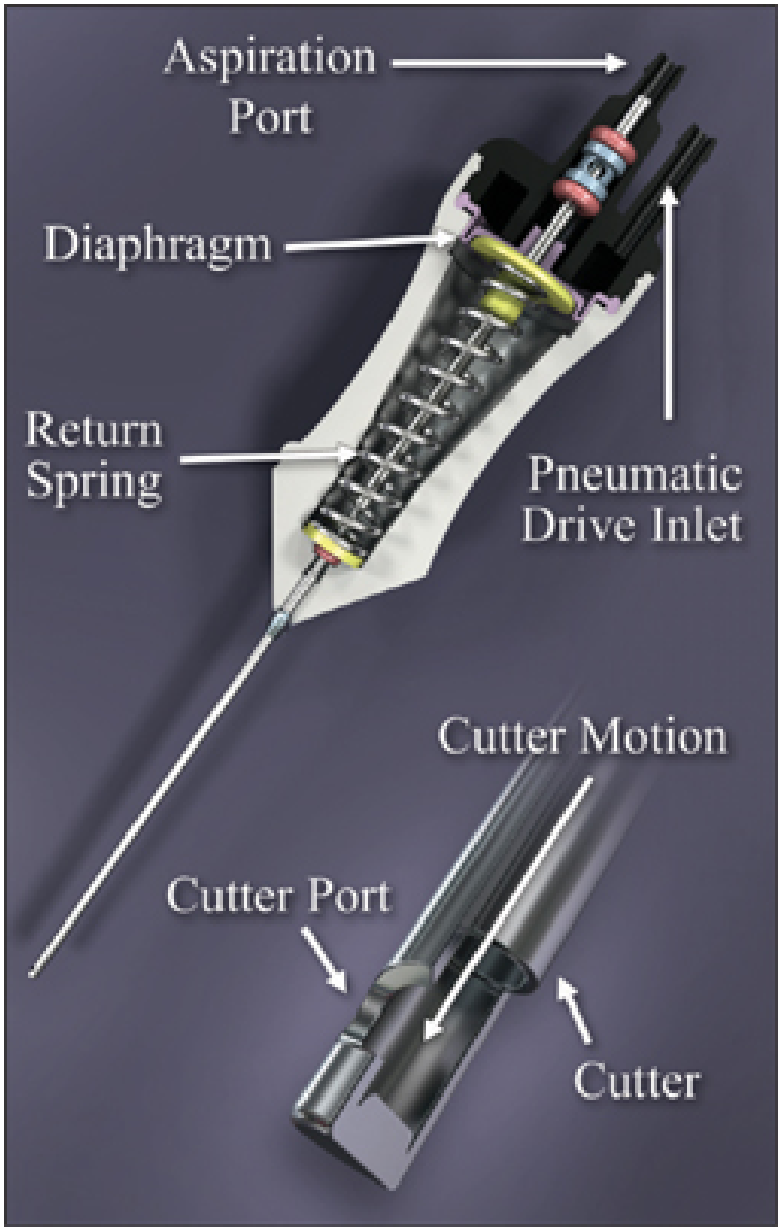

Figure 1.7: A cross section of a modern vitreous cutter, highlighting the pneumatically-driven, guillotine-like cutting action [25].

1.2.2 Modern Vitrectomy Developments

Modern instruments for vitrectomy are designed to be used in the three-port manner first described by O'Malley and Heintz [39]. This is counter to Machemer's original

vision of using a single tool to perform the four necessary tasks of cutting, aspirating, infusing, and illuminating, but has the benefit of allowing smaller instrument design, since each tool is responsible for only a small portion of the overall functionality. The attractiveness of smaller vitrectomy tools lies in their ability to reduce trauma at the incision sites, leading to improved patient outcomes and shorter healing times.

Keeping in mind the benefits associated with smaller surgical instruments, Fujii et al. introduced a 25-gauge (0.56 mm) transconjunctival sutureless vitrectomy system in 2002 [13]. In a typical vitrectomy using 20-gauge (0.89 mm) instruments, a conjunctival peritomy is performed, in which a long incision is made in the conjunctiva: the thin, outermost layer covering the sclera of the eye (see Figure 1.1). Incisions are then made in the pars plana region of the sclera to allow for the insertion of vitrectomy tools, as described in Section 1.2.1. Following the removal of the standard 20-gauge tools, sutures are require to close the access incisions in the sclera. A size comparison between a 20- and 25-gauge vitreous cutter is shown in Figure 1.8.

The narrowness of the 25-gauge design made it possible to skip the conjunctival peritomy and enter through relatively small incisions in the sclera. These incisions are small enough to allow for self-healing, or sutureless, procedures. This reduction in surgically induced trauma at the entry sites leads to faster postoperative recovery [13].

However, the reduction in size comes at the cost of a reduction in aspiration and infusion rates, as well as an objectionable increase in the flexibility of the instruments while

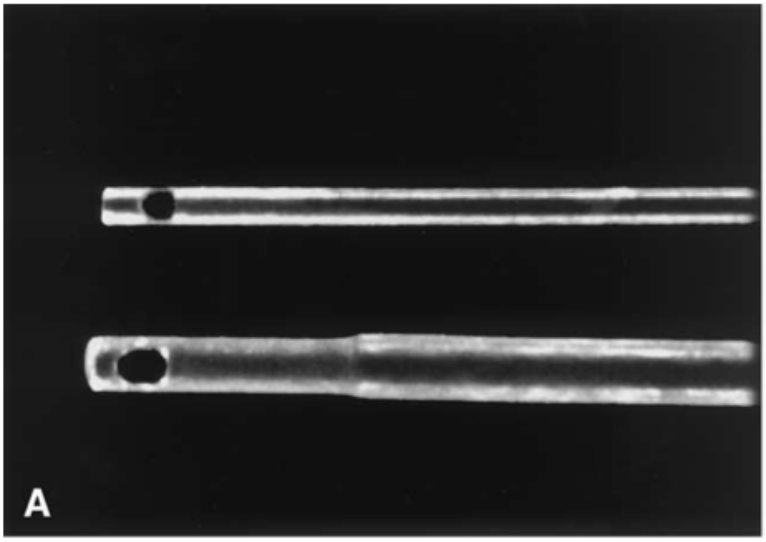

Figure 1.8: Comparison of the standard 20-gauge vitreous cutter (bottom) to the Fujii et al.'s 25-gauge design (top) [13].

performing complicated tasks which can impair a surgeon's ability to stabilize and direct movement during procedures [13, 11]. Fujii et al. recognized that a balance must be struck between high instrument functionality and minimally invasive design [13]. Eckardt was the first to introduce such a balanced approach, with his development of a 23-gauge (0.75 mm) vitrectomy system. The 23-gauge tools could be used in the same transconjunctival, sutureless manner as their 25-gauge counterparts, but came in a sturdier form factor and boasted improved flow rates [11]. For comparison, a 23-gauge vitreous cutter is shown alongside a 20- and 25-gauge cutter in Figure 1.9.

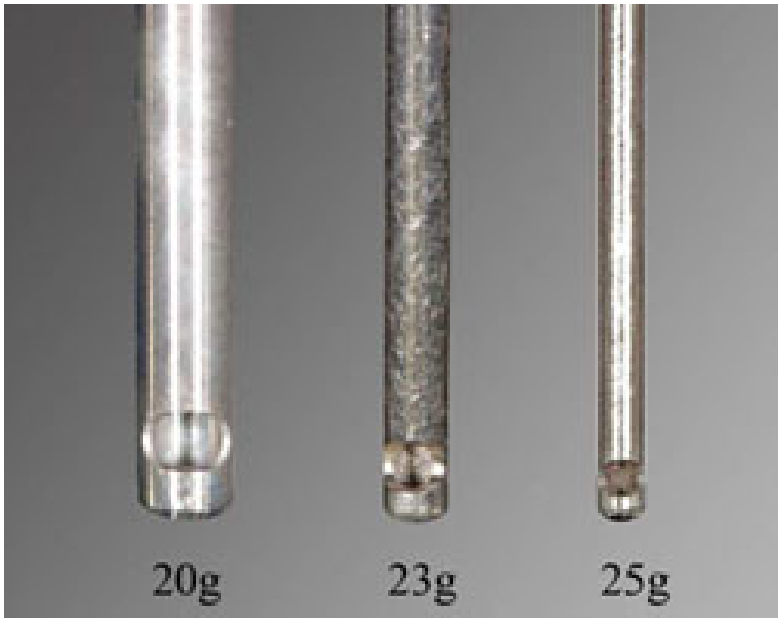

Figure 1.9: Eckardt's 23-gauge vitreous cutter, alongside the traditional 20-gauge and newer 25-gauge tools [52].

1.3 Previous Characterization Efforts

1.3.1 Experimental

As the number of vitreous cutter designs has steadily increased, it has become more challenging to choose the optimal instrumentation for vitrectomy [19]. Besides choosing the gauge, or width, of the tools to be used, surgeons must also make decisions about how to operate the device. Variables like cut rate, aspiration pressure, and duty cycle all affect overall performance. The cut rate is the frequency of guillotine cycles, and is typically expressed in units of cuts per minute (CPM). Aspiration pressure describes the vacuum pressure set at the surgeon's console which serves to draw in vitreous through the cutting port. The last variable, duty cycle, is defined as the ratio of the time the

cutter is open to the total cycle time.

The flow rate through the cutter is one of the most important metrics in classifying overall cutter performance. A higher flow rate is desirable, as it leads to faster operations; however, with larger flow rates comes the danger of inadvertently creating larger stresses, or tractions, throughout the posterior cavity of the eye, which can damage the delicate cells of the retina. Thus, an ideal vitreous cutter balances a high flow rate with a cutting mechanism that creates minimal disturbances in the surrounding vitreous.

A 2008 study by Hubschman et al. evaluated the flow rate and stiffness of 20-, 23-, and 25-gauge vitreous cutters under different operating conditions. Using egg white as an analog for vitreous, the study found that the 23-gauge cutter achieved a flow rate approaching that of the 20-gauge cutter when the aspiration pressure was increased from 250 mmHg to 550 mmHg [19]. More generally, they found that the flow rate for nearly every case increased when the cut rate was increased from 750 to 1500 CPM. Cutting rates higher than 1500 CPM have the potential to increase the fragmentation of vitreous, but because of the lower duty cycle, may lead to slightly lower flow rates [19]. Considering the parameter of stiffness, Hubschman et al. found that, as expected, the 20-gauge cutters were significantly stiffer than the 23-gauge cutters, which were, in turn, stiffer than the 25-gauge cutters. Interestingly, cutters of the same width from different manufacturers may have rigidity differences due to the type of metal used and the thickness of the outer shaft wall [19].

A follow-up study in 2009 focused on the response of flow rate during a particular cutting phase, i.e., as the cutter was (1) opening, (2) fully open, (3) closing, and (4) fully closed [18]. Using a high-speed camera, Hubschman et al. studied vitreous flow features during the opening and closing phases, finding the creation of a vortex during each cycle that may affect overall flow rate and create disturbances near the cutting tip. Frames from this high-speed film are shown in Figure 1.10.

The study also confirmed the importance of maximizing duty cycle, especially at high cut rates, to maintain high flow through the cutter. As before, same-gauge cutters from different manufacturers operating at the same cut rate and vacuum pressure proved to have different flow rates, likely due to differences in duty cycle and the geometry of the cutting port and internal shaft [18].

A 2008 study by Magalhaes et al. similarly found that in pneumatically-actuated cutters, the flow rate drops at higher cutting rates, due to a lower duty cycle [37]. This result is contrary to their observations with electrically-actuated cutters, in which higher cut rates at the same vacuum pressure resulted in higher flow rates. This contrast supports the hypothesis that a particular system's dynamics during the opening and closing events and the behavior of the vitreous at the cutting edge are important considerations when searching for the optimal vitrectomy system [37, 38].

1.3.2 Computational

A recent computational approach to this problem by Juan et al. looked at the effect of such parameter changes on mean flow rate [24]. Using a two-dimensional model operating in a Newtonian fluid, she found that the mean flow rate increases in a roughly linear fashion as a function of both aspiration pressure and duty cycle, ideas supported by the previously discussed experimental approaches. The computational approach allowed for the visualization of flow features associated with the opening and closing transitions of the guillotine. Specifically, she was able to investigate regions of disturbance near the cutter tip, offering these as a target for optimization since such disturbances have the potential to damage retinal cells. A set of characteristic computational results, highlighting the visualization of flow patterns around the cutting tip, is shown in Figure 1.11.

Further two-dimensional study attempted to account for the viscoelastic nature of the vitreous [23]. Again, the study determined that higher duty cycle improves mean flow rate, and that strong vorticity generated during guillotine motion is associated with higher flow rates. However, this must be balanced with the desire to minimize disturbances to the surrounding vitreous to reduce the potential for retinal cell damage. The study finds that slower guillotine motions during the opening and closing transitions are preferable to strike this balance. The difficulty of implementing a comprehensive viscoelastic model is evident in some of the simplified modeling choices, but the con-

clusions and trends highlighted in this study are a strong first step toward optimizing vitreous cutter design.

1.4 Objectives

Since Machemer's first concept of the vitreous cutter roughly four decades ago, there have been numerous fundamental design changes, with a general trend toward smaller instrumentation and less invasive procedures. With the introduction of 25- and 23-gauge vitreous cutters in 2002 and 2005, respectively, the selection of the optimal instrumentation is no longer straightforward. The surgeon's decision is further complicated by an even larger number of variables present during operation, including cut rate, the related concept of duty cycle, and vacuum pressure, to say nothing of the material and/or design differences between different vitrectomy system manufacturers. Although recent experimental studies have given some insight into how these myriad combinations affect the overall performance of a vitreous cutter, there remains a real need to comprehensively characterize the effect of design and operation changes in this complicated system. Similarly, recent efforts on the computational front have given insight into the importance of certain flow features and operation choices, but these were limited to two-dimensional physics and, in some cases, simplified modeling choices.

The goal of this study is to computationally model the complicated flow through a vitreous cutter during operation. The three-dimensional model described in this document

is built around a robust, viscoelastic solver. It offers a platform in which parameter changes such as geometry, cut rate, and vacuum pressure can be quickly implemented and accurately tested. These simulations will shed light on the optimal instrumentation for vitrectomy—balancing high flow rate with minimal disturbance to nearby fluid—and suggest operation guidelines for surgeons, leading to improved patient outcomes.

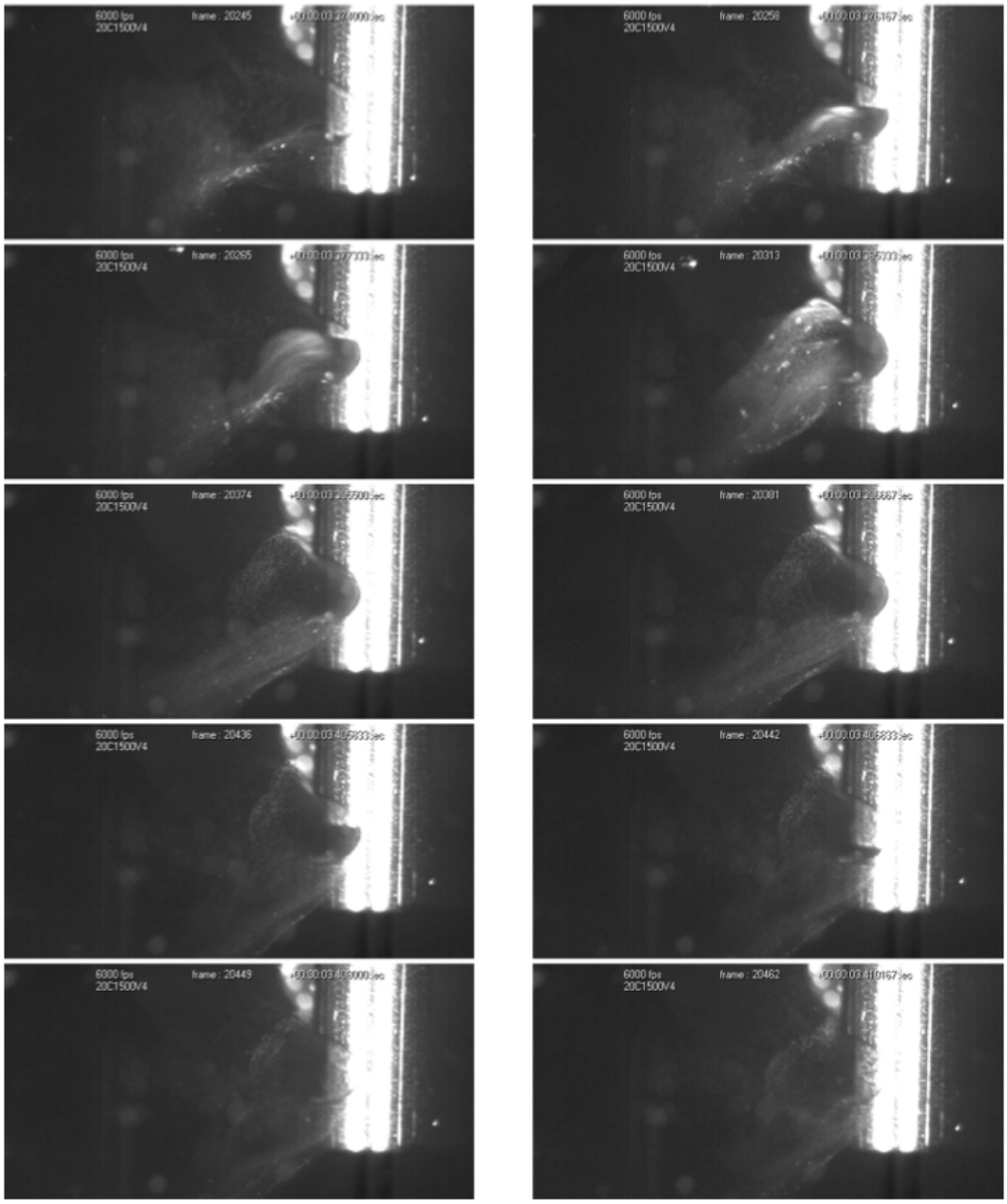

Figure 1.10: High-speed film frames of a modern vitreous cutter actively chopping and aspirating vitreous using a guillotine-like motion [17].

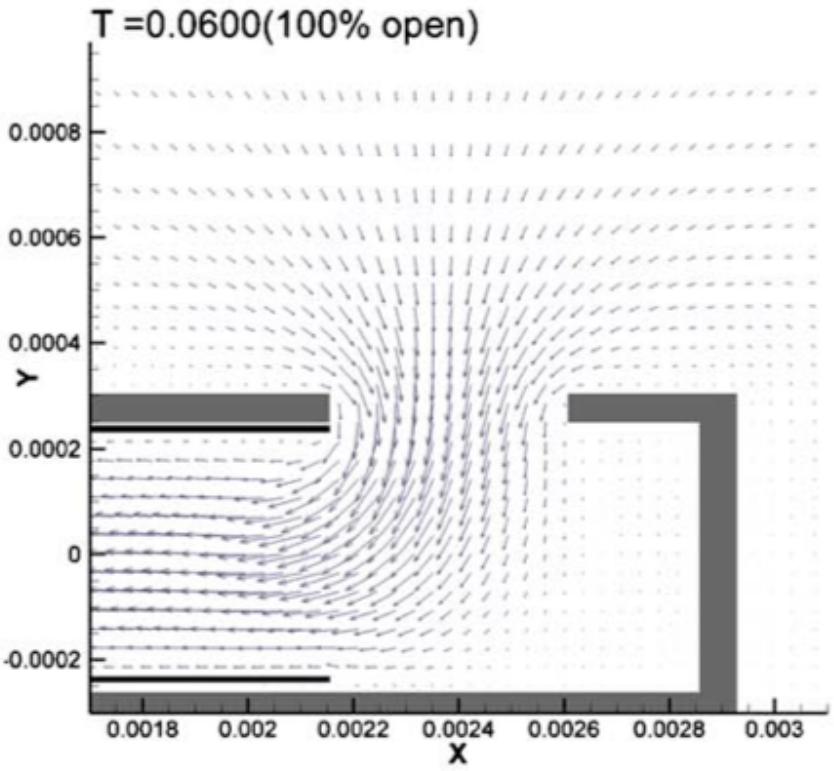

Figure 1.11: Flow field during the open phase of a two-dimensional vitreous cutter model operating at 1500 CPM and a vacuum pressure of 22.303 mmHg [24].

Chapter 2

Methodology

2.1 Computational Model

In order to perform a study of vitreous cutters, a three-dimensional model of the tool must first be constructed. As introduced in previous sections, a modern vitreous cutter is composed of a stationary outer shaft with a lateral orifice which surrounds a reciprocating, internal guillotine. A generic example of such a geometry is shown in cross section in Figure 2.1.

This relatively complicated three-dimensional geometry is represented in the algorithm by a signed distance field. A distance field represents the shortest distance between each node in the computational grid and the surface of the immersed solid being simulated. The sign of this distance value can be used to distinguish between solid and fluid nodes.

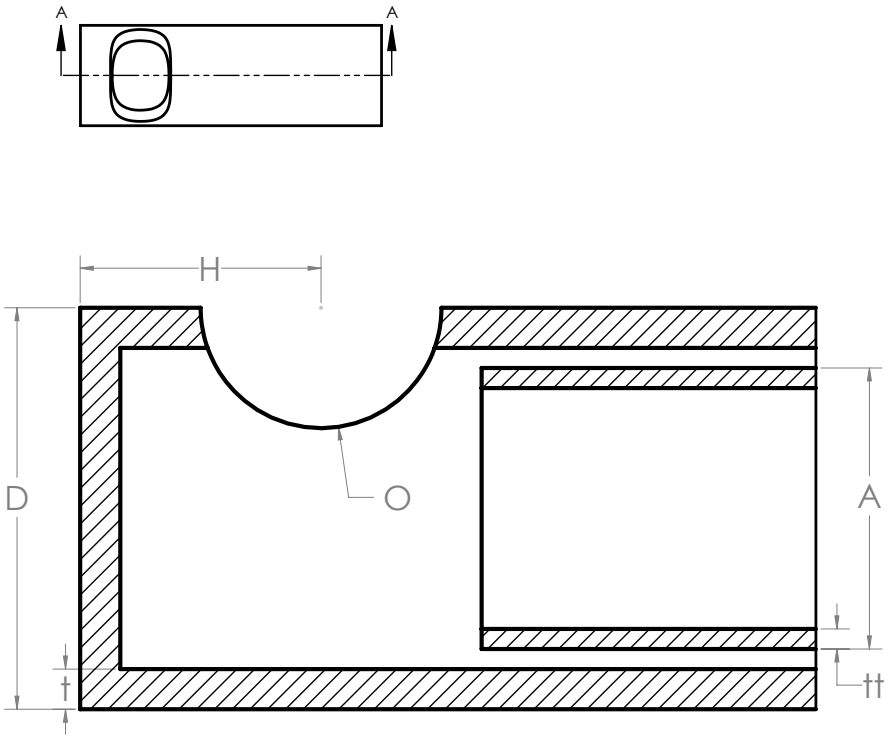

Figure 2.1: Cross section illustrating the internal geometry of a generic vitreous cutter design.

In this work, the convention that values are negatively signed inside the boundary and positively signed outside is used. Thus, the zero iso-contour of the signed distance field represents the surface of the immersed boundary, with values growing more positive or more negative moving outward into the fluid or inward into the solid, respectively [40].

These signed distance values play a pivotal role in an immersed boundary method; more will be said about this in Section 2.2.2. In addition to classifying nodes as solid, fluid, or interface, the magnitude of the signed distance field informs the algorithm as to which

fluid nodes are nearest the immersed boundary. It is through these so-called forcing points that the immersed boundary is "felt" by the fluid and propagated outward; thus, a precise and robust signed distance function is crucial to the accuracy and stability of any simulation. As an example, the signed distance field for a circular immersed boundary is shown in Figure 2.2.

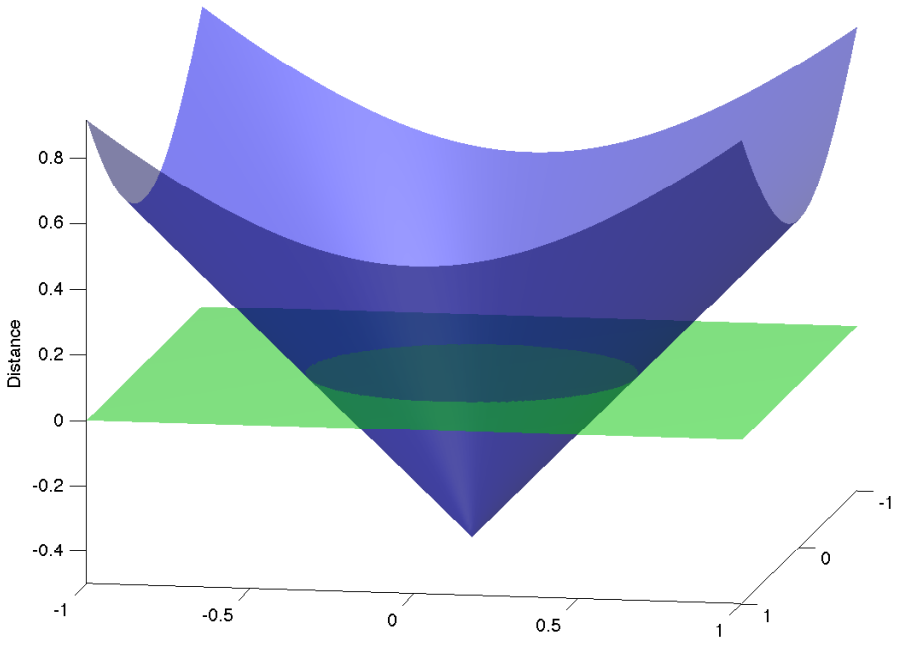

Figure 2.2: The signed distance field for a circular immersed solid, where nodes outside the boundary are positively signed and nodes inside are negatively signed.

The signed distance function depicted in Figure 2.2 is relatively simple; a circular immersed boundary centered at the origin can be represented by $Dist(x, y) = \sqrt{x^2 + y^2} - R$. This defines, for all points in the two-dimensional domain, a circle with radius R centered at $(0, 0)$. More complicated geometries can be modeled through the addition,

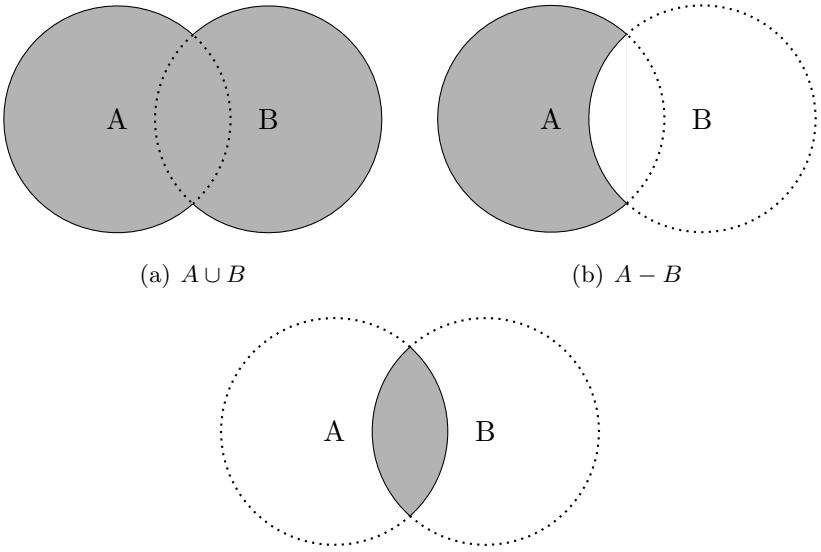

(a) $A \cup B$ (b) $A - B$

(c) $A \cap B$

Figure 2.3: The Boolean operations used to "sculpt" a complicated signed distance field from simple shapes.

subtraction, and/or intersection of simple shapes like this, as shown in Figure 2.3.

The operations depicted in Figure 2.3 can be implemented programmatically with relatively trivial maximum and minimum operations [12]. To unify two signed distance fields, as depicted in Figure 2.3(a), one simply needs to evaluate $min(\text{DistA}(...), \text{DistB}(...))$ for all points in the field. To perform a differencing operation, as in Figure 2.3(b), evaluate $max(\text{DistA}(...), -\text{DistB}(...))$ for all points in the field (noting the negative sign in front of distance field for shape B). An intersection operation, as in Figure 2.3(c), can be achieved by evaluating $max(\text{DistA}(...), \text{DistB}(...))$ for all points in the field. It is important to note that the choice of these Boolean functions is only correct when following the often-used convention that the signed distance values are negative in the the solid and positive in the fluid. For other conventions, the choice of maximum or minimum

(as well as the sign in front of the distance fields) may need to be reversed.

Using this technique, termed constructive solid geometry, it is possible to construct a complete, accurate, three-dimensional model of a vitreous cutter. Additionally, because the boundary is constructed using straightforward equations representing simple, cylindrical solids defined by the handful of dimensions shown in Figure 2.1, it is trivial to modify the dimensions of a cutter to quickly test design changes. Since the study is primarily concerned with the complex interaction between the vitreous, cutting port, and guillotine, the modeling area is limited to the distal tip (relative to the operator) of the cutter shaft. A representative sample geometry is shown in Figure 2.4.

With the geometry satisfactorily represented in this easily adjustable fashion, attention can turn to modeling the relationship between the solid body and the surrounding fluid.

2.2 Immersed Boundary Method

A problem with this degree of complicated, moving geometry lends itself well to an immersed boundary treatment, as first described by Peskin in 1972 for the simulation of flow through heart valves [42]. The common theme in any immersed boundary method is that the flow calculations are performed on a Cartesian grid that is *not* required to align or conform to the geometry of the solid object in the flow field.

To illustrate this distinction, consider the canonical case of flow past a two-dimensional

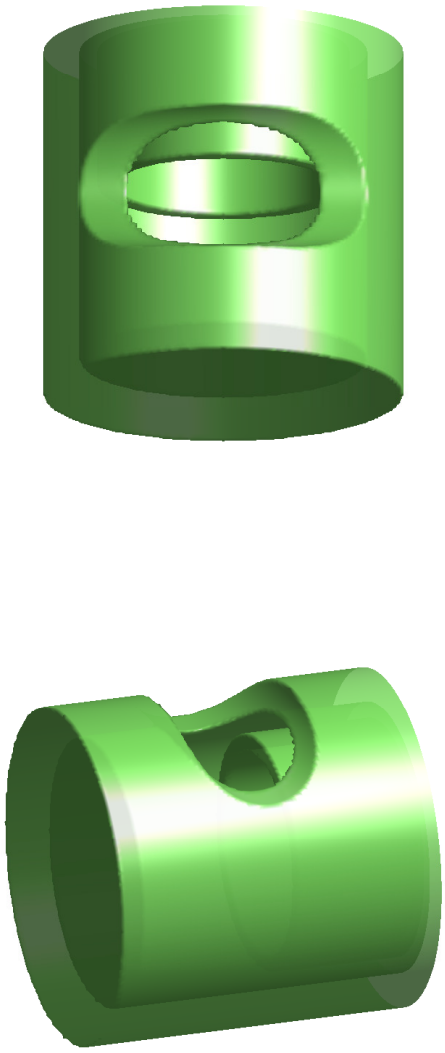

Figure 2.4: Two different views of the signed distance field for a three-dimensional vitreous cutter resolved on $\approx 1 \times 10^6$ evenly spaced grid points, where the green isosurface corresponds to $Dist(x, y, z) = 0$.

cylinder. The conventional approach would be to first generate a numerical mesh conforming to the surface of the cylinder, as shown in Figure 2.5(a).

With mesh points coinciding with the solid body, enforcing the conditions of no slip and no flow-through at the surface is straightforward. However, for all but the simplest geometries, the generation of this grid can necessitate significant user input. Structured body-fitted grids may require sophisticated sub-domain grid generation strategies, and although unstructured grids can be more resilient, they can have a negative effect on the stability and convergence properties of the algorithm. These problems are greatly compounded when the boundary is moving and/or deforming, since the expensive grid-generation step must be performed at each time step of the simulation as the boundary evolves [36, 35, 28].

In contrast, consider *immersing* the two-dimensional cylinder in a non-body-conformal Cartesian grid, as shown in Figure 2.5(b). Since mesh points are no longer required to coincide with the solid surface, enforcing no slip and no flow-through at the surface requires modifying the governing equations on nearby points. This modification—discussed in detail in Section 2.2.2—reproduces the effect of the boundary on the fluid, simulating the presence of a surface without altering the computational grid. This obviates the need for a complicated mesh-generation strategy, and eliminates re-meshing as the boundary evolves in time. The complicated geometry, coupled with the motion of the guillotine during operation, makes an immersed boundary method a natural choice for a successful study of a vitreous cutter. Before addressing exactly how the govern-

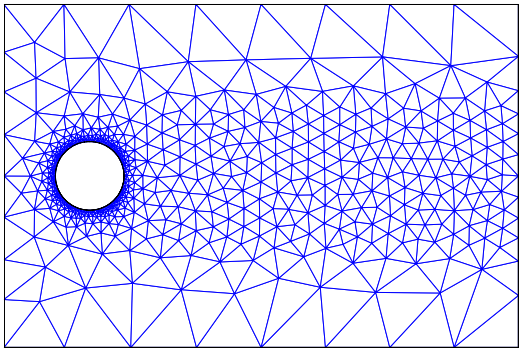

(a) Body-conforming mesh

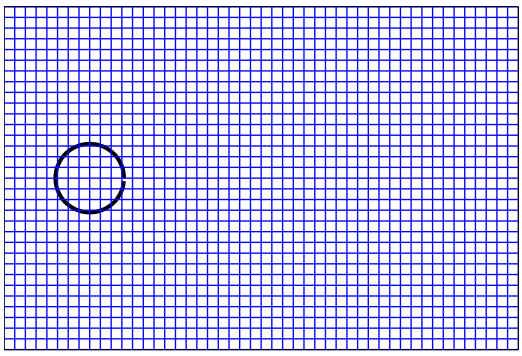

(b) Cartesian mesh

Figure 2.5: An stereotypical example of a body-conforming mesh used for simulating flow past a cylinder versus a cylinder "immersed" in a uniform Cartesian grid.

ing equations are modified near the immersed surface, it is appropriate to discuss the governing equations themselves.

2.2.1 Fractional Step Method

The simulation is governed by the Navier-Stokes and continuity equations, Equations 2.1 and 2.2, respectively. The role of the continuity equation is to enforce the incompressibility constraint.

$$\rho\left(\frac{\partial \mathbf{u}}{\partial t} + \mathbf{u}\cdot\nabla\mathbf{u}\right) = -\nabla \mathrm{P} + \mu\nabla^2\mathbf{u} \tag{2.1}$$

$$\nabla\cdot\mathbf{u} = 0 \tag{2.2}$$

Where ρ is the density of the fluid and μ is the dynamic viscosity of the fluid. The equations are solved in a non-dimensional form, with the following dimensionless variables.

$$\boldsymbol{x} = \frac{\mathbf{x}}{L_{\mathrm{ref}}}, \quad \boldsymbol{u} = \frac{\mathbf{u}}{U_{\mathrm{ref}}}, \quad t = \frac{\mathrm{t}}{L_{\mathrm{ref}}/U_{\mathrm{ref}}}, \quad P = \frac{\mathrm{P}}{\rho U_{\mathrm{ref}}^2} \tag{2.3}$$

Where U_{ref} and L_{ref} are the reference velocity and reference length, respectively. These

values typically have a logical choice dictated by the problem being solved. For example, the reference velocity in a vitreous cutter might be the closing speed of the guillotine, and the reference length might be the outer diameter of the outer shaft. Once chosen, these values define a Reynolds number which governs the problem, $\mathrm{Re} = \frac{\rho U_{\mathrm{ref}} L_{\mathrm{ref}}}{\mu}$. Rewriting Equations 2.1 and 2.2 in terms of the dimensionless quantities leads to the following:

$$\frac{\partial \boldsymbol{u}}{\partial t} + \boldsymbol{u} \cdot \nabla \boldsymbol{u} = -\nabla P + \frac{1}{\mathrm{Re}} \nabla^2 \boldsymbol{u} \tag{2.4}$$

$$\nabla \cdot \boldsymbol{u} = 0 \tag{2.5}$$

Equations 2.4 and 2.5 are discretized in a method similar to Yang and Balaras, using second-order, central finite differences on a staggered grid [55]. Since the locations of these values influences the required finite difference stencil, the storage locations of values on a staggered grid are shown in Figure 2.6.

Still following the cue of Yang and Balaras, the equations are integrated in time using a third-order Runge-Kutta method [55]. To enforce the continuity constraint, a fractional-step approach is used. The fractional step method solves two sub-steps for each time interval: (1) a predictor and (2) a corrector. In the first, the predicted velocity at the

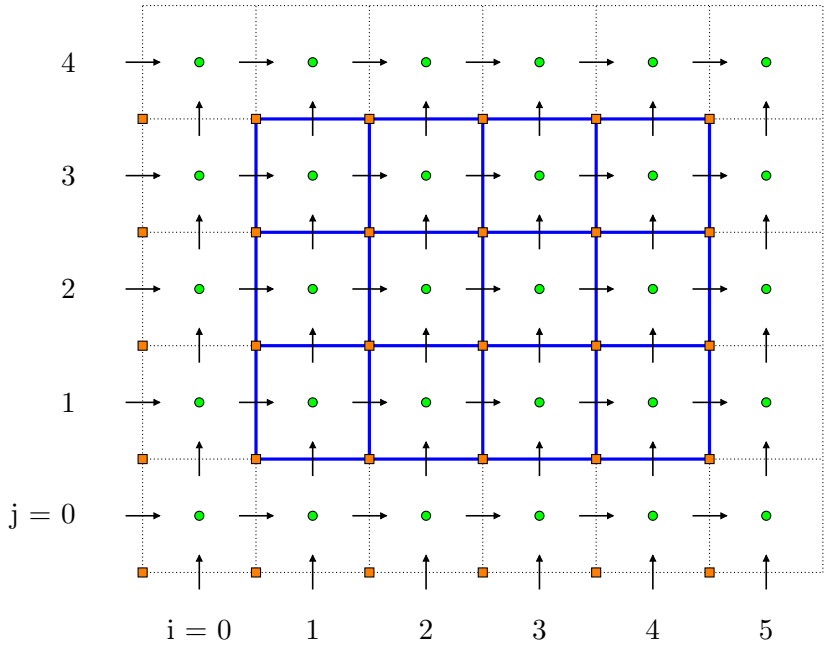

Figure 2.6: Storage locations for information on a two-dimensional staggered grid, NX = 4 and NY = 3, ∘ = Pressure, →= u-velocity, ↑= v-velocity, and □ = vorticity.

next time step, termed $\boldsymbol{u}^*$, is explicitly calculated from the Navier-Stokes terms.

$$\frac{\boldsymbol{u}^* - \boldsymbol{u}^n}{\Delta t} = \frac{1}{\mathrm{Re}}\nabla^2\boldsymbol{u}^n - \boldsymbol{u}^n \cdot \nabla\boldsymbol{u}^n - \nabla P^n \tag{2.6}$$

Where the superscript n denotes the value of the fluid variable at the current time step, and the superscript $*$ denotes the predicted value at the next time step. The predicted velocity field calculated with Equation 2.6 is, in general, *not* divergence free, so the second sub-step, a "pressure correction", is performed.

$$\frac{\boldsymbol{u}^{n+1} - \boldsymbol{u}^*}{\Delta t} = -\nabla\phi \tag{2.7}$$

$$\frac{\nabla \cdot \boldsymbol{u}^{n+1} - \nabla \cdot \boldsymbol{u}^*}{\Delta t} = -\nabla^2\phi$$

$$\therefore \nabla \cdot \boldsymbol{u}^* = \Delta t \nabla^2 \phi \tag{2.8}$$

Where the superscript $n+1$ denotes the value of the fluid variable at the next time step. In Equation 2.7, a new variable, ϕ, is introduced to represent the change in the pressure field required to correct the prediction, $\boldsymbol{u}^*$, to $\boldsymbol{u}^{n+1}$. Evaluating the divergence of each term, and remembering that $\nabla \cdot \boldsymbol{u}^{n+1} = 0$ to satisfy the continuity constraint, results in a Poisson Equation, 2.8, that can be solved for the change in the pressure field, ϕ. The true velocity field, $\mathbf{u}^{n+1}$ can now be calculated by substituting ϕ and $\mathbf{u}^*$ into Equation 2.7.

$$\boldsymbol{u}^{n+1} = \boldsymbol{u}^* - \Delta t \nabla \phi \tag{2.9}$$

Finally, the pressure field is updated to reflect the adjustment required to make the flow divergence free.

$$P^{n+1} = P^n + \phi \tag{2.10}$$

After all the flow variables have been updated, the algorithm increments time, solves for a new $\boldsymbol{u}^*$, calculates a new ϕ, corrects $\boldsymbol{u}^*$ to $\boldsymbol{u}^{n+1}$, updates values, and so on. As previously stated, these equations are enforced on a Cartesian grid which is not required to align or conform to the solid body. The method for modifying these governing equations near the immersed surface is introduced in the next section.

2.2.2 Immersed Boundary Treatment

As noted in Section 2.2, the distinguishing characteristic of any immersed boundary method lies in how it modifies the governing equations near the immersed surface to satisfy no slip and no flow-through at the surface of the solid body without altering the non-body-conforming Cartesian grid. Generally speaking, there are two fundamentally different approaches to this problem [36]. In the first, the forcing term is introduced into the governing equations themselves before discretization, and in the second, the governing equations are discretized without regard to the immersed boundary, only to be adjusted to account for its presence afterward. The so-called "continuous forcing" and "discrete forcing" approaches, respectively, both have their benefits; however, for the simulation of a vitreous cutter, the discrete forcing approach is preferable, as it represents the immersed geometry with a relatively higher degree of spatial precision,

resulting an a "sharp" interface of solid and fluid [36, 35].

The exact implementation of the discrete forcing used in these studies closely follows the approach of Balaras [4, 55]. The first step in such an approach is to identify all the fluid points in the computational domain. As noted in Section 2.1, the use of a signed distance function makes this a trivial step—simply identify all the points with a *positive* signed distance value. Given the list of fluid points, the next step is to identify the forcing points, which are defined as any fluid points with an orthogonal neighbor (either north-south, east-west, or front-back) in the solid. The identification procedure used to find these points in two dimensions is illustrated in Figure 2.7.

After generating the list of forcing points, a triangular interpolation region is constructed around each one, as shown in Figure 2.7. The vertices of the triangle are chosen in a specific way: two are points in the fluid that are not also forcing points, and the third is the point on the surface of the immersed boundary nearest the forcing point. Finding the third point in the interpolation stencil requires constructing a line passing through the forcing point that is normal to the immersed boundary. The resulting interpolation region is shown in more detail in Figure 2.8.

With the interpolation region defined, the value at the forcing point can now be calculated. Since the values at the two fluid points are known, and the value at the surface point is prescribed—no slip and no flow-through, where velocity can be zero for a stationary wall, or non-zero for a moving surface—the value at the forcing point can be

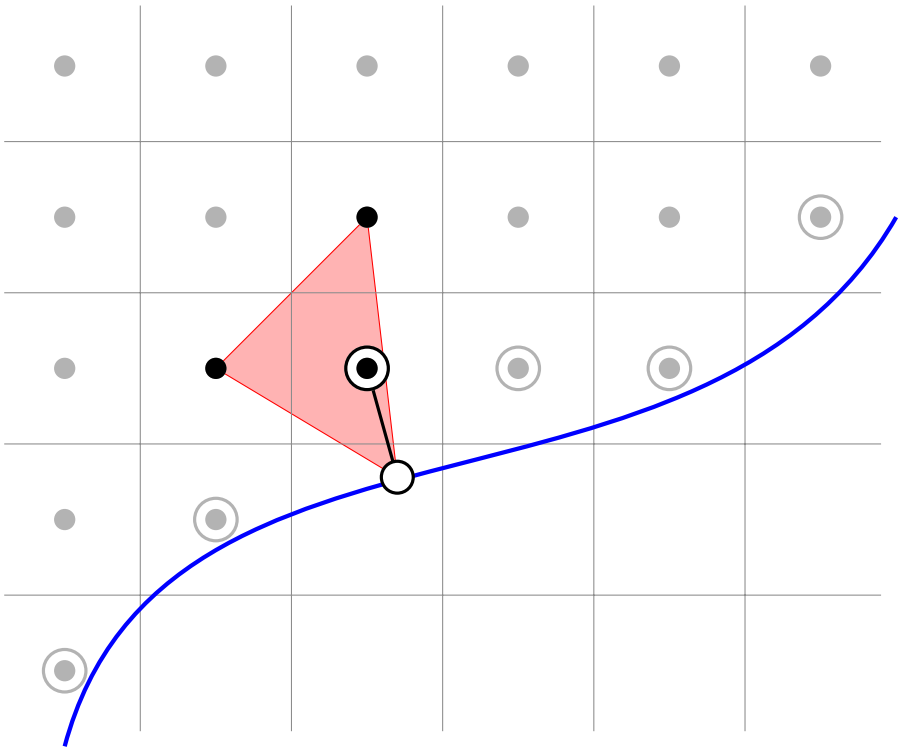

Figure 2.7: Illustration of the procedure used to define the interpolation region for a forcing point, where the blue line is the immersed surface, the closed circles are fluid points, the open circles denote forcing points, and an example triangular interpolation region is shaded red.

obtained by means of a bilinear interpolation. Thus, the effect of the immersed boundary is "felt" by the fluid forcing points and propagated outward, reproducing the effect of the boundary without altering the computational grid. In cases where the triangular interpolation region depicted in Figure 2.7cannot be constructed, usually due to a limited number of non-forcing fluid points due to irregular geometry near "internal" solid corners, the solver reverts to a simpler linear interpolation.

Incorporating a moving boundary only requires that the signed distance function be updated at each time step; no re-meshing is necessary. The interpolation routine remains

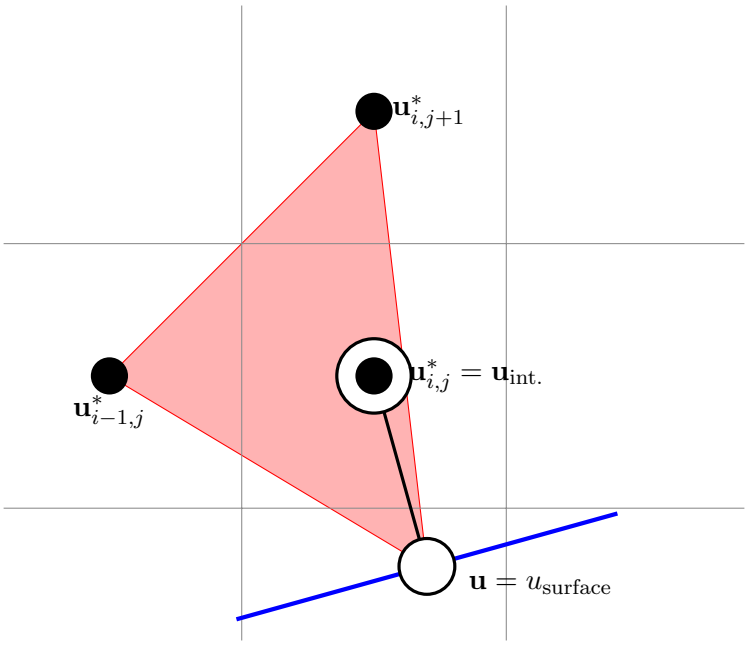

Figure 2.8: Illustration of the interpolation procedure used to determine the fluid variable value, $\boldsymbol{u}_{\text{int.}}$, at the forcing point.

unaltered; however, special treatment must be applied to freshly cleared nodes from inside the solid body. Consider the translation of a circular immersed boundary as shown in Figure 2.9.

The dotted red line in Figure 2.9 represents a potential finite differencing stencil, which includes a newly exposed node from inside the solid body. As a freshly cleared node, it has non-physical flow values. In order to avoid propagating the junk data from inside the solid, these sold-to-fluid nodes are assigned new values using the same bilinear interpolation previously described. With this interpolation, the nodes can be used for a meaningful calculation of the intermediate velocity, $\boldsymbol{u}^*$, at the next time step.

Before addressing the boundary conditions in the next section, it is helpful to see the

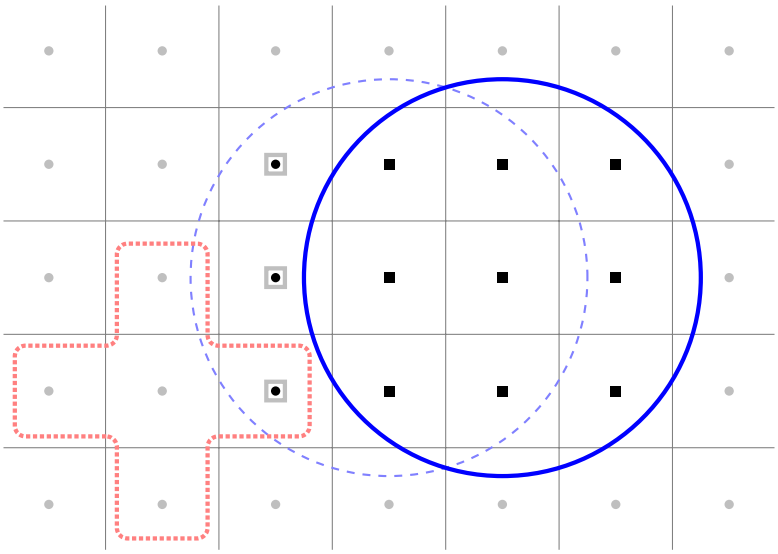

Figure 2.9: Illustration showing the previous (dotted) and current (solid) position of a circular immersed boundary moving from left to right, where the solid circles are fluid nodes, the solid squares are solid nodes, and the open squares show freshly cleared solid nodes.

overall method for applying all these ideas. For each time step, the numerical algorithm proceeds as follows:

1. Compute the convective, viscous, and pressure terms
2. Calculate the predicted velocity at the next time step, $\boldsymbol{u}^*$ (Equation 2.6)
3. Apply forcing to fluid points nearest the immersed boundary (Figures 2.7 and 2.8)
4. Construct and solve the Poisson equation (Equation 2.8)
5. Calculate the true velocity at the next time step, $\boldsymbol{u}^{n+1}$ (Equation 2.9)
6. Update $\boldsymbol{u}$ and P
7. Update signed distance function and adjust freshly-cleared nodes (if necessary)

8. Increment time

2.2.3 Boundary Conditions

During a vitrectomy, the chopped vitreous is drawn out of the eye by means of a vacuum applied at the surgeon's end. Since the intraocular pressure is higher than this vacuum, a pressure gradient is established which causes vitreous to be entrained into the cutter and drawn through the internal shaft. To replicate these boundary conditions, the algorithm relies on the surface traction vector discussed by Gresho [16, 15].

$$\boldsymbol{F} = \boldsymbol{n} \cdot \boldsymbol{\sigma} \tag{2.11}$$

Where $\boldsymbol{F}$ is the surface traction, $\boldsymbol{n}$ is the outward-pointing unit vector on the boundary, and $\boldsymbol{\sigma}$ is the stress tensor. This type of open boundary conditions allows the pressure to be specified without knowing *a priori* the velocity at the boundaries. Additionally, it allows the computational domain to be truncated without sacrificing a natural fluid entrainment [15]. For the case of a planar boundary, as will be the case on the outer walls of the computational domain, Equation 2.11 can be decomposed into the following normal and tangential (shear) components.

$$F_n = -P + 2\mu \left(\frac{\partial \boldsymbol{u}_n}{\partial n} \right) \tag{2.12}$$

$$F_t = \left(\frac{\partial \boldsymbol{u}_t}{\partial n} \right) \tag{2.13}$$

Where $\boldsymbol{u}_n$ denotes the component of velocity normal to the boundary and $\boldsymbol{u}_t$ denotes the component of velocity tangential to the boundary. From the physics of the vitreous cutter problem, it is logical to specify these surface traction vectors in terms of a pressure. The specified pressure acts normal to the boundary, replacing F_n in Equation 2.14, and is taken at time level $n+1$ [6]. Since the physics of the problem do not suggest a choice for the traction in the tangential direction, it is set to 0, a convenient, "free slip" condition [7]. With these considerations in mind, the traction boundary conditions can be written in the following form.

$$-P_\infty = -P + 2\mu \left(\frac{\partial \boldsymbol{u}_n}{\partial n} \right) \tag{2.14}$$

$$0 = \left(\frac{\partial \boldsymbol{u}_t}{\partial n} \right) \tag{2.15}$$

Where $-P_\infty$ is the desired ambient pressure on the boundary. These traction boundaries make it possible to assign pressure conditions to each wall of the computational domain, as shown in Figure 2.10.

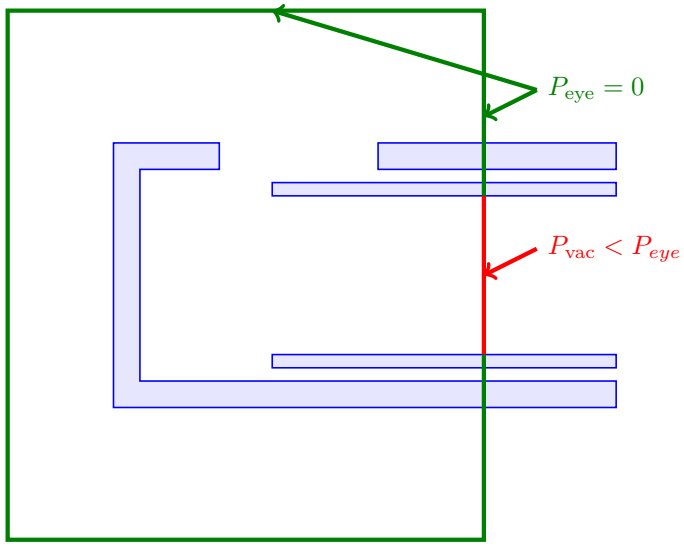

Figure 2.10: A cartoon schematic showing how the walls of the computational domain are assigned a pressure to establish a pressure gradient.

The intraocular pressure is set to be zero, and the vacuum pressure is chosen to represent the magnitude of the vacuum in the draining tube relative to the eye. These choice of these boundary conditions, driven by the underlying physics of the vitreous cutter, allow a pressure gradient to be established as it would be during a vitrectomy. At this point, enough of a method has been developed to perform Newtonian simulations of a vitreous cutter during operation. However, the critical component of the current work lies in pairing everything previously discussed with an appropriate non-Newtonian fluid. The properties of vitreous, and the choice of a constitutive equation capable of representing those properties, are discussed in the following sections.

2.3 Modeling Vitreous

2.3.1 Experimental Rheology

In order to choose an appropriate computational approach for modeling vitreous, it is first necessary to understand its basic properties. Great progress has been made by Sharif-Kashani et al. to experimentally characterize the properties of this complicated substance, without which, the current work would have limited real-world significance.

As introduced in Section 1.1.2, vitreous is a viscoelastic fluid, exhibiting both a solid and liquid-like nature. One of the most important measures that can be derived from experimentation is a quantification of the influence of these natures; in other words, a measure of how elastic versus how liquid the vitreous is. To obtain this information, Sharif-Kashani et al. surgically removed intact vitreous from freshly-harvested porcine eyes. Since the vitreous was still intact, long collagen molecules were still providing structural integrity. A stress-controlled rheometer was used to perform a creep-compliance test on the intact vitreous. Creep is a phenomenon in viscoelastic materials in which a material experiences an increase in strain over time without a corresponding increase in stress. In this test, a constant shear stress is applied until the sample reaches a linear steady-state condition [48]. The results are shown in Figure 2.11.

The resulting plot can be roughly divided into three sections. For short time scales

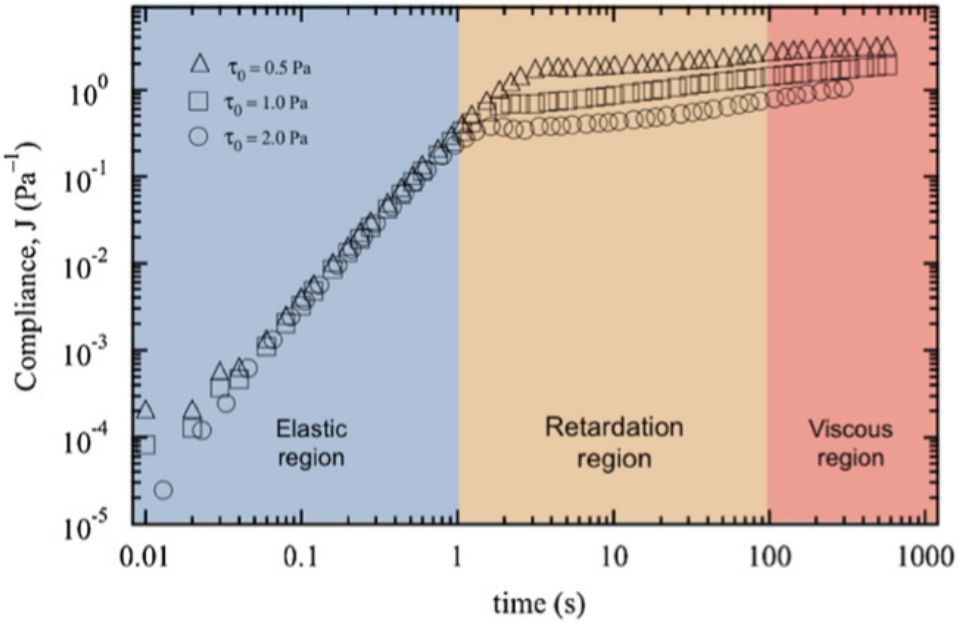

Figure 2.11: Compliance of intact vitreous as a function of time for different shear stresses.

(up to approximately 1 second) the intact vitreous behaves as a linearly-elastic solid, exhibiting negligible liquid-like behavior. This region is followed by a transition region (from approximately 1 to 100 seconds) in which the vitreous behaves like a viscoelastic gel: neither purely elastic nor purely liquid. Finally, after approximately 100 seconds of testing, the vitreous enters the viscous region and begins exhibiting liquid-like behavior [47, 48]. Conceptually, this means that at short time scales, can be expected to behave like a purely-elastic solid, because the long collagen molecules are not given time to slide past each other. Only at very long time scales can it be expected to flow, or exhibit purely-liquid behavior.

These results make sense in the context of the development of vitreous cutters introduced

in Section 1.2.1. After all, it is precisely because of this highly elastic behavior that a cutting mechanism is necessary during vitrectomy. Breaking up the long collagen fibers, as described in Section 1.1.2, allows the vitreous to behave more like a fluid, and be smoothly aspirated from the eye. Furthermore, because the level of fragmentation of the collagen fibers is dependent on surgical variables such as cut rate, it is not surprising that slightly different time scales can be obtained for vitreous processed under different operating conditions. To obtain a precise description of how this chopped substance differs from the un-chopped, as well as the differences between different chopping speeds, the work of Sharif-Kashani et al. is, again, an invaluable resource. The results for chopped vitreous processed under different conditions are shown alongside the results for intact vitreous in Table 2.1.

Table 2.1: Comparison of time scales between intact and chopped vitreous [47].

	Mean τ_{retard} (s)	Mean τ_{relax} (s)
Intact Vitreous	1	100
Chopped Vitreous (500 CPM)	0.13	4.01
Chopped Vitreous (2000 CPM)	0.14	3.60
Chopped Vitreous (2500 CPM)	0.22	5.69

Clearly, both the retardation and relaxation mechanism for chopped vitreous is reduced from that of intact vitreous, as evidenced by the much shorter time scales. Though the chopped vitreous has a much more fluid-like nature, it still exhibits elasticity on small time scales. Additionally, Sharif-Kashani et al. found that chopped vitreous exhibits

a phenomenon known as shear thinning, in which the viscosity decreases monotonically with increasing shear rate [47]. When deciding on a computational approach, it is important to give due consideration to these defining features. Namely, any appropriate constitutive model must be capable of dealing with elastic behavior, dictated by retardation and/or relaxation time scales, and reproducing shear-thinning effects. Furthermore, the implementation should be robust enough to handle the very elastic nature (very large time scales) of the intact gel. With this in mind, it is possible to arrive at one of the constitutive models introduced in the following section.

2.3.2 Viscoelastic Constitutive Models

Capturing the viscoelastic nature of vitreous is one of the most critical and challenging obstacles in this study. Perhaps the most basic and important characteristic of viscoelastic fluids is their shear-rate dependent or non-Newtonian viscosity [5]. Before documenting how this viscosity relies on information from the velocity field, it is necessary to have an understanding of the total stress tensor and how it applies to Navier-Stokes. The total stress tensor, $\boldsymbol{\sigma}$, can be split up into two parts, as shown below.

$$\boldsymbol{\sigma} = -P\boldsymbol{I} + \boldsymbol{T} \tag{2.16}$$

In equation 2.16, P is the pressure and $\boldsymbol{I}$ is the 3×3 identity tensor. The term $-P\boldsymbol{I}$

represents the stress due to compression of the fluid. The remaining term, $\boldsymbol{T}$, is the portion of the total stress tensor that arises from the viscosity of the fluid. Rewriting Equation 2.1 in terms of the total stress tensor yields the Cauchy momentum equation, 2.17.

$$\rho\left(\frac{\partial \mathbf{u}}{\partial t} + \mathbf{u}\cdot\nabla\mathbf{u}\right) = \nabla\cdot\boldsymbol{\sigma} \tag{2.17}$$

Since the viscosity of a non-Newtonian fluid depends on the velocity field, the task of any viscoelastic constitutive model is to relate $\boldsymbol{T}$ to the velocity field [5].

Maxwell Model

Maxwell was the first to attempt to obtain such a constitutive equation [5]. The Maxwell model can be represented as a spring and dashpot connected in series, shown in Figure 2.12.

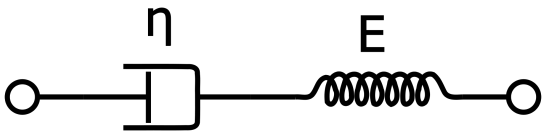

Figure 2.12: A single Maxwell element, a purely viscous dashpot connected, in series, to a purely Hookean solid.

The spring behaves as a purely Hookean solid with elastic modulus E and the dashpot behaves as a purely Newtonian fluid with viscosity μ. Such a model seems to be a promising starting point for describing a material with both solid and fluid properties.

Since the two elements are linked in series, the force acting on both must be equal. The rate of displacement of the system, $\partial\boldsymbol{\gamma}/\partial t$, can then be written as shown in Equation 2.18.

$$\frac{\boldsymbol{T}}{\mu} + \frac{1}{E}\frac{\partial \boldsymbol{T}}{\partial t} = \frac{\partial \boldsymbol{\gamma}}{\partial t} \tag{2.18}$$

Purely Newtonian or Hookean responses can be recovered from Equation 2.18. For a constant stress, the time derivative on the left-hand side vanishes, leaving a Newtonian fluid with viscosity μ. Similarly, for a sudden change in stress, the time derivative on the left-hand side dominates the overall response, and the system behaves as a Hookean solid with modulus E. Introducing more systemic variables to the Maxwell model leads to the more familiar form of the equation shown below.

$$\boldsymbol{T} + \lambda_1 \frac{\partial \boldsymbol{T}}{\partial t} = \eta_0 \dot{\boldsymbol{\gamma}} \tag{2.19}$$

Equation 2.19 introduces a constant, λ_1, known as the relaxation time. This is the same time constant, τ_{relax} measured by Sharif-Kashani et al. in Section 2.3.1. This time constant is equivalent to μ/E, and can be conceptualized as the time it takes the fluid to "relax" back into equilibrium after the application of an instantaneous stress. Additionally, μ has been replaced with η_0, the viscosity associated with zero shear rate. The rate-of-strain tensor, $\dot{\boldsymbol{\gamma}}$, appears as the symmetric component in the velocity

gradient tensor, $\nabla u = \frac{1}{2}(\dot{\gamma} + \boldsymbol{\omega})$, where $\boldsymbol{\omega}$ is the antisymmetric rate-of-spin, or vorticity, tensor. Often, the rate-of-strain tensor is expressed in terms of its contribution to the velocity gradient, where $\frac{1}{2}\dot{\gamma} = \boldsymbol{D} = \frac{1}{2}\left(\nabla \boldsymbol{u} + (\nabla \boldsymbol{u})^T\right)$, allowing the right-hand side of Equation 2.19 to expressed in terms of $\boldsymbol{D}$ as $2\eta_0 \boldsymbol{D}$ [5].

Upper-Convected Maxwell Model

This relatively simple model is not sufficient to describe cases of large displacement, as Hooke's law is valid only for small strains. To account for large displacements, the Eulerian time derivative needs to be replaced with a time derivative that accounts for stretching and rotation of the reference frame. Such a derivative is called the upper-convected time derivative. The general form of the upper-convected derivative for a tensor is shown below.

$$\boldsymbol{T}_{(1)} = \frac{D}{Dt}\boldsymbol{T} - (\nabla \boldsymbol{u})^T \cdot \boldsymbol{T} - \boldsymbol{T} \cdot (\nabla \boldsymbol{u}) \tag{2.20}$$

In Equation 2.20, $\nabla \boldsymbol{u}$ is the tensor of derivatives of the velocity field and $\boldsymbol{T}$ is the portion of the total stress tensor due to viscosity, as seen before. The D/Dt notation specifies a material derivative, which takes into account deformation of the reference frame. The form of the material derivative is given below.

$$\frac{D}{Dt}\boldsymbol{T} = \frac{\partial}{\partial t}\boldsymbol{T} + \boldsymbol{u} \cdot \nabla \boldsymbol{T} \tag{2.21}$$

Replacing the Eulerian time derivative in Equation 2.19 with the upper-convected derivative defined in Equation 2.20, yields the upper-convected Maxwell model shown below.

$$\boldsymbol{T} + \lambda_1 \boldsymbol{T}_{(1)} = \eta_0 \dot{\boldsymbol{\gamma}} \tag{2.22}$$

Where the full form of the upper-convected derivative of the stress tensor, $\boldsymbol{T}$, is given by

$$\boldsymbol{T}_{(1)} = \frac{\partial}{\partial t}\boldsymbol{T} + \boldsymbol{u} \cdot \nabla \boldsymbol{T} - (\nabla \boldsymbol{u})^T \cdot \boldsymbol{T} - \boldsymbol{T} \cdot (\nabla \boldsymbol{u}) \tag{2.23}$$

This extension of the Maxwell model is one of the most fundamental constitutive equations in non-Newtonian flows, and has been widely studied because of it's simplicity. The upper-convected Maxwell model has been the platform for many subsequent attempts to characterize viscoelastic flows, and many more complicated models can recover upper-convected Maxwell with certain parameter choices [5].

Oldroyd-B Model

One significant extension of the upper-convected Maxwell model is the Oldroyd-B model, or convected Jeffreys model, which begins with the introduction of an additional linear relationship into Equation 2.19. Conceptually, this additional term represents a

Newtonian solvent in which the viscoelastic fluid, represented as Maxwell elements, is immersed. This yields the Jeffreys model, shown below.

$$\boldsymbol{T} + \lambda_1 \frac{\partial \boldsymbol{T}}{\partial t} = \eta_0 \left(\dot{\boldsymbol{\gamma}} + \lambda_2 \frac{\partial \dot{\boldsymbol{\gamma}}}{\partial t} \right) \tag{2.24}$$

Equation 2.24 introduces a new time constant, λ_2, known as the retardation time. Again, this is the same time constant, τ_{retard}, measured by Sharif-Kashani et al. in Section 2.3.1. As before, these Eulerian time derivatives will be replaced with upper-convected derivatives that have significance independent of a moving reference frame. The upper-convected derivative of the stress tensor, $\boldsymbol{T}$, is the same shown in Equation 2.23. The upper-convected derivative for the rate-of-strain tensor follows a similar form, with notation shown below.

$$\begin{aligned} \boldsymbol{\gamma}_1 &\equiv \dot{\boldsymbol{\gamma}} \\ \boldsymbol{\gamma}_{(n+1)} &= \frac{D}{Dt}\boldsymbol{\gamma}_n - (\nabla \boldsymbol{u})^T \cdot \boldsymbol{\gamma}_n - \boldsymbol{\gamma}_n \cdot (\nabla \boldsymbol{u}) \end{aligned} \tag{2.25}$$

As before, D/Dt specifies a material derivative defined in Equation 2.21. Finally, the partial time derivatives from Equation 2.24 can be replaced with their upper-convected forms to yield the upper-convected Jeffreys, or Oldroyd-B, model shown below.

$$\boldsymbol{T} + \lambda_1 \boldsymbol{T}_{(1)} = \eta_0 \left(\boldsymbol{\gamma}_{(1)} + \lambda_2 \boldsymbol{\gamma}_{(2)} \right) \tag{2.26}$$

Oldroyd-B is a desirable model because it yields qualitatively accurate data in many situations and has been widely studied and documented. However, many viscoelastic properties are not captured by this model; specifically, there are singularities leading to infinite viscosity in certain strain-rate regimes. Additionally, Neither the Oldroyd-B nor upper-convected Maxwell models capture shear-thinning effects, something that has been observed experimentally in chopped vitreous by Sharif-Kashani et al., which may significantly affect the behavior of non-Newtonian fluids [47]. This motivates the investigation of other, non-linear differential models, specifically, the well-researched Giesekus model.

Giesekus Model

Giesekus developed his nonlinear model with strong physical ties to polymer solution ideas [14]. Treating the polymer molecules as long chains, his model introduces an anisotropic drag force constant which depends on the stress tensor. Since this nonlinear model captures many of the viscoelastic behaviors seen experimentally by Sharif-Kashani et al., and discussed in Section 2.3.1, the Giesekus constitutive equation has been implemented to model vitreous. Equation 2.27 shows the basic constitutive equation.

$$\boldsymbol{\tau} + \frac{\alpha\lambda_1}{\eta_0}\boldsymbol{\tau}^2 + \lambda_1\boldsymbol{\tau}_{(1)} = 2\eta_0\boldsymbol{D} \tag{2.27}$$

Where η_0 and λ_1 are, as before, parameters corresponding to the zero-shear viscosity and zero-shear relaxation time, respectively, and α is the model parameter attributed to anisotropic hydrodynamic drag on the constituent polymer molecules. In this case, the model is expressed not in terms of the full viscous stress tensor, $\boldsymbol{T}$, but is split into a polymer and solvent component. The polymer contribution, $\boldsymbol{\tau}$, is added to the standard Newtonian solvent response as follows.

$$\boldsymbol{T} = \boldsymbol{\tau} + 2\eta_s\boldsymbol{D} \tag{2.28}$$

Where η_s is the dynamic viscosity of the solvent component only. Substituting the full form of the upper-convected derivative, $\boldsymbol{\tau}_{(1)}$, into Equation 2.27 yields the following equation.

$$\boldsymbol{\tau} + \frac{\alpha\lambda_1}{\eta_0}\boldsymbol{\tau}^2 + \lambda_1\left[\frac{\partial\boldsymbol{\tau}}{\partial t} + \boldsymbol{u}\cdot\nabla\boldsymbol{\tau} - (\nabla\boldsymbol{u})^T\cdot\boldsymbol{\tau} - \boldsymbol{\tau}\cdot(\nabla\boldsymbol{u})\right] = 2\eta_0\boldsymbol{D} \tag{2.29}$$

Which can be rearranged to

$$\boldsymbol{\tau} + \lambda_1\left[\frac{\partial\boldsymbol{\tau}}{\partial t} + \boldsymbol{u}\cdot\nabla\boldsymbol{\tau}\right] = 2\eta_0\boldsymbol{D} + \lambda_1\left[(\nabla\boldsymbol{u})^T\cdot\boldsymbol{\tau} + \boldsymbol{\tau}\cdot(\nabla\boldsymbol{u}) - \frac{\alpha}{\eta_0}\boldsymbol{\tau}^2\right] \tag{2.30}$$

The advection term on the left-hand side, $\boldsymbol{u} \cdot \nabla \boldsymbol{\tau}$, results in instability when treated explicitly, making the method useful only for very small relaxation times [27]. To deal with this numerically problematic advection term, the semi-implicit method described by Khismatullin and Truskey is employed. Dealing with the terms on the left-hand side implicitly yields the following expression.

$$\left[\Delta t + \lambda_1 + \lambda_1 \Delta t \left(u^{n+1}\frac{\partial}{\partial x} + v^{n+1}\frac{\partial}{\partial y} + w^{n+1}\frac{\partial}{\partial z}\right)\right]\boldsymbol{\tau}^{n+1} = \lambda_1 \boldsymbol{\tau}^n + \Delta t\left[2\eta_0 \boldsymbol{D} + \lambda_1\left[(\nabla \boldsymbol{u})^T \cdot \boldsymbol{\tau} + \boldsymbol{\tau} \cdot (\nabla \boldsymbol{u}) - \frac{\alpha}{\eta_0}\boldsymbol{\tau}^2\right]\right] \tag{2.31}$$

Where the n superscript indicates the current time level, and $n+1$ the next time level. This semi-implicit scheme solves the stability problem, but is very computationally expensive due to the inversion of a large, sparse matrix. Thus, a factorization technique is employed to effectively invert the terms on the left-hand side [57].

$$(\Delta t + \lambda_1)\left[1 + \frac{\lambda_1 \Delta t}{\lambda_1 + \Delta t}u^{n+1}\frac{\partial}{\partial x}\right]\left[1 + \frac{\lambda_1 \Delta t}{\lambda_1 + \Delta t}v^{n+1}\frac{\partial}{\partial y}\right]\left[1 + \frac{\lambda_1 \Delta t}{\lambda_1 + \Delta t}w^{n+1}\frac{\partial}{\partial z}\right]\boldsymbol{\tau}^{n+1} = \lambda_1 \boldsymbol{\tau}^n + \Delta t\left[2\eta_0 \boldsymbol{D} + \lambda_1\left[(\nabla \boldsymbol{u})^T \cdot \boldsymbol{\tau} + \boldsymbol{\tau} \cdot (\nabla \boldsymbol{u}) - \frac{\alpha}{\eta_0}\boldsymbol{\tau}^2\right]\right] \tag{2.32}$$

The inversion of the factorized left-hand side requires solving only three tridiagonal matrices, which greatly reduces computational expense. This semi-implicit scheme is valuable in simulating fluids with large relaxation times, and overcomes some of the limitations of previous computational studies of vitreous cutters [23]. Integrating this model into the method outlined at the end of Section 2.2.2 requires storing values for each independent component of the stress tensor. This requires a careful consideration of the indexing when forming the finite difference stencils due to their locations on the staggered grid. For the sake of clarity, the locations of the terms of the 3×3 stress tensor are shown in Figure 2.13.

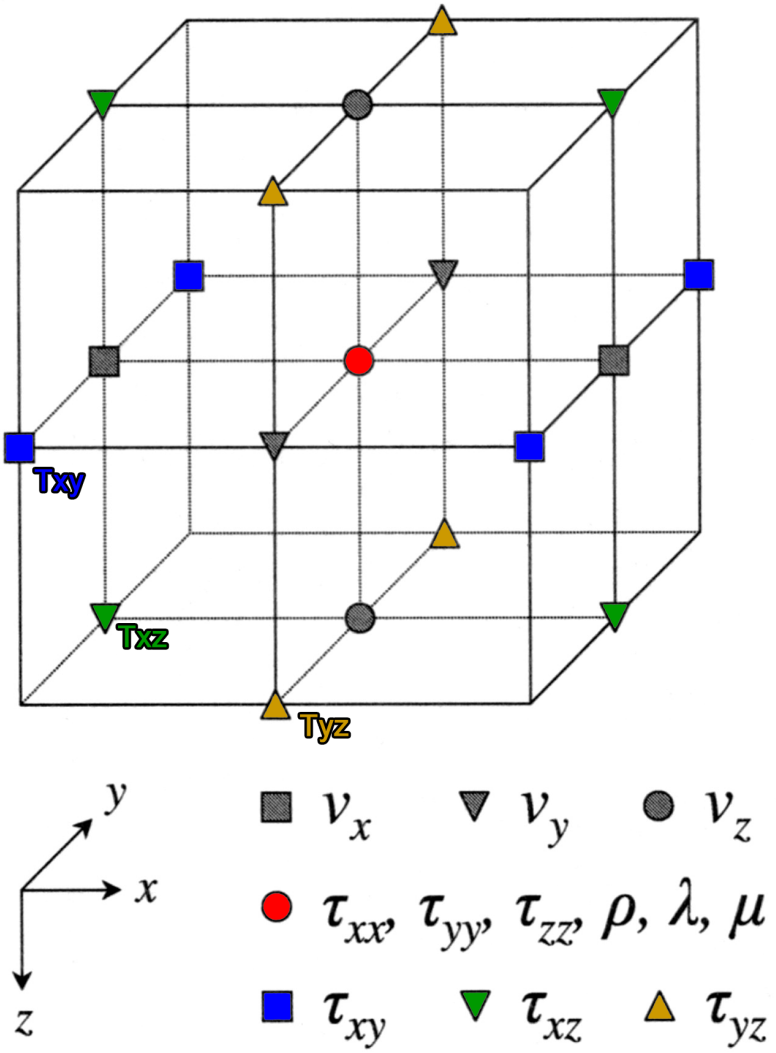

Figure 2.13: The storage locations for the stress terms on a three-dimensional grid (compare to Figure 2.6).

Chapter 3

Results

3.1 Code Verification and Validation

After implementing all the features documented in the previous chapter, attention turned to verifying and validating their performance and behavior. Careful selection of the model problems to isolate or test only a single feature at a time allowed this study to naturally "ramp up" to the case of the full, three-dimensional, viscoelastic, vitreous cutter simulations. The most important of these testing milestones are presented in the following sections.

3.1.1 Newtonian Flow Past a Cylinder

Flow past a two-dimensional cylinder is a classic problem, with no shortage of benchmark results on both computational and experimental fronts [54, 53, 35]. The objectives of this study were to first ensure that the immersed boundary treatment was working as expected, correctly identifying forcing points, interpolating values, etc., and second, to ensure that the simple shapes being used during the constructive solid geometry of the vitreous cutter were being represented as expected.

For this benchmark problem, the dimensionless diameter, D, of the cylinder was set to 1. The computational domain extended from $2D$ in the upstream direction to $10D$ in the downstream direction. A no-slip condition was enforced at the upper and lower walls which were separated by $4D$, essentially turning this into a case of flow past a cylinder in a channel. The grid spacing was uniformly $0.05D$ throughout the domain. This relatively coarse, uniform grid spacing cannot accurately resolve the thin boundary layers forming around the cylinder, and the constricted domain has an effect on the flow; thus, it is unsuitable for a high-fidelity comparison involving forces at and/or near the surface. However, for the purposes of testing the implementation of a simple immersed boundary, it was sufficient. The upstream boundary condition was prescribed a fixed velocity, $u_\infty = 1$, and a convective outflow condition was used on the downstream boundary [50]. A Reynolds number of 400 was used in this problem, with the expectation that this places the flow in the regime where a Karman vortex street should be produced,

but will not yet be in the turbulent or transition regime [54]. The resulting contour plots of downstream vorticity at four different instances is shown in Figure 3.1.

Examining the results, it is clear that the immersed cylindrical body was being implemented as expected, and that the effects of the boundary were propagating throughout the fluid. This is evidenced both by the size and location of the flow features. Additionally, for a Reynolds number of 400, the flow downstream of the immersed body shows the characteristic alternate shedding of vortices and their smooth advection downstream. The Karman vortex street in the wake of the cylinder is consistent with previous studies at similar Reynolds numbers [54, 35]. Having tested some of the most fundamental parts of the algorithm with this simple problem, the focus can turn to testing the more unique features of this solver that are specific to the study of a vitreous cutter.

3.1.2 Newtonian Poiseuille Flow

As discussed in Section 2.2.3, the computational model relies on a traction boundary condition to establish the pressure gradient responsible for the aspiration of vitreous. To verify the implementation of this crucial boundary condition, a simulation was performed to simulate pressure-driven flow, or Poiseuille flow, in a three-dimensional pipe with a square cross section. The centerline of the pipe is concurrent with the x-axis, and the dimensions in the y- and z-directions are $2b$ and $2c$, respectively. An illustration of the model setup is shown in Figure 3.2

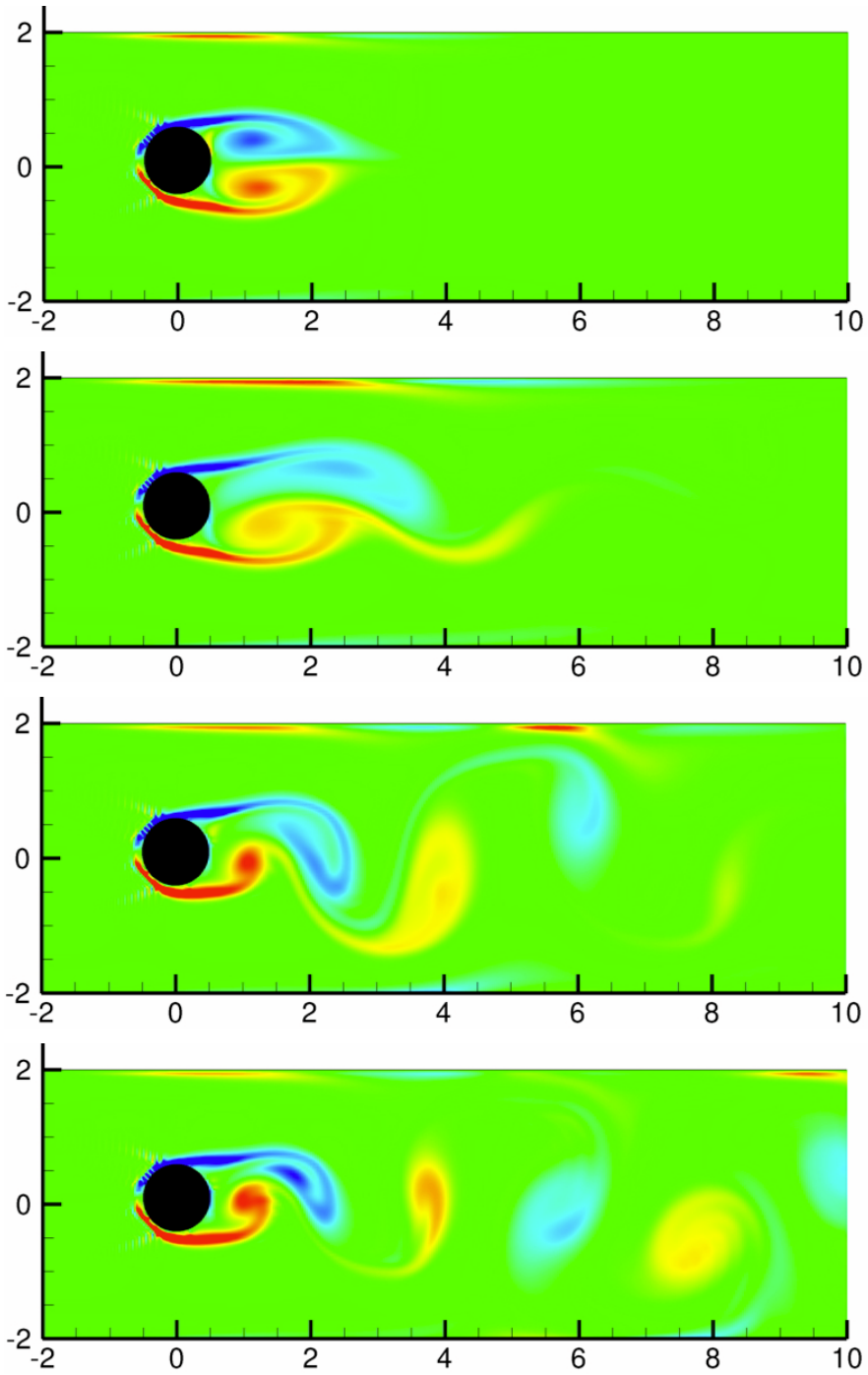

Figure 3.1: Spanwise vorticity contours showing the evolution of a Karman vortex street behind a cylindrical immersed boundary at $\mathrm{Re} = 400$, $\Delta x = \Delta y = 0.05D$.

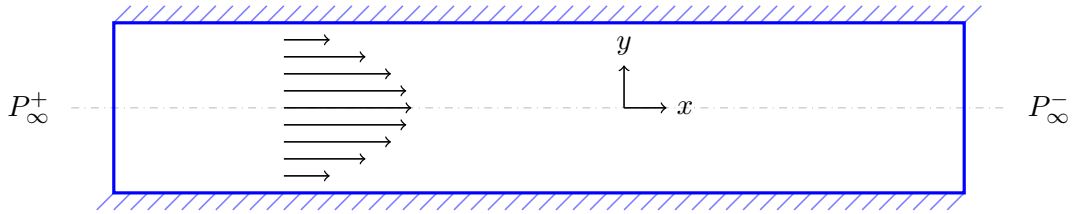

Figure 3.2: An illustration of the computational domain and boundary conditions used to simulate a pressure-driven flow, or Poiseuille flow, in a square pipe.

In Figure 3.2, P_∞^+ is a relatively high ambient pressure compared to P_∞^-. The resulting pressure gradient is expected to establish flow from the left-hand to right-hand side, as shown in the illustration. For such a three-dimensional, pressure-driven flow, the analytical velocity profile passing through the yz-plane is given by evaluating the following infinite series [9].

$$u_x(y,z) = -\frac{1}{2\eta}\frac{\partial P}{\partial x}c^2\left[1-\left(\frac{z}{c}\right)^2+4\sum_{k=1}^{\infty}\frac{(-1)^k}{\alpha_k^3}\frac{\cosh\left(\frac{\alpha_k y}{c}\right)}{\cosh\left(\frac{\alpha_k b}{c}\right)}\cos\left(\frac{\alpha_k z}{c}\right)\right] \tag{3.1}$$

where

$$\alpha_k = (2k-1)\,\frac{\pi}{2}, \qquad k = 1,2,3,\ldots$$

As noted before, the dimensions of the pipe in the y- and z-directions are $2b$ and $2c$, respectively. Additionally, η is the dynamic viscosity of the fluid, and dP/dx is the pressure drop along the length of the pipe. To ensure that traction conditions alone were responsible for any resulting flow, the simulation was initiated in a quiescent fluid,

i.e., initial conditions set to zero throughout the domain. The velocity profile established by the traction boundary condition is shown in Figure 3.3.

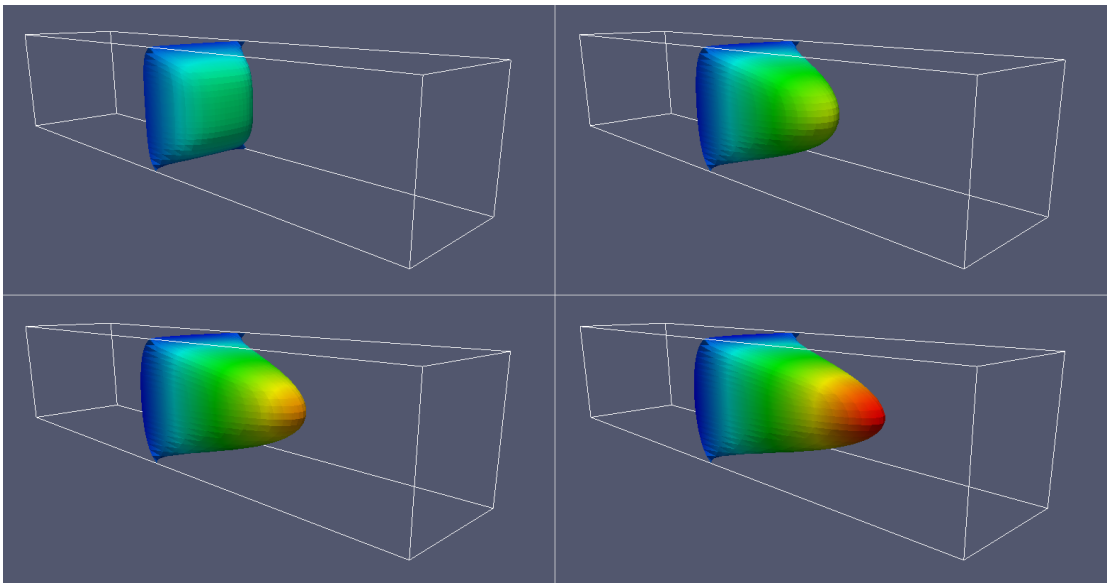

Figure 3.3: Evolution to a steady-state velocity profile for a pressure-driven fluid in a square tube, Re $= 100$, $2b = 2c = 1$, $L/2b = 5$, $dP/dx = -0.1$.

The infinite series representing the analytical solution to Poiseuille flow in a square tube was calculated to ≈ 20 terms, at which point the percent error between successive terms becomes less than 1×10^{-12}. The simulation results were compared to this analytical solution to verify the traction boundary condition. The results are shown in Figure 3.4.

Examining the plot in Figure 3.3, the traction boundary condition is capable of establishing a steady-state Poiseuille flow in a quiescent fluid. Additionally, as shown in Figure 3.4, the results compare very favorably to the analytical solution, inspiring confidence in studies with more complex and potentially moving geometry.

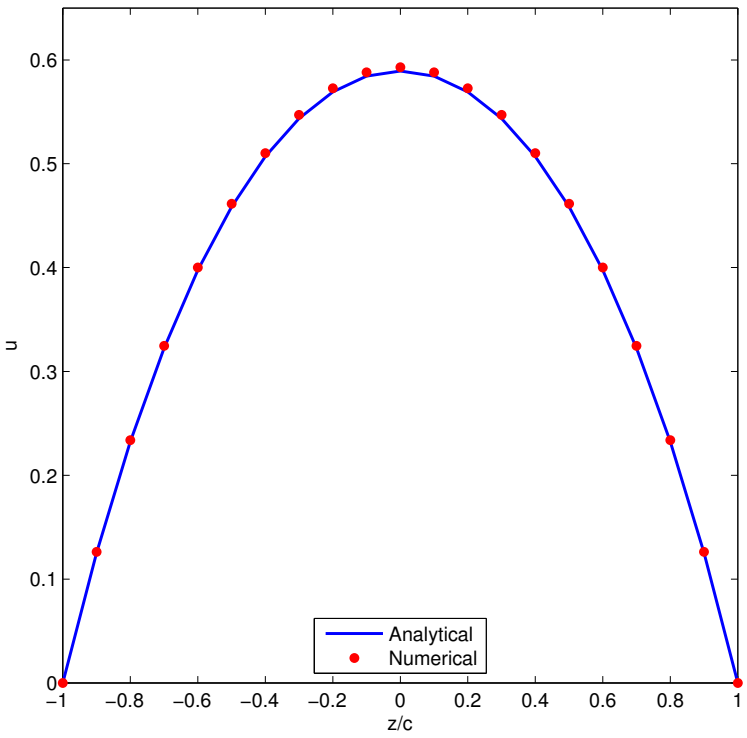

Figure 3.4: The analytical and numerical steady-state velocity profile taken along the z-axis at the center of the computational domain.

3.1.3 Viscoelastic Poiseuille Flow

Accurately capturing the viscoelastic nature of the vitreous is central to future studies. To this end, the Giesekus constitutive equation has been implemented alongside the existing fractional-step algorithm as discussed in Section 2.3.2. To verify the Giesekus solver, a two-dimensional simulation of Poiseuille flow with a viscoelastic liquid was constructed. The computational model is identical to the one described in Section 3.1.2; however, in this case, the standard viscous term in the Navier-Stokes equation has been replaced with the stress tensor calculated with the semi-implicit implementation of the

Giesekus constitutive equation. A relatively simple analytical expression for the velocity profile exists when the nonlinear Giesekus parameter, α, is equal to 0.5 and the solvent viscosity, η_s, is zero [56, 10].

$$u_x(y) = -\frac{1}{2\mathrm{We}^2 \frac{dP}{dx}} \ln \frac{1 - \mathrm{We}^2 \left(\frac{dP}{dx}\right)^2 y^2}{1 - \mathrm{We}^2 \left(\frac{dP}{dx}\right)^2} \tag{3.2}$$

Where dP/dx, represents the pressure drop along the axial direction of the pipe, as previously discussed. The additional term in Equation 3.2, We, is the Weissenberg number, an important dimensionless quantity that arises in the study of viscoelastic fluids. The Weissenberg number is a ratio of the polymer relaxation time, λ_1, to the time scale of the fluid [5].

$$\mathrm{We} = \frac{\lambda_1 U_{\mathrm{ref}}}{L_{\mathrm{ref}}} \tag{3.3}$$

Conceptually speaking, the Weissenberg is an indication of a fluid's elasticity. As the relaxation time increases, elastic effects dominate, and the fluid behaves more like a solid. At small relaxation times, or long fluid time scales, viscous effects dominate and the fluid behaves more like a liquid. A Weissenberg number of zero indicates a purely Newtonian fluid, and an infinite Weissenberg number indicates a purely elastic solid. The analytical results for a fluid with Weissenberg number of 0.6 are shown in Figures 3.5-3.6.

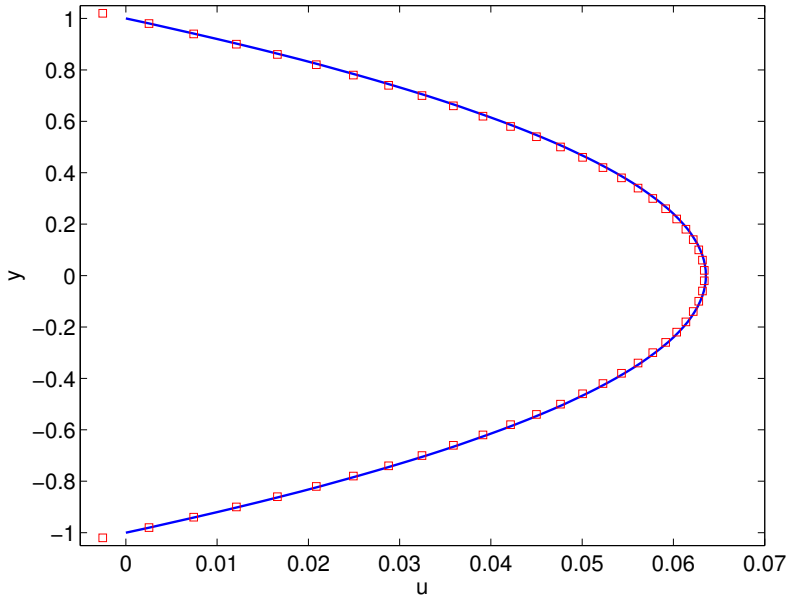

Figure 3.5: The analytical (solid) and numerical (markers) steady-state velocity profile taken along the y-axis at the center of the computational domain.

The agreement between the analytical and numerical solutions is quite strong, suggesting that the Giesekus solver is working as expected. Since the Poiseuille flow was driven by the traction boundary condition, this simulation also demonstrates the compatibility of a traction boundary when implemented alongside the viscoelastic solver.

3.1.4 Viscoelastic Contraction Flow

An interesting canonical problem in the study of viscoelastic fluids is pressure-driven flow through a 4:1 contraction. This example builds on the viscoelastic Poiseuille flow in Section 3.1.3 in that it introduces a simple immersed boundary and additional rheological properties. The basic geometry of the problem is shown in Figure 3.7.

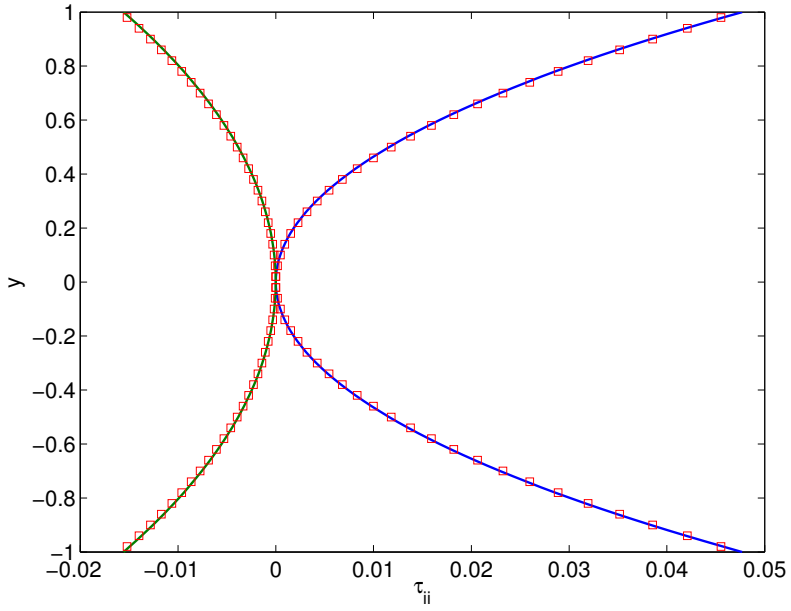

(a) The normal stresses, τ_{yy} (left) and tau_{xx} (right).

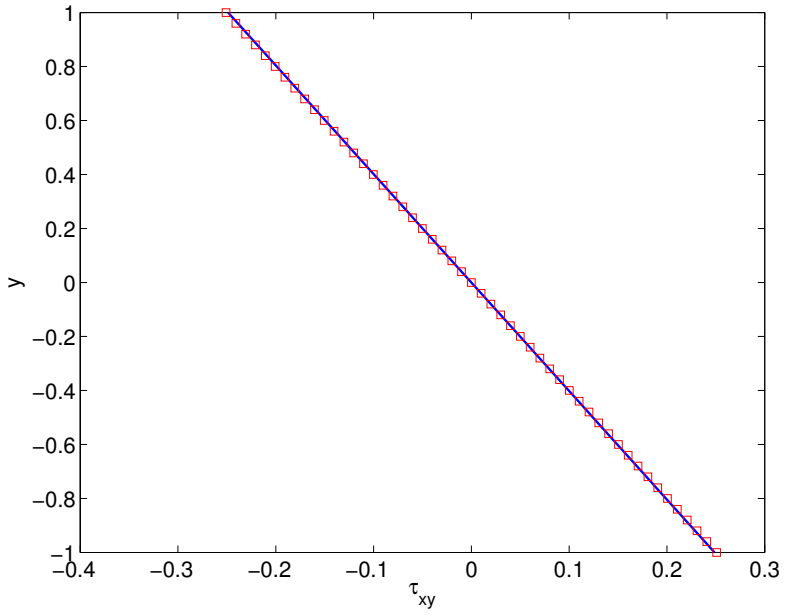

(b) The shear stress, τ_{xy}.

Figure 3.6: Analytical (solid) and numerical (markers) steady-state stress values taken along the y-axis at the center of the computational domain.

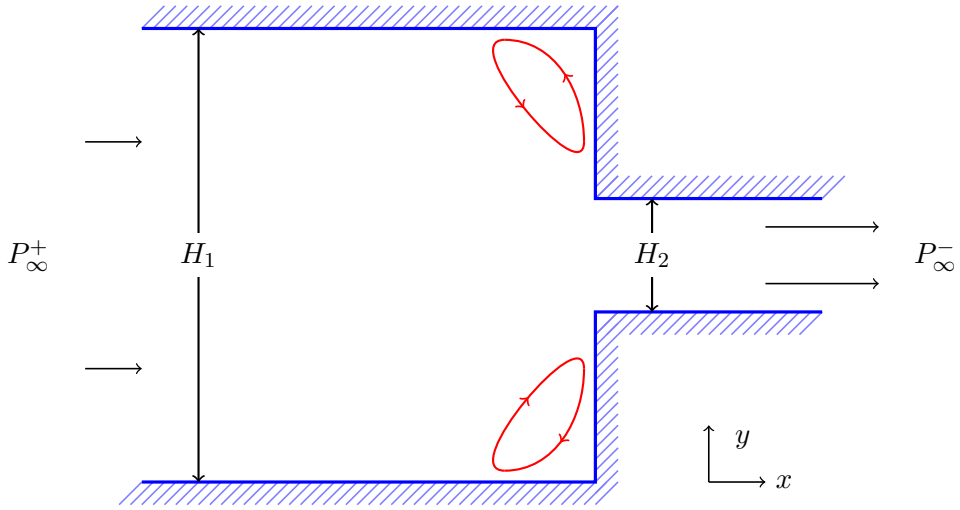

Figure 3.7: The geometry of the 4:1 contraction problem.

Flow is moving from the left-hand side to the right-hand side due to a pressure gradient. To test the three-dimensionality of the Giesekus implementation, the computational domain was extended in the z-direction (into the page). The resulting geometry and flow field is shown in Figure 3.11.

As the fluid is forced through the constriction, two symmetric recirculation zones appear in the upper and lower corners. This is a valuable litmus test for an implementation of the Giesekus constitutive model because there are two distinct fluid responses based on the choice of the Giesekus nonlinear parameter. In the case where there is no shear-thinning behavior, i.e., $\alpha = 0$, only the effects of elasticity are modeled, and the recirculation zones shrink with increasing Weissenberg number. Conversely, when shear thinning is introduced, i.e., $\alpha \neq 0$, the opposite behavior is observed. That is, the recirculation zones increase in size with increasing Weissenberg number.

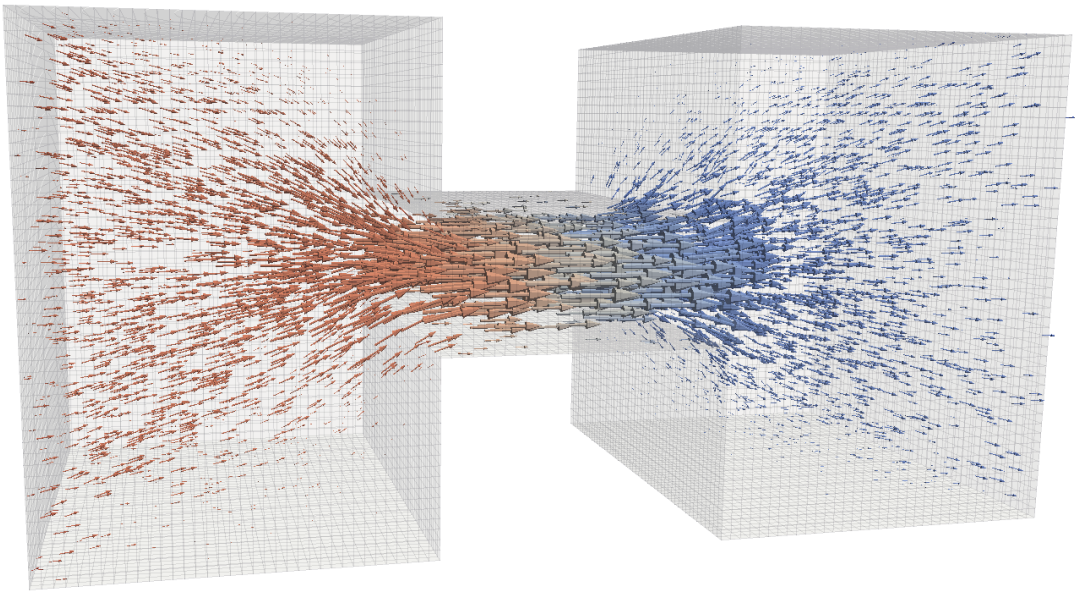

Figure 3.8: The three-dimensional computational domain, and the resulting velocity field colored by pressure.

$$\alpha = \begin{cases} 0, \text{ elasticity only} \\ \\ 0.5, \text{ elasticity + shear thinning} \end{cases}$$

For this problem, the dimensionless pressure gradient, dP/dx, is set to -1.0. The ratio of solvent viscosity to total viscosity, η_s/eta_0, is set to 1/9. Qualitative comparisons are made with the benchmark results presented by Alves et al. in their 2003 publication [2]. The results when no shear thinning is present are shown in Figure 3.9.

Examining the streamlines defining the recirculation zones in Figure 3.9, the Giesekus implementation is clearly able to reproduce the characteristic shrinking of the recirculation zones in the case where the fluid has only elastic effects present. The addition of

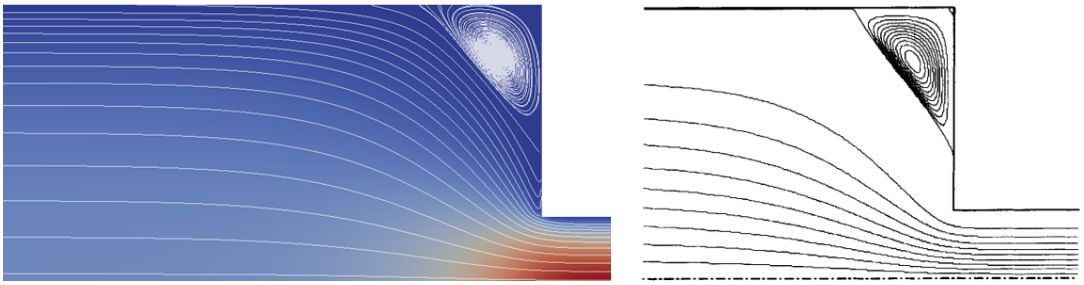

(a) We = 0

(b) We = 0

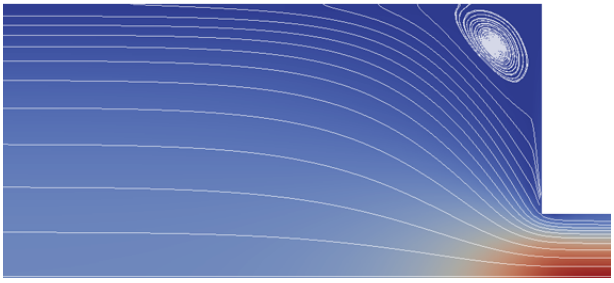

(c) We = 1.5

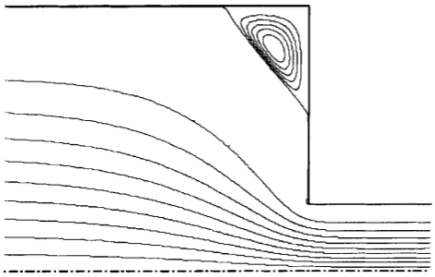

(d) We = 1.5

Figure 3.9: Comparison of 4:1 contraction with no shear thinning ($\alpha = 0$) to Alves et al., $dP/dx = -1.0$, $\eta_s/eta_0 = 1/9$ [2].

shear thinning is presented in Figure 3.10.

In the case where shear thinning is present, an increase in Weissenberg number leads to the growth of the recirculation zones formed ahead of the contraction. Passing this important qualitative test, when considered alongside the strong quantitative agreement presented in Section 3.1.3, suggests the the Giesekus implementation is working as expected. With confidence in the model, the focus can now turn to the problem of the vitreous cutter.

3.2 Newtonian Simulations

Following the creation of the vitreous cutter signed distance function and the verification of the traction boundary condition, a preliminary study was performed to study the flow through a vitreous cutter operating in a Newtonian fluid. The exact dimensions and geometry of the computational model were obtained from measurements of a 20-gauge pneumatically-operated vitreous cutter manufactured by Alcon Laboratories of Fort Worth, Texas. Since the non-Newtonian characteristics of vitreous were not considered in this study, a Newtonian analog with the fluid properties of egg white—a common substitute during in vitro experimentation—was employed. These properties are surmised in Table 3.1.

The cutting dynamics were loosely interpreted from analysis of a high-speed film central to the research of different vitrectomy systems by Hubschman et al. [18]. More will be

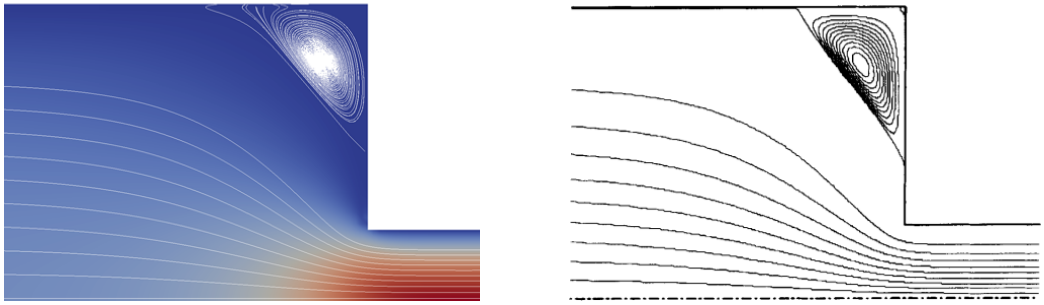

(a) We = 0 (b) We = 0

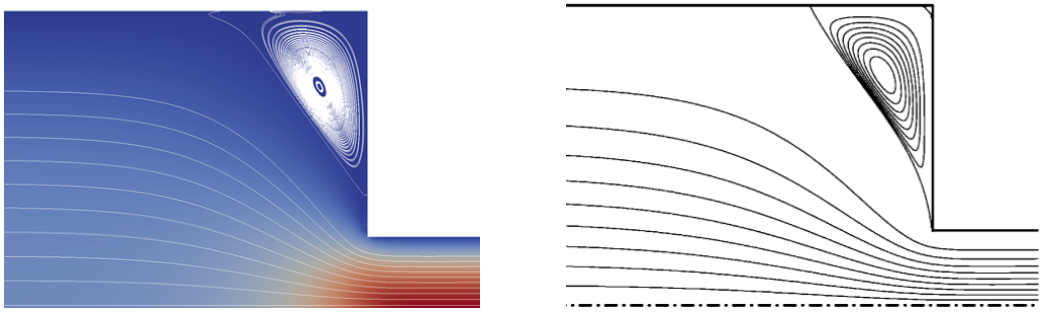

(c) We = 2.5 (d) We = 2.5

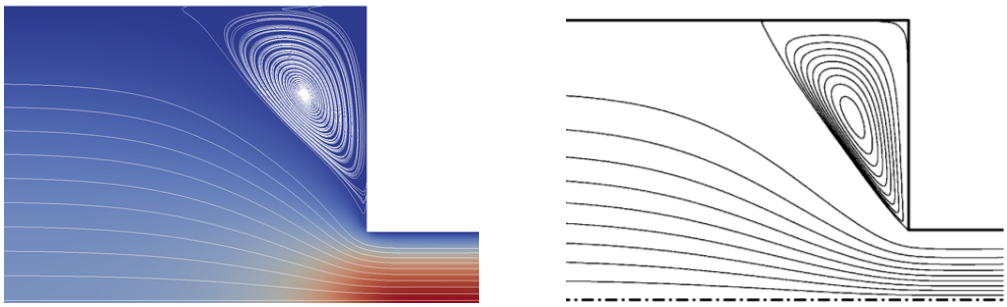

(e) We = 10.0 (f) We = 10.0

Figure 3.10: Comparison of 4:1 contraction with shear thinning ($\alpha = 0.5$) to Alves et al., $dP/dx = -1.0$, $\eta_s/eta_0 = 1/9$ [2].

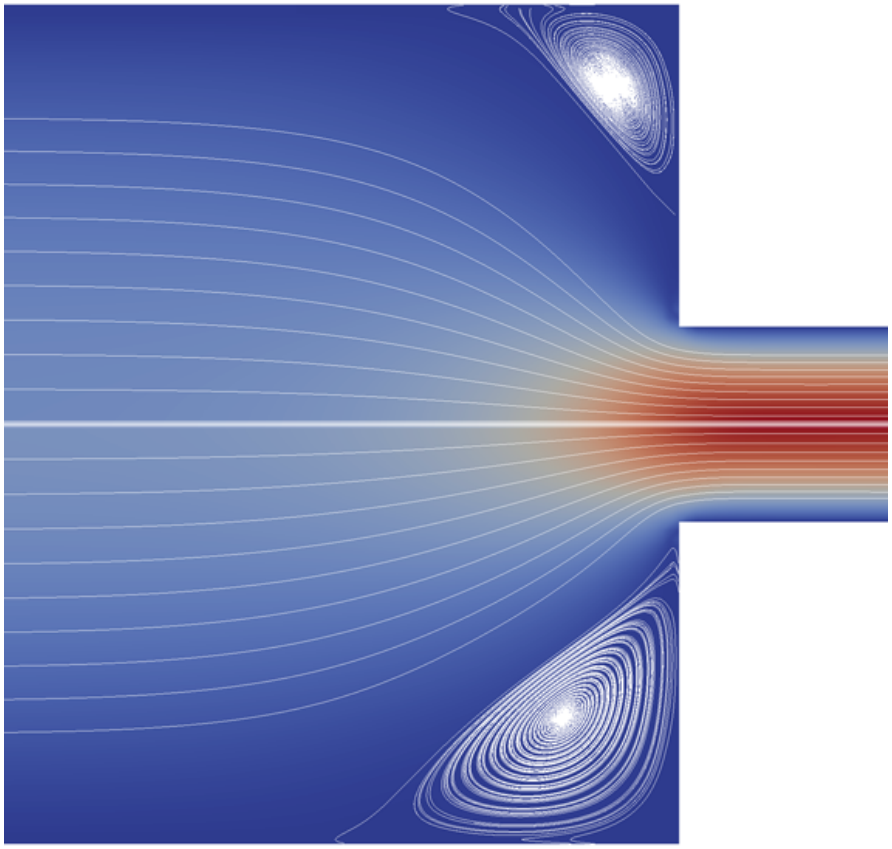

Figure 3.11: Comparing the recirculation zone for a Newtonian fluid (top) and a viscoelastic fluid with shear thinning, We = 10.0 (bottom).

said about these results in Section 3.3. The total time required for the opening, open, closing, and closed events define the cut rate, which for this preliminary study was 2000 CPM. Additionally, these time windows define the velocity at which the guillotine cycles, which was found to have an effect on the flow features around the orifice [18, 24]. Velocity at the guillotine surface is enforced by setting a non-zero velocity value at the interface in the direct forcing step of the algorithm, covered in detail in Section 2.2.2. The outer shaft of the vitreous cutter is treated as a stationary wall. The time frames

Table 3.1: Fluid parameters and cutter dimensions; values with the * notation use the same labeling as Figure 2.1.

Physical Parameter	Value
Density (ρ)	1038 kg/m^3
Viscosity (μ)	4.5 mPa·s
Outer Diameter* (D)	910 μm
Inner Diameter* (A-2·tt)	475 μm
Orifice Radius* (O)	237 μm

used in this study are shown in Table 3.2.

Table 3.2: Duration of cutting phases corresponding to 2000 CPM.

Opening	Opened	Closing	Closed
3.2 ms	7.7 ms	3.2 ms	15.6 ms

During a modern vitrectomy, fluid is infused into the posterior cavity while the vitreous is being removed. This simultaneous infusion and removal allows the intraocular pressure to be maintained, preventing collapse of the eye. The normal intraocular pressure maintained by healthy vitreous ranges from 12-22 mmHg [1]. In this study, it is assumed that the tip of the cutter is sufficiently removed from the inner eye wall, that pressure fluctuations due to guillotine motion are restricted to the area around the cutter, and that the infusion ideally stabilizes the intraocular pressure. With these assumptions, the intraocular pressure can be assumed to be constant on all walls of the truncated computational domain. The normal traction on these boundaries is set to zero, and the

resultant pressure difference will be entirely accounted for at the vitreous cutter outlet. This method of boundary segmentation is shown in Figure 3.12.

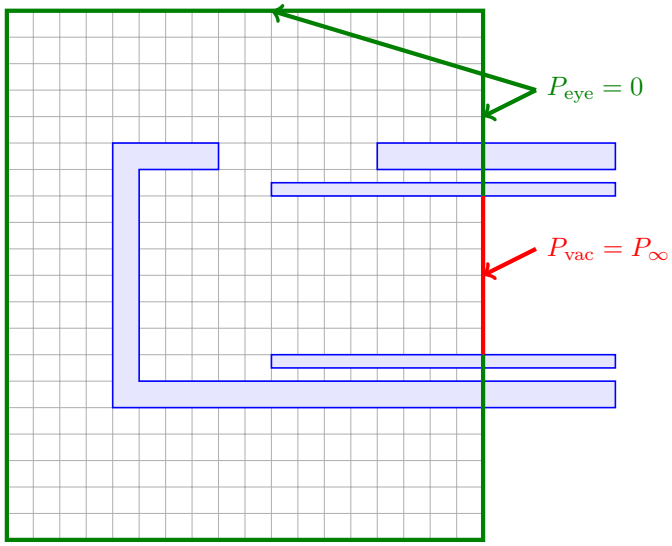

Figure 3.12: Not-to-scale illustration of the boundary segmentation, where P_{vac} is the gauge pressure relative to normal intraocular pressure.

The aspiration pressure is set by a vacuum pump attached to the distal end of the vitrectomy system. Between the cutting zone modeled in this study and the console controlling the vacuum is a long, unmodeled tube through which the chopped vitreous flows. The pressure drop in this extended domain is approximated using Poiseuille's law [23]. The manufacturer recommends a 250 mmHg vacuum pressure, which corresponds to a pressure of 14.869 mmHg at the edge of the truncated domain; however, since the goal with this study was only to verify that all the elements could function together, a lower, more computationally stable aspiration pressure, 3.242 mmHg, was used. This value is on the low end of what could be used clinically, while still providing relevant results.

The simulation was initialized in a quiescent fluid, similar to what a vitreous cutter would encounter at the beginning of an actual vitrectomy. At time $t = 0$, the traction boundary conditions were initialized, and entrainment into the vitreous cutter began. It is important to note that fluid was already present in the internal cutter shaft at initialization, such that the vitreous-air interface that would normally be present at start up was not modeled. The cutting dynamics were not started until the flow had reached a steady state. This decision to begin aspiration without moving the guillotine was made after testing showed that the simulation tended to become unstable if the guillotine movement began immediately, attributed to the sudden "shock" of starting a relatively high-velocity shearing motion against the direction of the pressure gradient. The resulting entrainment into the stationary vitreous is shown in Figure 3.13.

The flow field in this cross section looks quite natural, and does not seem to exhibit a directionality or other bias. The immersed boundary is working as intended, with no slip and no flow-through being enforced at all interfaces. Additionally, the section of guillotine modeled is long enough to allow the flow to fully develop, exhibiting a symmetric, parabolic velocity profile at the outlet. By integrating the velocity passing through a circular plane inside the guillotine shaft, the flow rate at steady state can be calculated, the resulting plot is shown in Figure 3.14.

With the computational domain now seeded with an entrainment initial condition, the guillotine motion was initialized. The time frames given in Table 3.2 were used to define opening and closing velocities, which were enforced at the surface of the immersed

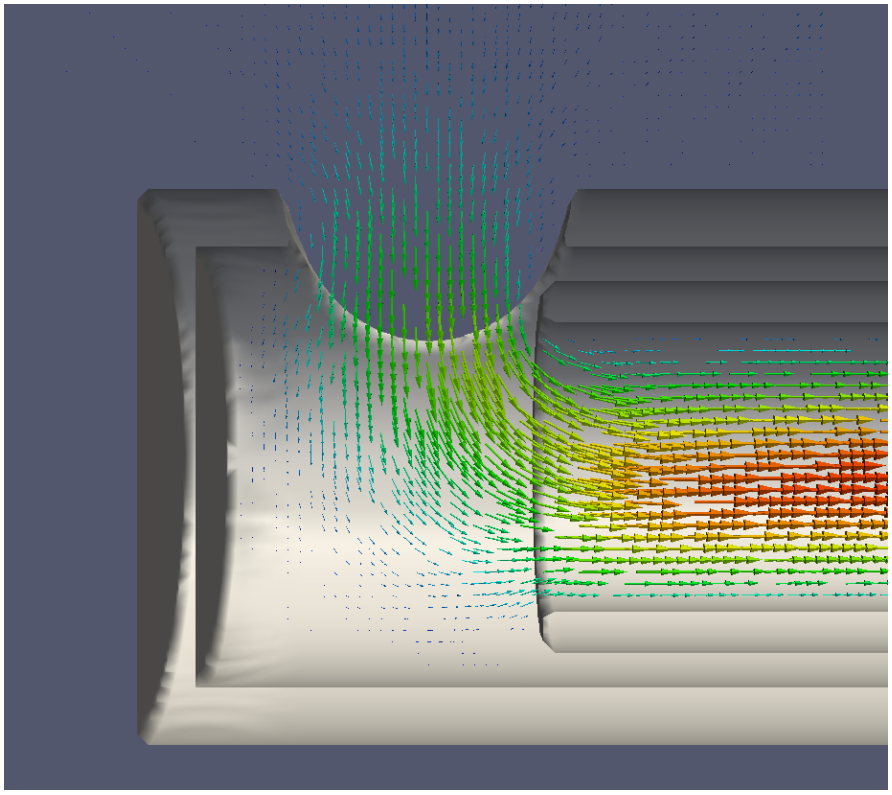

Figure 3.13: Flow field, colored by velocity magnitude, of the steady-state entrainment of Newtonian fluid into the stationary, open vitreous vitreous cutter.

boundary during the interpolation step described in Section 2.2.2. After a full two cycles, the results were processed, yielding the flow fields shown in Figure 3.15.

As with the stationary, open cutter, the flow across a circular plane bounded by the inner guillotine walls was integrated and plotted over time to show the flow rate through the operational cutter. The flow rate is shown in Figure 3.16.

The flow field snapshots in Figure 3.15 can be better understood in relation to the plot of flow rate in Figure 3.16, and will be addressed in four stages.

1. Closing: As the guillotine moves toward the end of the cutter, the core of fluid it

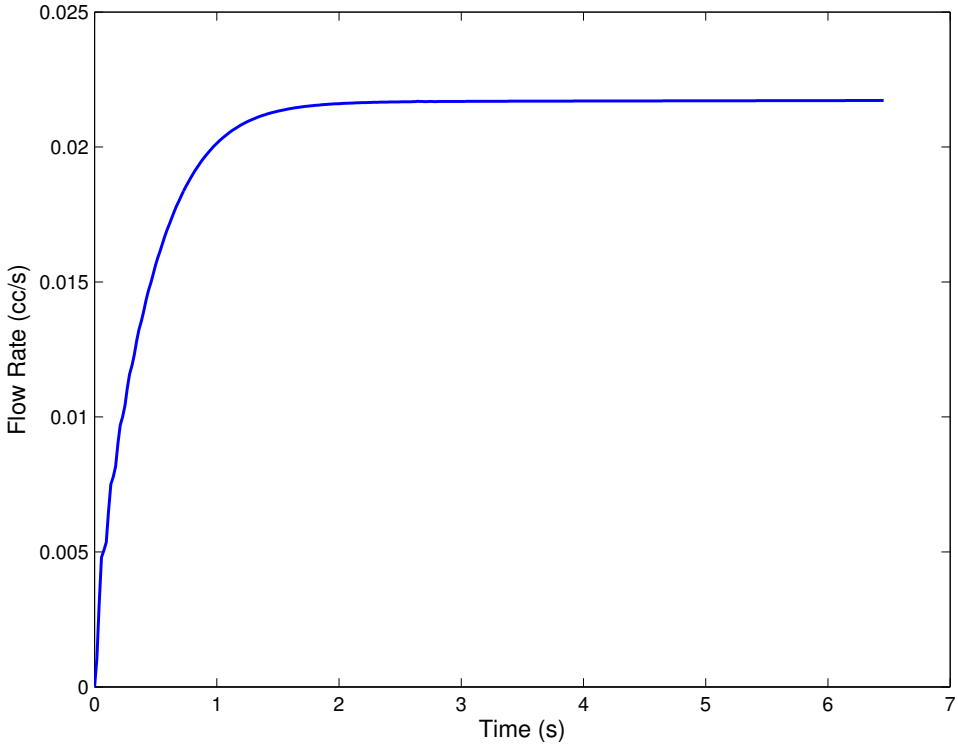

Figure 3.14: The dimensional flow rate inside the stationary guillotine shaft, showing that a steady state is achieved.

contains begins moving against the direction of traction. A high-pressure region forms ahead of the cutting edge of the guillotine, causing a small amount of ejection through the orifice, as seen in Figure 3.24(a). The flow rate during this period drops off sharply, as expected. As the core of fluid move with the guillotine, the flow rate eventually becomes negative. This stops when the cutter is significantly close to contacting the outer wall, at which point the flow rate begins approaching zero.

2. Closed: When the guillotine makes contact with the stationary outer wall, the flow

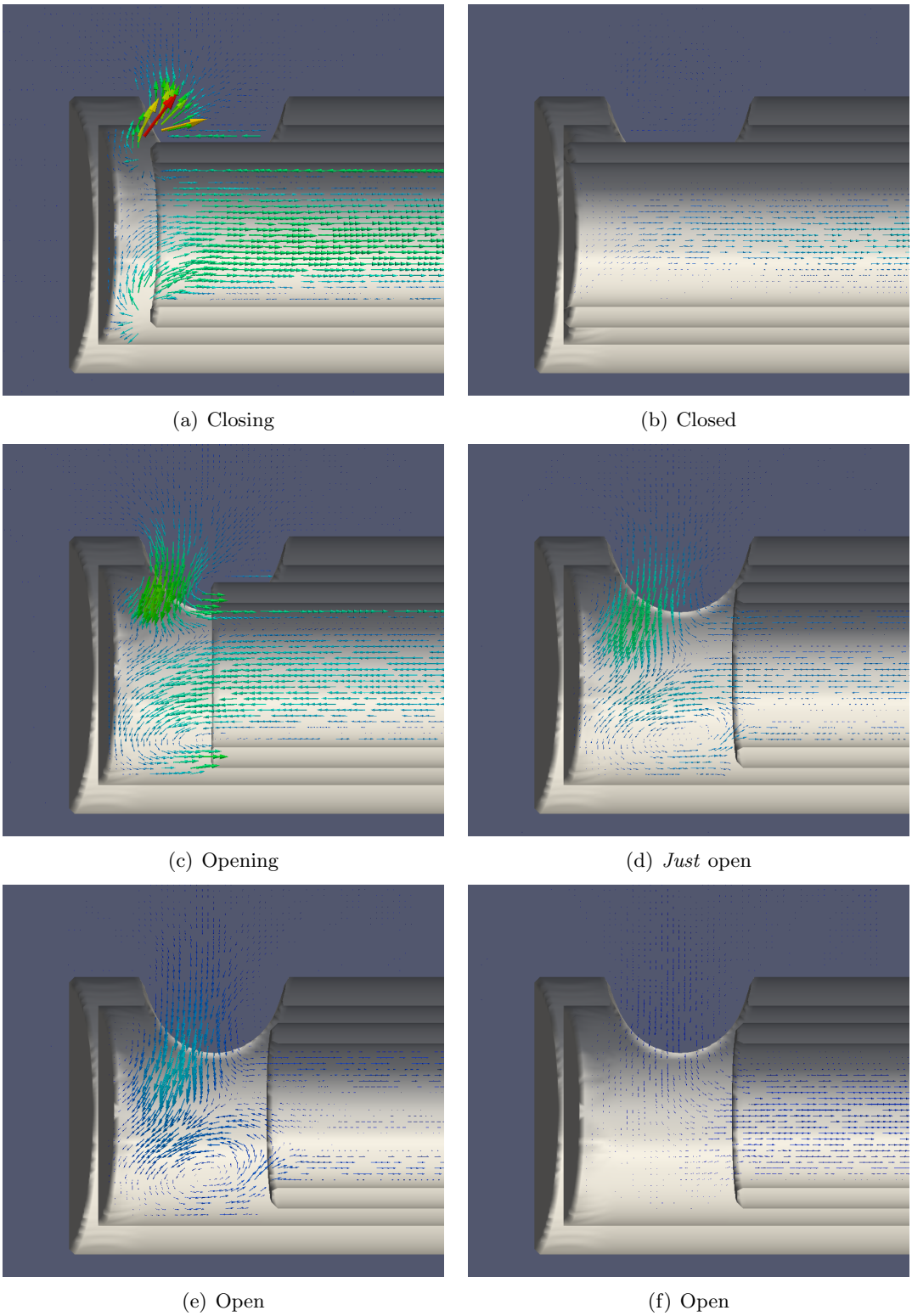

(a) Closing

(b) Closed

(c) Opening

(d) *Just* open

(e) Open

(f) Open

Figure 3.15: The flow field, colored by overall velocity magnitude, at different points in a 2000 CPM cycle.

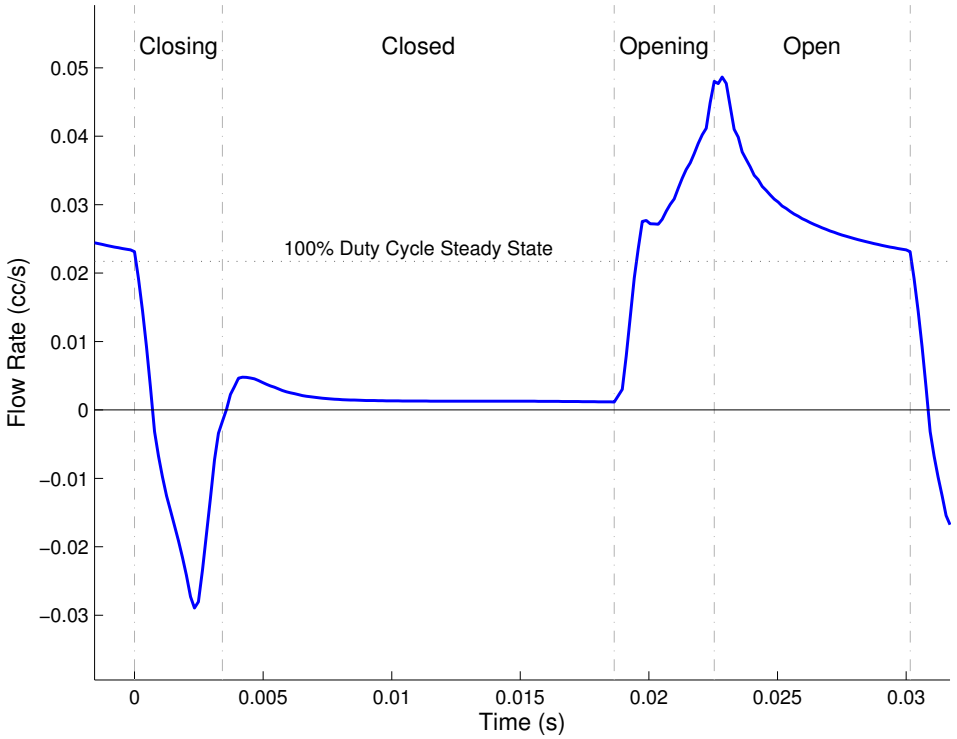

Figure 3.16: The dimensional flow rate inside the moving guillotine shaft, divided into four phases and the steady-state flow rate.

rate drops to a near-zero value and remains there for the duration of the closed phase. The flow is not identically zero, because a small gap between the guillotine and wall is allowed to avoid a computationally problematic pressure discontinuity between the two separated regions, as documented by Juan et al. [23].

3. Opening: As the guillotine begins opening, the core of fluid it contains is accelerated out of the device, causing a positive spike in flow rate. The low-pressure region left in the void draws fluid in the cutter, creating a small region of vorticity opposite the orifice, seen in Figure 3.20(a).

4. Opened: After reaching the fully-open position, the fluid decelerates, as it is no longer being "pulled" along by the guillotine. The flow rate nearly returns to the steady-state value corresponding to a vitreous cutter operating at 100% duty cycle before the next cutting begins.

Although these results do not take into account the viscoelastic nature of vitreous, they still provide some insight into the behavior of the device, and the behaviors observed seem to be in agreement with previous computational studies [23, 24]. The velocity of the guillotine is responsible for many of the flow features observed, including the small portion of vitreous ejected during closing and the large increase in flow rate as the cutter slowly opens. From here, the study moves on to the more interesting problem, which attempts to account for the viscoelastic nature of this complicated biofluid.

3.3 Viscoelastic Results

3.3.1 Flow Rate

Following the implementation of the Giesekus constitutive equation to model the gel-like nature of the vitreous, attention turned to performing a more in-depth study of the conditions present during vitrectomy. As in Section 3.2, the dimensions of the cutters being studied are presented first. Table 3.3 shows the critical dimensions of both a 20- and 23-gauge cutter manufactured by Alcon Laboratories of Fort Worth, Texas.

Table 3.3: Dimensions of a 20- and 23-gauge vitreous cutter [18].

Property	20-Gauge	23-Gauge
Outer Diameter	900 μm	630 μm
Guillotine Outer Diameter	640 μm	460 μm
Guillotine Inner Diameter	475 μm	355 μm
Orifice Radius	249 μm	229 μm
Vacuum Pressure (P_{vac})	250 mmHg	550 mmHg

As expected, the 23-gauge cutter is a thinner instrument. Perhaps most importantly, the cross-sectional area inside the guillotine of the 23-gauge cutter is only 55.8% the size of its 20-gauge counterpart. Because of this, the manufacturer recommends increasing the vacuum pressure from 250 to 550 mmHg.

The orifice radius corresponding to a 20-gauge vitreous cutter is slightly different from that reported for the Newtonian simulation in Section 3.2. This is not an oversight, but rather, the result of improving the technique used to calculate the aperture radius implied by measurements of the port area performed by Hubschman et al. [18]. Additionally, the outer diameter has been adjusted to reflect Hubschman's measurements. To better see the differences between the 20- and 23-gauge cutter, a scale rendering created from the signed distance fields is shown in Figure 3.17.

To determine the duration of each cutting phase, Hubschman et al. used a high-speed camera to record the tip of different vitreous cutters operating in a beaker filled with

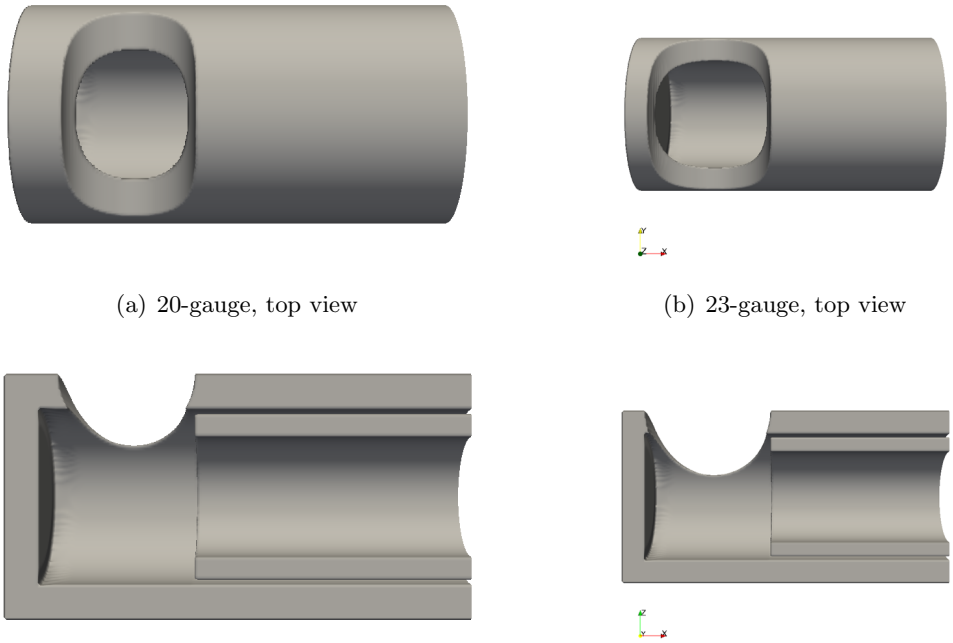

(a) 20-gauge, top view

(b) 23-gauge, top view

(c) 20-gauge, cut-away view

(d) 23-gauge, cut-away view

Figure 3.17: To-scale comparison of the 20-gauge and 23-gauge vitreous cutter geometry, generated by the zero iso-surface of the signed distance field.

porcine vitreous [18]. Opening time was defined as the elapsed time between the first frame of guillotine motion and the frame where the guillotine disappeared from view. The time in the open state was measured between the end of the opening time and the start of the closing time. The closing time was defined as the elapsed time between the guillotine reappearing in the cutting port and the guillotine reaching a stationary position. The time in the closed state started at the end of closing time and ended at the start of opening time [18]. The results for both 20- and 23-gauge vitreous cutters are shown in Table 3.4.

The Reynolds numbers for all the cases shown in Table 3.4 are calculated using the

Table 3.4: The duration of the different cutting phases for different cut rates.

	Cutting-Phase Duration (ms)					
Cuts/Minute	Opening	Opened	Closing	Closed	Duty Cycle (%)	Reynolds
20-gauge						
1,500	7.2	15.2	2.7	14.6	50.8	2.2
2,500	7.7	0.4	2.1	13.4	22.5	2.9
23-gauge						
1,500	4.9	19.8	1.8	12.7	59.1	1.9
2,500	4.8	5.3	2.3	11.0	37.9	1.4

closing speed of the guillotine as the reference velocity, and the outer diameter (from Table 3.3) as the reference length. The closing velocity is determined from the time measured by Hubschman et al. combined with a calculation of the distance the guillotine must travel to span the cutting port and contact the stationary outer wall, where the travel distance is based on the assumption that the guillotine stops in the fully open position directly under the edge of the cutting port. The additional physical properties used in the calculation of Reynolds number are shown in Table 3.5.

Table 3.5 also restates the relaxation time, λ_1, and retardation time, λ_2, that correspond to chopped vitreous processed at 2000 CPM. As presented in Section 2.3.1, these values change depending on exactly how the vitreous was fragmented. Sharif-Kashani et al. report values for 500, 2000, and 2500 CPM. Hubschman et al. report experimental flow rates and cutting dynamics for only the cases of 1500 and 2500 CPM. Rather than rely

Table 3.5: The physical properties of vitreous chopped at 2000 CPM.

Vitreous Parameter	Value
Density (ρ)	1038 kg/m^3
Total Viscosity (η_0)	0.09 Pa·s
Relaxation Time (λ_1)	3.60 s
Retardation Time (λ_2)	0.14 s
Mobility Factor (α)	0.02 Pa·s

on an ad hoc interpolation routine, the rheological properties of vitreous chopped at 2000 CPM are used in the studies of a cutter operating at 1500 CPM.

At this point, it is appropriate to address one of the most critical assumptions made in these viscoelastic studies. There is currently no method in place to mark and follow the separation line between the chopped vitreous and the intact vitreous inside and outside the cutter, respectively. As such, *all of the vitreous in the computational domain will be treated as the chopped consistency.* This simplification is acceptable because one of the primary optimization points for a vitrectomy system is the flow rate through the device. In order to accurately gauge this behavior, and compare with the experimental work of Hubschman et al., the vitreous must exhibit the liquid-like behavior that allows it to be suctioned from the eye. The second important consideration, disturbances near the cutting port and moving guillotine, are still attainable with this assumption. Although the chopped vitreous will undoubtedly propagate stresses differently than the more

realistic intact vitreous would, qualitative comparisons can still be made to determine which systems and operating parameters are more destructive than others. It is expected that any trends observed in the disturbances generated in chopped vitreous would be qualitatively (if not quantitatively) similar to those generated in intact vitreous. The importance of accounting for spatially-varying rheology could provide an important extension of the current studies, and will be addressed further in Section 4.2.

As before, the aspiration pressure is set by a vacuum pump attached to the distal end of the vitrectomy system. As described in Section 3.2, the manufacturer recommends a 250 mmHg vacuum pressure for the 20-gauge cutter, which corresponds to a pressure of approximately 15 mmHg at the edge of the truncated domain. As in the Newtonian simulations, it is assumed that the infusion tube works ideally; thus, the intraocular pressure is perfectly maintained, and a constant ambient pressure can be set on all walls of the computational domain. In these viscoelastic studies, an impedance-matching pressure condition has been introduced. This extension of the traction boundary condition monitors the flow rate through the guillotine, and adjusts the vacuum pressure at the truncated domain according to Poiseuille's Law.

After establishing the geometry, cutting dynamics, rheological properties, and the boundary conditions, the first of the viscoelastic simulations began. The flow field at different stages in the cutting cycle of a 20-gauge vitreous cutter operating at 1500 CPM is shown in Figure 3.18.

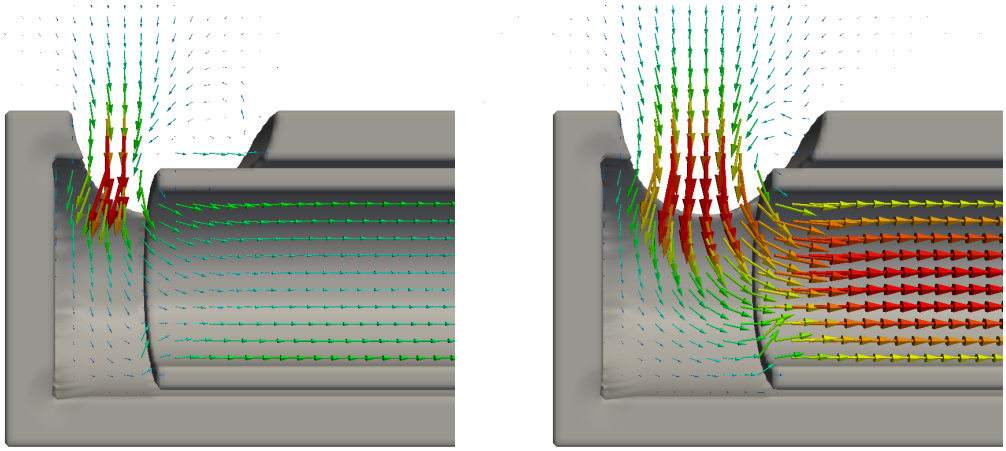

(a) Opening

(b) Opening

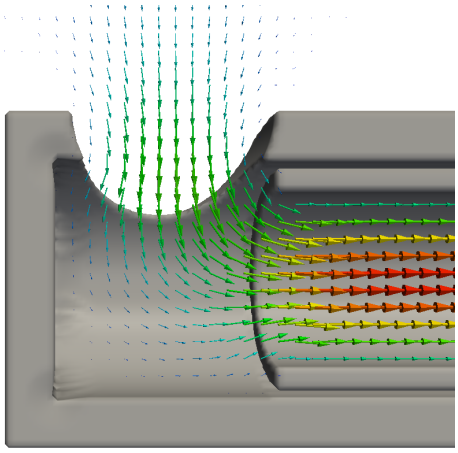

(c) Open

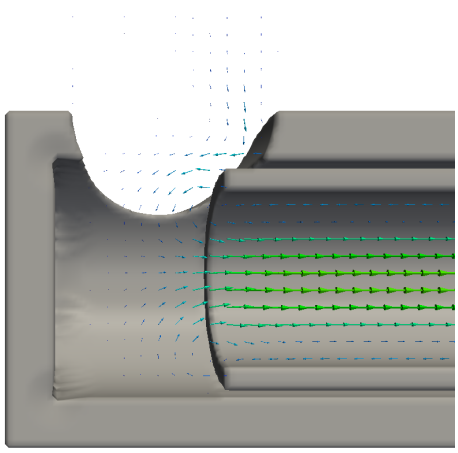

(d) Closing

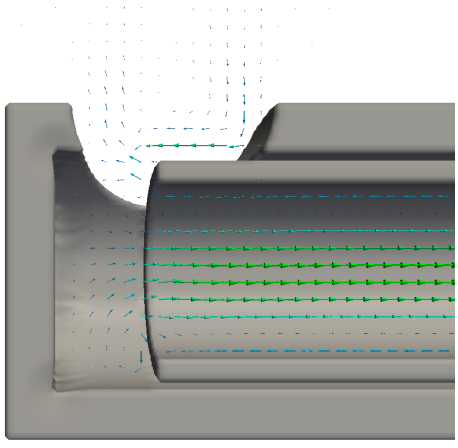

(e) Closing

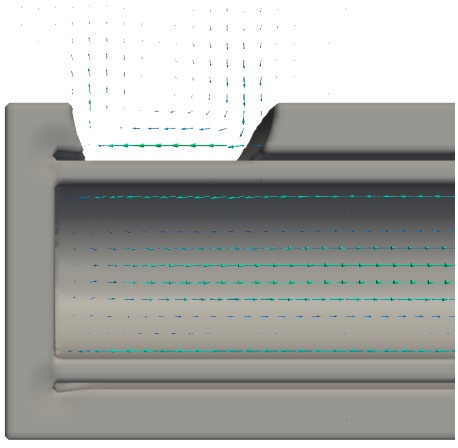

(f) Closed

Figure 3.18: The flow field, colored by overall velocity magnitude, at different stages in the cycle of a 20-gauge cutter operating at 1500 CPM.

To reiterate, the opening and closing events are modeled according to the measurements presented in Table 3.4. Integrating the flow across the circular cross section defined by the inner wall of the guillotine, it is possible to obtain the flow rate as a function of time, shown in Figure 3.19.

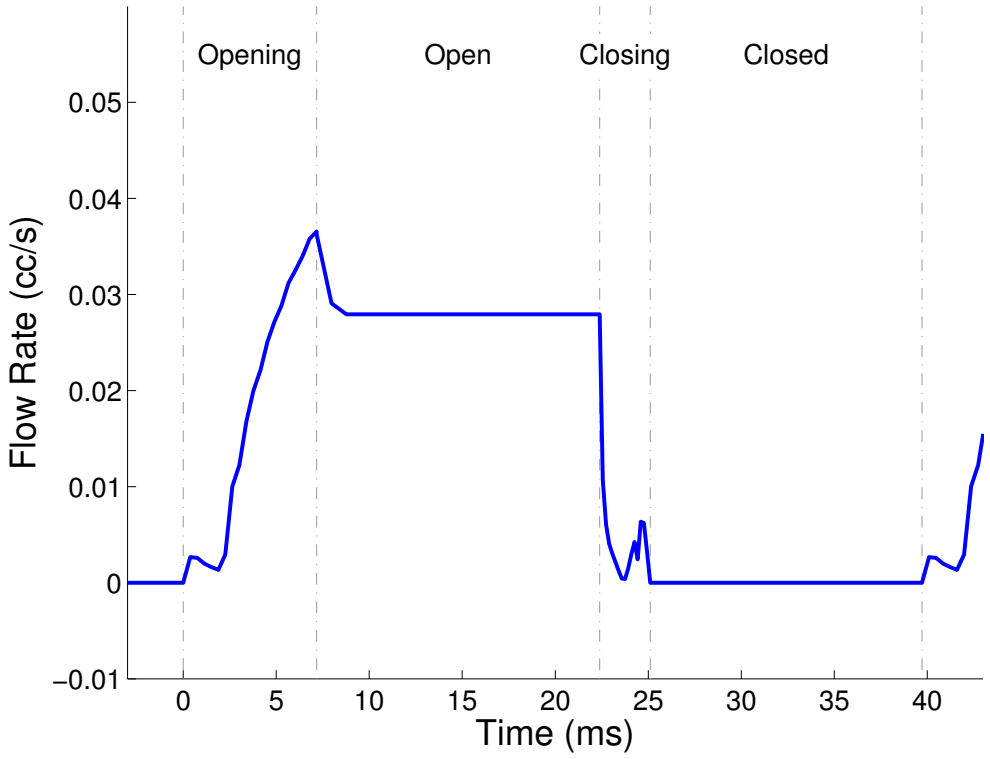

Figure 3.19: The dimensional flow rate inside a 20-gauge cutter operating at 1500 CPM.

For the sake of clarity, Figure 3.19 has been divided up into four stages: opening, open, closing, and closed. Studying this plot alongside Figure 3.18 clearly shows the vitreous' response to guillotine motion over one cutting cycle. As the guillotine moves away from the stationary outer wall, it draws with it a cylindrical core of vitreous, accelerating the chopped substance through the tube and out of the eye. During this period, moving

the guillotine with the direction of traction results in a sharp increase in the flow rate. Once the cutter reaches the fully open position, the motion of the guillotine wall stops, which decelerates the fluid core and decreases the flow rate to a steady state. After this fully-open period is finished, the guillotine begins moving against the direction of traction toward the stationary outer wall. This moves the core of fluid toward the end of the device, fighting the effect of suction forces, resulting in a pronounced decrease in flow rate. Finally, as the guillotine makes contact with the stationary outer wall, the flow rate drops to zero, where it remains until the next cutting cycle begins.

A similar study was performed for the same 20-gauge cutter operating at 2500 CPM. The critical difference to note between these two operational modes is in the amount of time the cutter remains in the fully-open position, as shown in Table 3.4. At 1500 CPM, the cutter spends 15.2 ms in the open position, but at 2500 CPM, the cutter spends only 0.4 ms in the open position. The other durations (opening, closing, closed) remain very similar across both cut rates. This results in a greatly reduced duty cycle, or the ratio of the time the cutter spends in the fully open state to the total cycle time: from 50.8% to 22.5%. Additionally, Sharif-Kashani et al. report slightly different values for the rheological properties of vitreous processed at 2500 CPM. These are printed in Table 3.6.

The vitreous processed at 2500 CPM shows slightly larger time scales than the vitreous processed at 2000 CPM. After accounting for this change, the simulation was repeated to determine the difference between operating at 1500 and 2500 CPM. The flow field

Table 3.6: The physical properties of vitreous chopped at 2500 CPM.

Vitreous Parameter	Value
Density (ρ)	1038 kg/m^3
Total Viscosity (η_0)	0.07 Pa·s
Relaxation Time (λ_1)	5.69 s
Retardation Time (λ_2)	0.22 s
Mobility Factor (α)	0.02 Pa·s

at different stages in the cutting cycle of a 20-gauge vitreous cutter operating at 2500 CPM is shown in Figure 3.20.

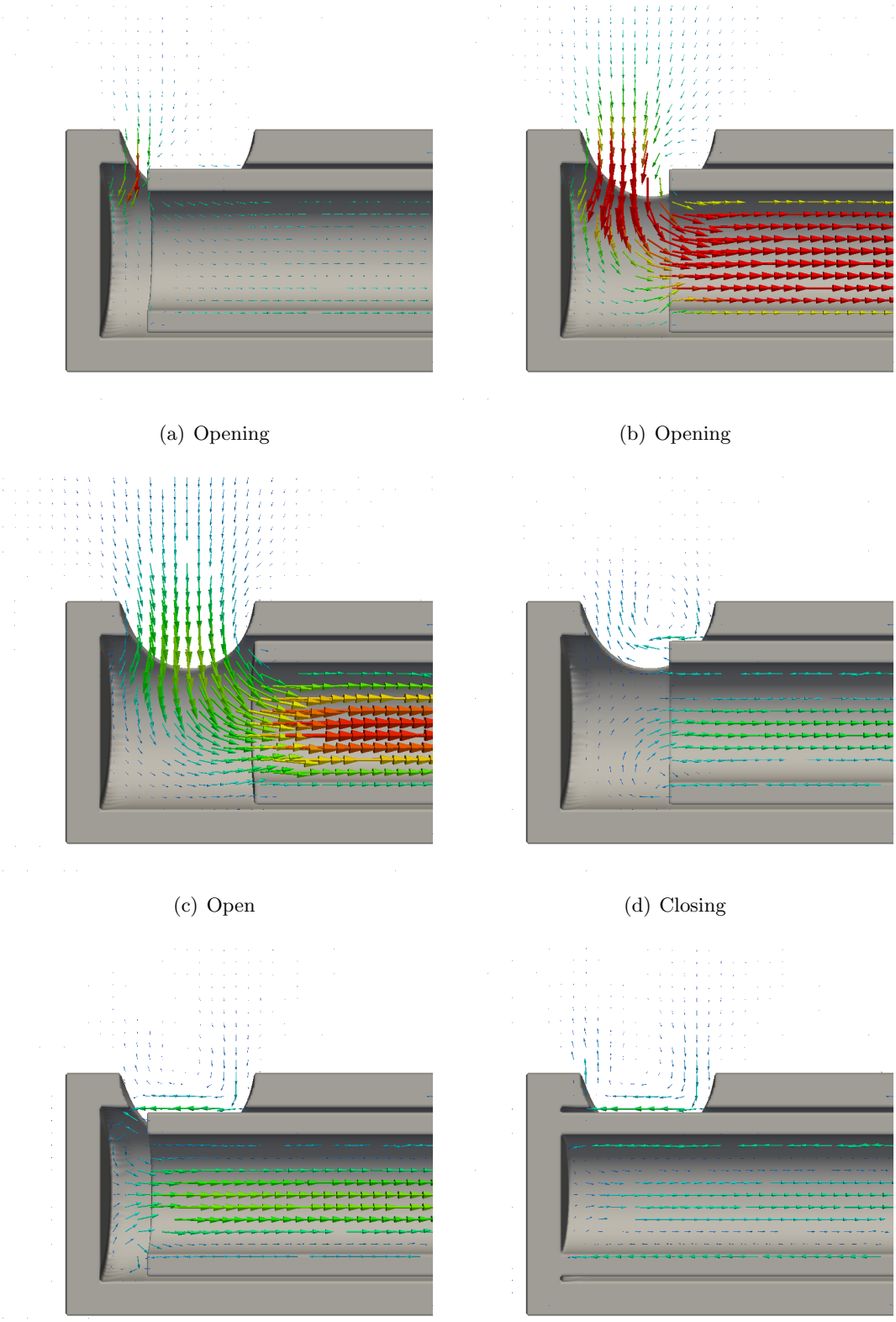

(a) Opening

(b) Opening

(c) Open

(d) Closing

(e) Closing

(f) Closed

Figure 3.20: The flow field, colored by overall velocity magnitude, at different stages in the cycle of a 20-gauge cutter operating at 2500 CPM.

As before, the flow fields in Figure 3.20 are best explained in the context of the time-varying flow rate, shown in Figure 3.21.

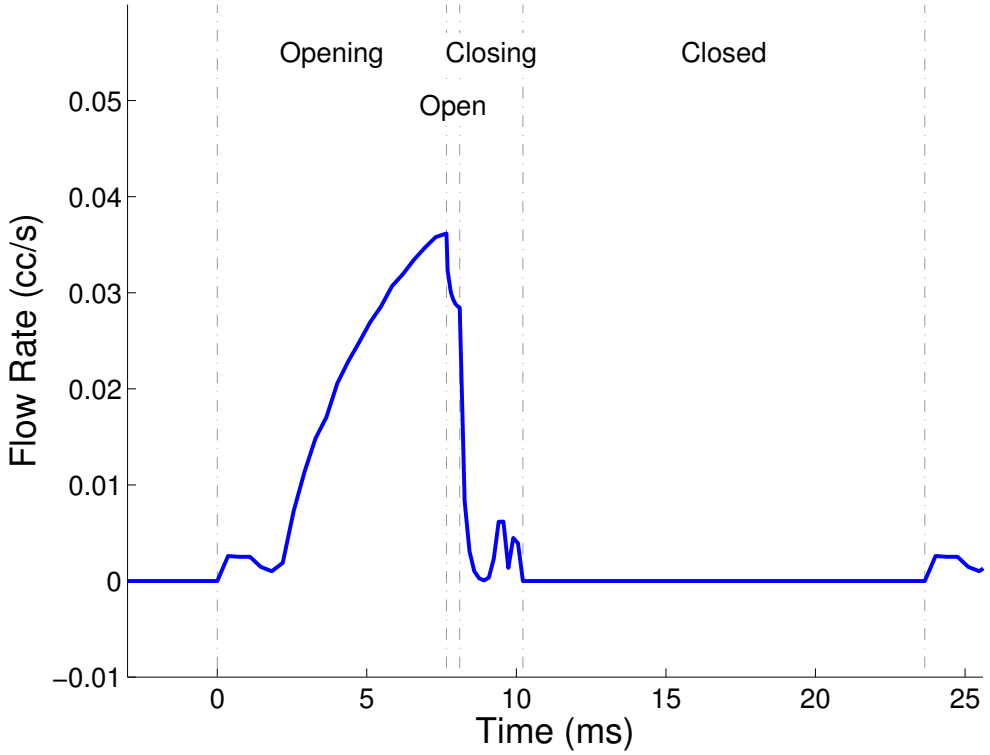

Figure 3.21: The dimensional flow rate inside a 20-gauge cutter operating at 2500 CPM.

The general shape of the plot in Figure 3.21 is similar to that of the case of the cutter operating at 1500 CPM. There is a pronounced increase and decrease in flow rate associated with the opening and closing, respectively, of the guillotine. The critical difference is that the guillotine spends only a small fraction of its total cycle time in the open position, not long enough to reach a steady flow rate, before it begins closing again. This leads to a much lower average flow rate for the total cycle when compared to a 1500 CPM procedure. The average flow rates from both studies are shown alongside

the experimental results of Hubschman et al. in Table 3.7.

Table 3.7: Comparing the average flow rates to experimental results from Hubschman et al. [18].

	20-Gauge Flow Rate (cc/s)	
Source	1,500 CPM	2,500 CPM
Hubschman, 2009	0.0248	0.0013
Computational	0.0172	0.0065

The magnitudes of the computational results show a generally good agreement with the experimental results. The flow rate decreases with increasing cut rate, which is largely the result of a much smaller duty cycle. This trend of reduced average flow rates for increased cut rates has been seen both experimentally and in previous computation studies [18, 23].

3.3.2 Stress

Until this point in the document, the results have been characterized by examining the average and time-varying flow rate through the device. Although a high flow rate through the cutter is desirable, it must be balanced with the importance of avoiding far-reaching stresses that could damage the delicate cells of the retina. When considering a metric for this potential cell damage, the first approach was to look at the pressure gradients near the tip of the cutter. As an example, the pressure fields around a small section of the cutting tip (determined to be the area of the most damaging effects) are

presented in Figure 3.22.

The pressure field snapshots seem to give a feel for how the vitreous reacts to cutting; however, the viscoelastic solver gives access to even more information about the stresses in the fluid. In fact, the Giesekus implementation allows access to all of the individual stress components in the total stress tensor at every point in the fluid. To visualize which of these has the most potential for cell damage, the maximum principal stress is a valuable comparison metric. The principal stress represents the total stress state at a point in the fluid in such an orientation that the shear or off-diagonal components vanish, leaving only three normal components. The maximum of these is chosen to gauge what the most destructive force at the point would be. The principal stress field is compared to the pressure field representation in Figure 3.23.

The maximum principal stress seems to be more illustrative of the conditions directly affecting the vitreous, and for this reason, it was chosen as the metric for cell damage. Although only qualitative at this point, the "bubble" of maximum principal stress that forms near the cutting port, and evolves with the guillotine during cutting, is the primary focus of these images. When designing a vitrectomy system, care must be paid to minimize the appearance of far-reaching stress-affected areas. To begin more meaningful quantitative comparisons, it is appropriate to begin introducing the results for a 23-gauge cutter The flow field and corresponding maximum principal stress contours for a 23-gauge cutter operating at 2500 CPM are shown in Figure 3.24.

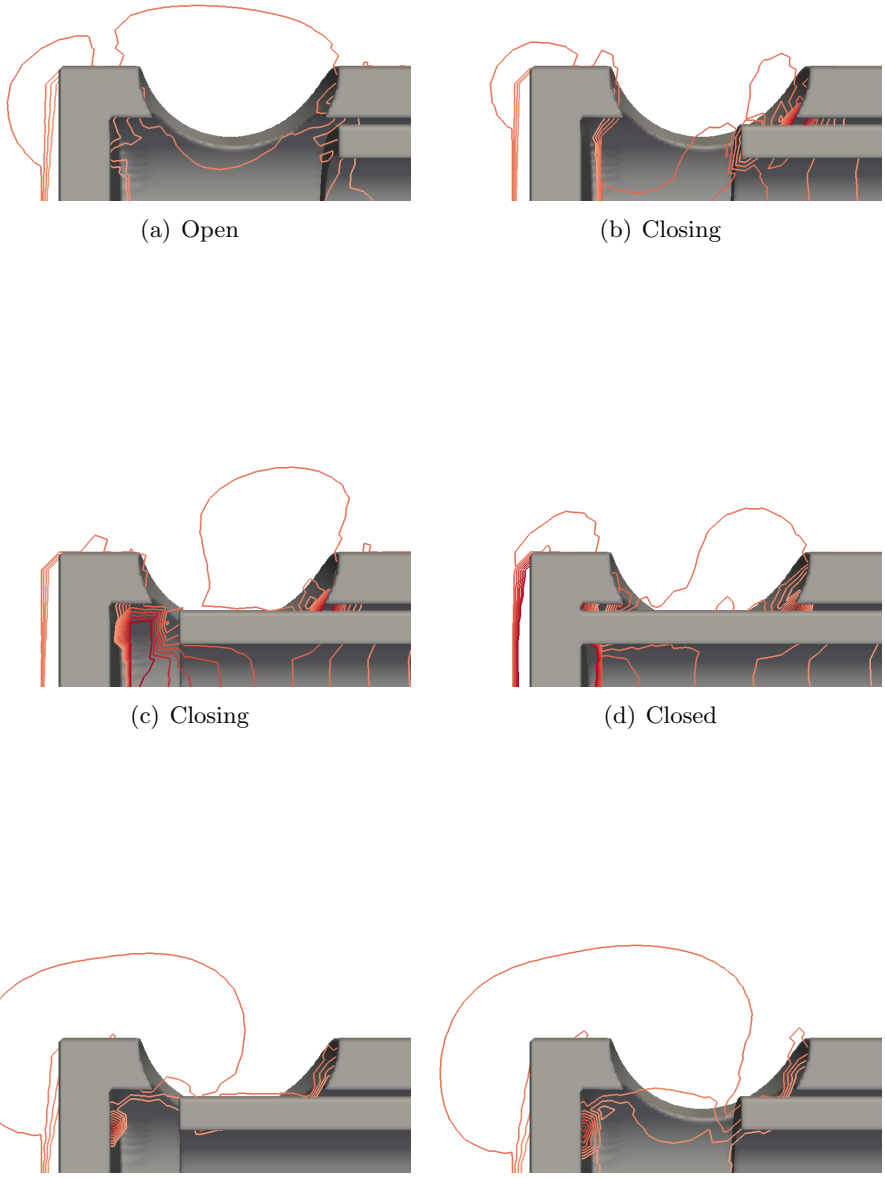

(a) Open (b) Closing

(c) Closing (d) Closed

(e) Opening (f) Opening

Figure 3.22: The pressure field at different stages in the cycle of a 20-gauge cutter operating at 1500 CPM.

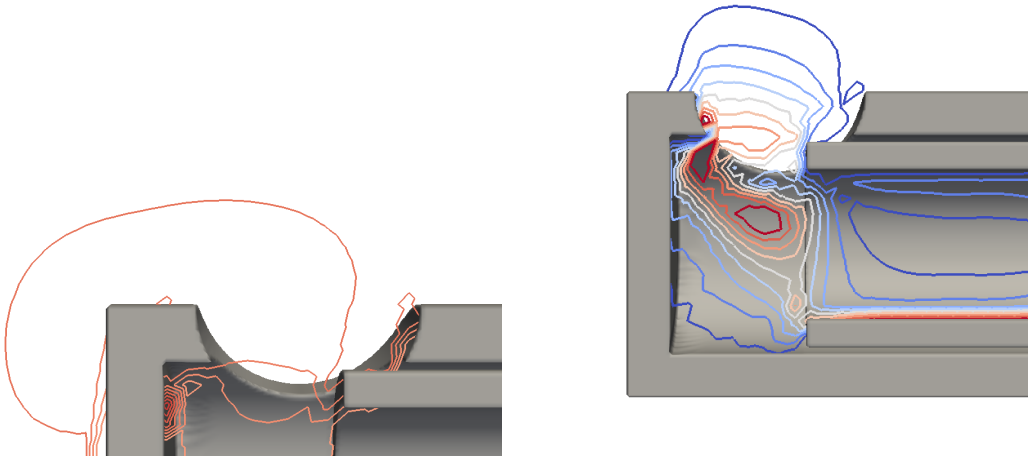

(a) Pressure (b) Maximum Principal Stress

Figure 3.23: Comparing two possible metrics for cell damage: pressure and maximum principal stress, 20-gauge cutter operating at 1500 CPM.

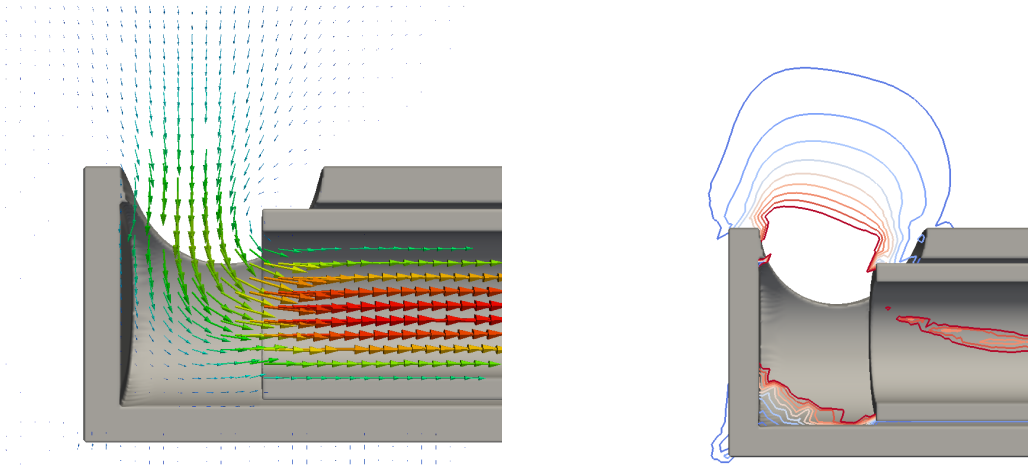

(a) Velocity (b) Maximum Principal Stress

Figure 3.24: The flow field and maximum principal stress contour during the opening phase of a 23-gauge cutter operating at 2500 CPM.

Clearly, the flow field exhibits many of the same behaviors seen in a 20-gauge cutter during the opening phase. To better compare the relative size of the stress-affected area near the cutting port, the maximum principal stress field is shown at the same instant of operation for both a 20- and 23-gauge cutter operating at 1500 and 2500 CPM in Figure 3.25.

Figure 3.25 shows four different cases taken at the same instant in the opening cycle. Identical iso-contours of the maximum principal stress have been drawn for all four cases, allowing comparisons to be made.

There are very evident differences in the way the size of the cutters (along with the manufacturer's recommended vacuum pressure) and the cut rate affect the location and spread of the stress-affected area. Since the primary objective of this study is to balance a high flow rate with minimal disturbance to the surrounding fluid, the large "bubble" of maximum principal stress near the cutting port must be considered. Specifically, to what degree the stresses in the fluid are contained inside the cutting port or body of the vitreous cutter itself.

It is worth noting that the cross sections in Figure 3.25 have been scaled so that the cutters (and, in turn, their stress-affected areas) appear at the correct size relative to one another. In other words, the 23-gauge cutter has been shown proportionally smaller than the 20-gauge cutter. A cursory analysis suggests that the 23-gauge cutters have a slightly farther-reaching stress-affected area *relative to the size of the instrument.*

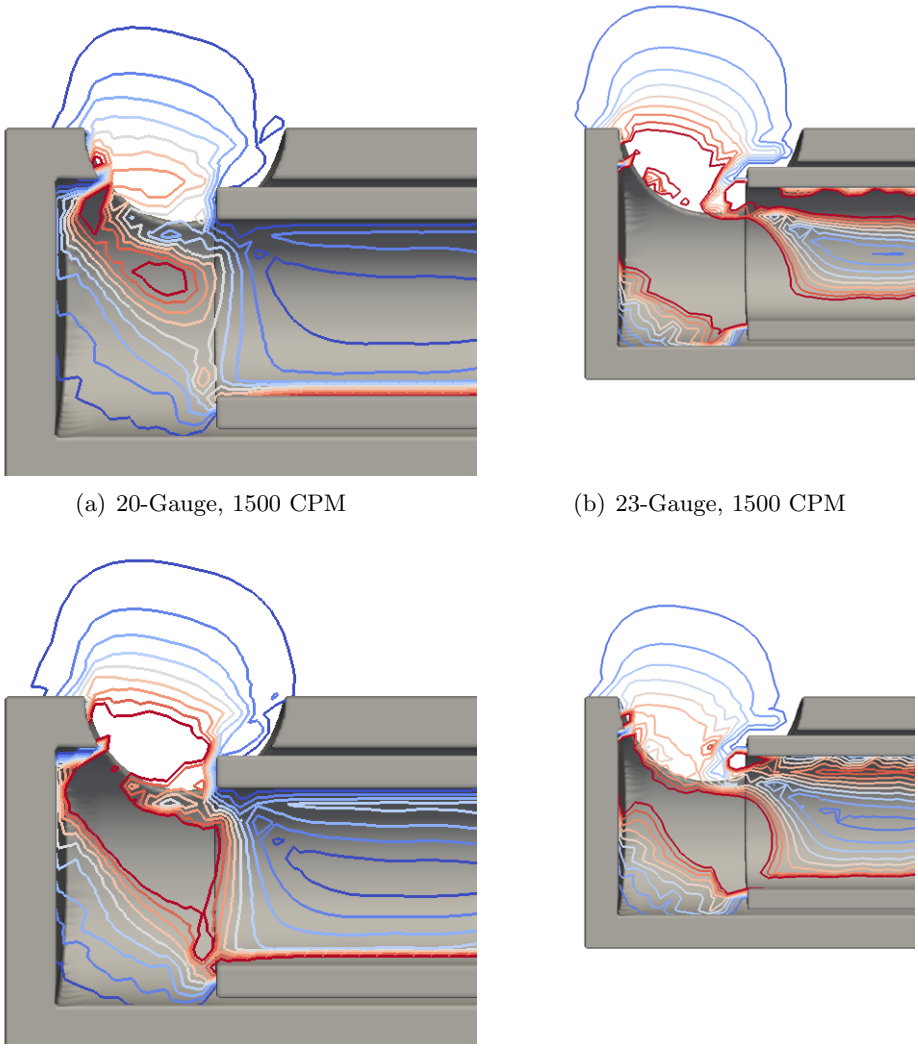

(a) 20-Gauge, 1500 CPM

(b) 23-Gauge, 1500 CPM

(c) 20-Gauge, 2500 CPM

(d) 23-Gauge, 2500 CPM

Figure 3.25: The maximum principal stress fields at the same instant of opening for four different cases.

In addition to the size of the stress-affected area, the location of the highest stresses, whether it is contained inside or propagates outside of the cutter, can be observed. Certainly, increasing the vacuum pressure at the surgeon's console form 250 to 550 mmHg in the case of the 23-gauge cutter plays a role. More will be said about these effects, and what can be concluded, in Section 4.1.

Beginning with the left-hand column of Figure 3.25 depicting the 20-gauge cutters, it seems that the size of the stress-affected area grows when increasing the cut rate from 1500 to 2500 CPM. Additionally, the location of the highest stresses (in red) begins to move further outside the cutter body, through the cutting port, for the case of 2500 CPM. This is contrary to the behavior seen in the right-hand column, depicting the 23-gauge cutters. For this geometry, it seems that the 1500 CPM case generates farther reaching stresses than the 2500 CPM case. Additionally, the 1500 CPM case has higher stresses migrating away from the cutter body, while the 2500 CPM case does a better job of containing the highest stresses inside the cutter body.

It seems that a relationship between cutting rate and cell damage cannot be constructed; however, when examining the *velocity* of the guillotine for each of these cases, a clearer picture begins to emerge. The velocity of the guillotine associated with the opening action for the four cases in question is shown in Table 3.8.

In both cases, the two best-performing scenarios are associated with a relatively higher opening guillotine velocity. For the 20-gauge cutter, increasing the cutting rate *decreases*

Table 3.8: The opening speeds of the guillotine for four different cases.

CPM	Opening Velocity (cm/s)
20-Gauge	
1,500	7.9
2,500	7.4
23-Gauge	
1,500	9.4
2,500	9.6

the opening velocity, which is associated with an increase in the stress-affected area. The 23-gauge cutter shows the opposite behavior, with a guillotine velocity that *increases* at the higher cutting rate. More will be said about this potential connection in Section 4.1.

The stresses generated during the closing event are also of interest. The maximum principal stress field is shown at the same instant of closing for both a 20- and 23-gauge cutter operating at 1500 and 2500 CPM in Figure 3.26.

Starting with the left-hand column of Figure 3.26 depicting the 20-gauge cutter, it seems that increasing the cutting rate from 1500 to 2500 CPM is associated with a slight increase in the size of the stress-affected area. There is, perhaps, a small shifting of the location of the highest stresses further into the vitreous body, but it is not as pronounced as in the opening case. In the right-hand column, the 23-gauge cutters

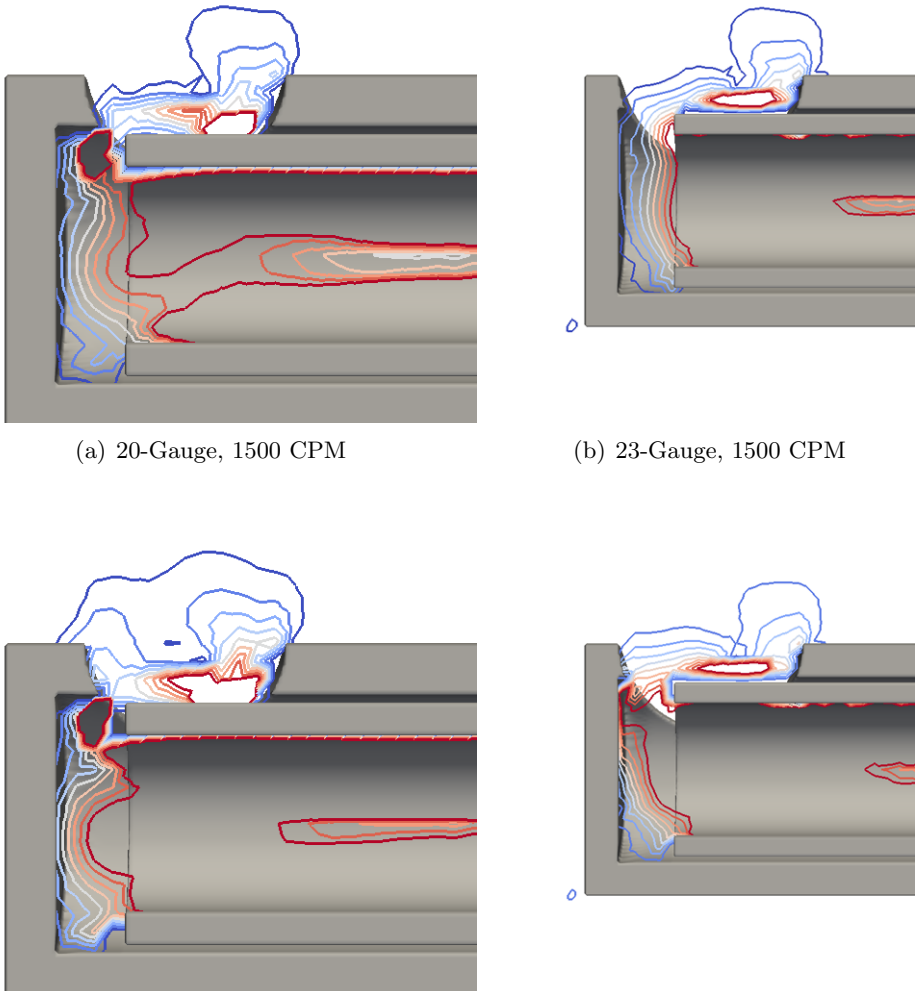

(a) 20-Gauge, 1500 CPM

(b) 23-Gauge, 1500 CPM

(c) 20-Gauge, 2500 CPM

(d) 23-Gauge, 2500 CPM

Figure 3.26: The maximum principal stress fields at the same instant of closing for four different cases.

Table 3.9: The closing speeds of the guillotine for four different cases.

CPM	Closing Velocity (cm/s)
20-Gauge	
1,500	21.1
2,500	27.1
23-Gauge	
1,500	25.5
2,500	20.0

show only very small changes between operating at 1500 and 2500 CPM. The size of the stress-affected area remains relatively constant, and the region of highest stress shows only slight differences. As before, the closing velocities generating these stresses are shown in Table 3.9.

In contrast to the opening cases, there is no clear link between closing velocity and the size and/or location of the stress-affected area. The 20-gauge cutter closes faster at higher cut rates, and the 23-gauge cutter closes faster at lower cut rates. This does not seem to indicate a trend of either shrinking or growing the stress-affected area. The importance of studying the features associated with guillotine closing will be addressed further in Section 4.1.

Despite the seeming lack of correlation between the stress-affected area and closing velocity, there is clearly a difference when considering the general behaviors seen between

a cutter during opening and during closing. For the ease of comparison, a representative sample illustrating this distinction is shown below in Figure 3.27.

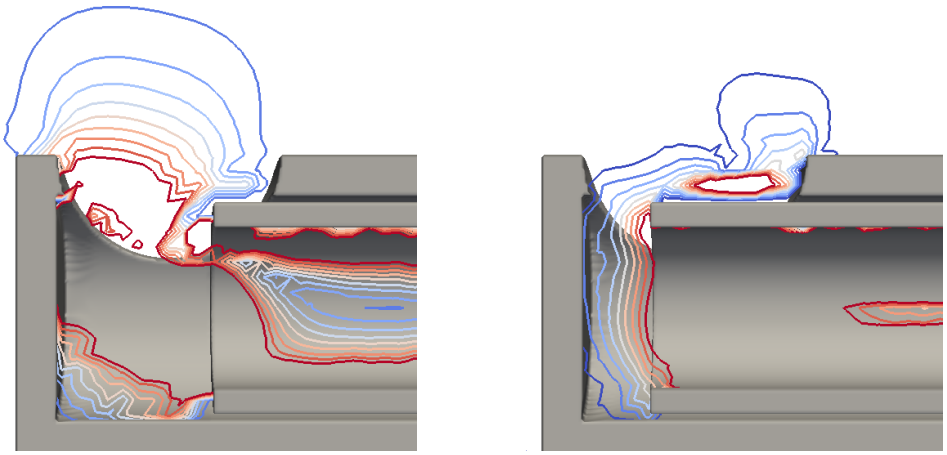

(a) Opening (b) Closing

Figure 3.27: Characteristic samples of the maximum principal stress fields for a 23-gauge cutter operating at 1500 CPM.

Clearly, the opening stage is more potentially destructive to retinal cells than the closing stage using the maximum principal stress as the metric for cell damage. Not only does the stress-affected area extend further into the vitreous during opening than closing, but the location of the highest stresses begins to propagate further outside the body of the cutter during opening than closing. This is true for both the cutters examined in this study and both the cut rates considered. Moving forward, the opening phase of the cutter should be considered as a target for improvement. Pneumatically actuated cutters seem to vary their cut rate primarily by changing the amount of time the guillotine spends in the fully open position. Unfortunately, this leads to a much lower duty cycle at high cut rates, and reduced flow through the device. Manipulating the opening speed

of the guillotine could help increase duty cycle at high cut rates, while also leading to better management of the stress-affected area near the cutting port.

3.3.3 Novel Cutter Design

Until this point, the focus has been exclusively on commercially available cutter designs. These were simulated using the best measurements of geometry and cutting dynamics available, and implemented alongside the manufacturer's recommended operating conditions. However, one of the strengths of approaching this problem computationally is the ease with which new designs can be synthesized and tested. To this end, a preliminary simulation was conducted on the geometry shown in Figure 3.28.

This geometry is identical to the 20-gauge cutter from previous cases, but includes an arbitrarily chosen rectangular keyhole. This additional port was trivial to add with the constructive solid geometry approach to generating signed distance fields: simply subtract an extra rectangular solid from the usual guillotine-creation step. Functionally, it produces a design that operates at what is essentially 100% duty cycle, as there is always some opening through which fluid can be aspirated. Additionally, it is hypothesized that the additional cutting surface could have a positive effect on the level of fragmentation. The preliminary results for this cutter are shown in Figure 3.29.

These results are not presented in support of either the 100%-duty-cycle or increased-fragmentation hypotheses. Rather, they are included here only to demonstrate the

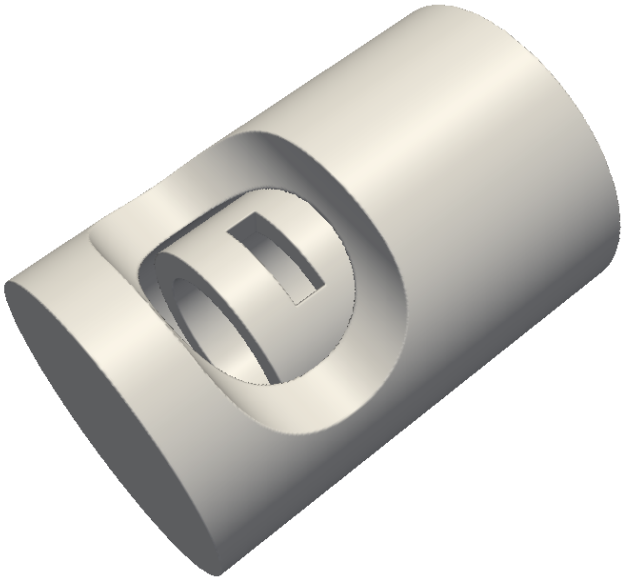

Figure 3.28: The inclusion of a rectangular "keyhole" in the standard guillotine geometry.

benefits of approaching this problem computationally, and the ease with which these types of ideas can be incorporated and tested. More research is needed to characterize the impact of such design changes, and will be discussed in the following section.

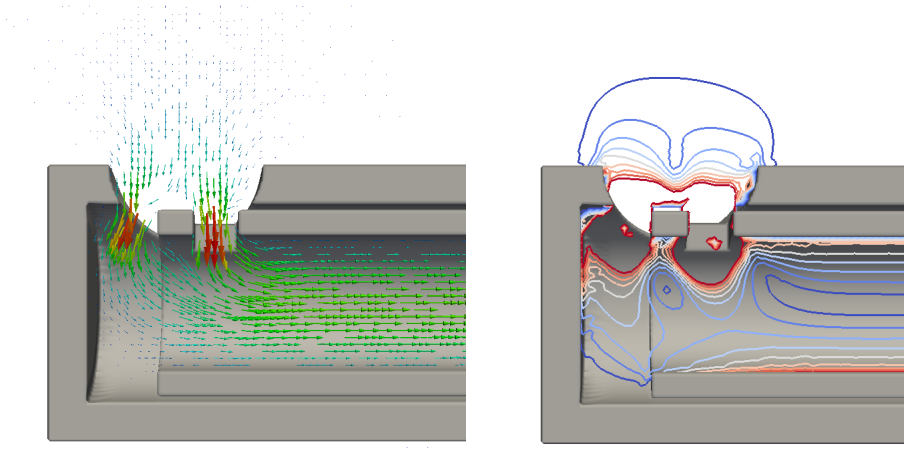

(a) Velocity (b) Maximum Principal Stress

Figure 3.29: A very preliminary result of a rectangular-keyhole cutter in the opening stage, highlighting the potential of the tool presented in this document for quickly testing new designs.

Chapter 4

Concluding Remarks

4.1 Discussion

As stated in Section 1.4, the goal of this study is to model the complicated flow though an operational vitreous cutter. This has the potential to offer recommendations on the optimal instrumentation for vitrectomy and to provide operational guidelines to surgeons. Multiple relevant studies have been presented toward fulfilling these objectives. A three-dimensional computational model of a vitreous cutter has been created and can be easily modified by changing a small number of parameters. The constructive solid geometry based on the most basic measurements of a vitreous cutter works well, and is easily changed to test the effect of different dimensions. The complicated, moving boundary is accounted for using a "sharp" interface immersed boundary method. Flow

through this immersed boundary is driven by the traction boundary condition, allowing natural entrainment and domain truncation. All these features have been verified on multiple benchmark problems. At its core, all these simulations are heavily influenced by the semi-implicit implementation of the Giesekus constitutive equation. The Giesekus model is capable of reproducing the experimentally observed behavior of vitreous, while the semi-implicit implementation allows for the simulation of long relaxation times without instability.

The Newtonian simulations presented in Section 3.2 were a good first step toward characterizing the flow in a vitreous cutter. Although these results did not account for the viscoelastic nature of the vitreous, elements of the flow field, and their effects on the flow rate through the device, are consistent with previous computational studies [23, 24]. It was shown that for a Newtonian fluid, the largest average flow rate is achieved by operating the vitreous cutter at 100% duty cycle. In this way, the vitreous cutter doesn't cut at all, but operates as a simple syringe through which the vitreous can be aspirated. This result is of limited application, however, since it is known that simply aspirating intact, viscoelastic vitreous without fragmentation is not effective. Thus, the study turned to the viscoelastic simulations of vitrectomy.

Accounting for the viscoelastic nature of the vitreous allowed the study to offer real insights about what happens during vitrectomy. As in the Newtonian case, it was shown that flow features associated with the opening and closing of the guillotine have a large effect on the flow rate through the device. As the guillotine wall moves with the

direction of traction, a core of fluid is accelerated out of the device, resulting in a large increase in flow rate. When the guillotine begins closing, the core of fluid surrounded by the guillotine wall is accelerated against the direction of the flow, toward the stationary outer wall, resulting in a sharp decrease in the flow rate. The time averaged flow rate for multiple cut rates was compared to experimental results from Hubschman et al. [18]. The viscoelastic simulations capture the correct trend for all cases. At higher cut rates, the flow rate decreases, which seems to be mostly attributable to a much smaller duty cycle (the ratio of the time the cutter spends in the open position to the total cycle time). Due to the nature of the pneumatically-actuated cutters considered in this experiment, the difference between cut rates is mostly accounted for by differences in the amount of time spent in the fully open state. Experimental results from Magalhaes et al. suggest that this trend is highly dependent on the exact cutting dynamics; specifically, that because of the differences between electric and the more traditional pneumatic actuation techniques, higher cut rates do not necessarily mean lower flow rates [37, 38].

Furthermore, the time averaged flow rates exhibit the same order of magnitude as the experimental results. It is perhaps not surprising that a perfect agreement is not obtained, given the assumptions and measurement errors inherent to every method and constant described in this document. Still, the generally good agreement suggests that the model is working as expected, and that the assumptions and simplifications described for these studies do not significantly degrade the results. One of the most important of these assumptions is the choice to model the entire computational domain with the rheological

properties of chopped vitreous. This choice was made so that accurate values for flow rate could be obtained. The generally good agreement with the experimental results suggests that this assumption had the intended effect. A more physics-driven approach to the problem of chopped versus un-chopped rheology is addressed in Section 4.2.

The flow rate is certainly an important metric in classifying cutter behavior, but it must be balanced with the importance of minimizing the appearance of far-reaching stresses that could potentially damage the delicate cells of the retina on the posterior surface of the eye cavity. The Giesekus implementation allows direct access to all the information about the stress terms in the fluid, which offers many possible options for a cell-damage metric. Values for the pressure field are presented, as are results highlighting the maximum principal stress in the fluid, a quantity derived post-processing which represents the most influential normal stress at a given location. The principal stress is a helpful quantity, because it combines the effects of all the individual stress components into a single stress state oriented such that the shear components vanish.

Using the maximum principal stress as the primary metric for cell damage, it is possible to compare the different cutting rates and cutter sizes directly to one another. As the cutters are opening and closing, a stress-affected region is created in the vicinity of the cutting port. The location and spread of this region depends on the size of the aperture, speed of the guillotine, and the vacuum pressure at the outlet. In all the cases presented in this document, the opening phase is consistently the most destructive point in the overall cutting cycle. This is evidenced both by an increase in the distance that

the stress-affected area extends into the vitreous, as well as a migration of the highest stresses from being contained inside the body of the cutter to extending out through the cutting port.

Considering only the opening phase, it was shown that a higher opening velocity of the guillotine is associated with a reduction in the size and spread of the stress-affected area. For a 20-gauge cutter operating at 1500 CPM and a 23-gauge cutter operating at 2500 CPM, the highest stresses were localized entirely inside the cutter body and the stress "bubble" created around the cutting port was reduced when the velocity of the guillotine was increased. This trend was not immediately evident when looking only at the cut rate, as a 20-gauge cutter opens faster at 1500 CPM than 2500 CPM, while a 23-gauge cutter opens faster at 2500 CPM than 1500 CPM. This is likely because of the exact pneumatic mechanism used in these cutters.

No such trend was found in the closing of the guillotine, despite considering links between cutting rates, closing speeds, and other factors that could potentially provide insight. However, it is worth reiterating that since the opening phase was consistently found to have the most potential for retinal cell damage, the response of the vitreous during closing can be considered less of a focus in optimization.

Considered in total, these simulations have shown the importance of maximizing duty cycle at high cut rates to avoid negatively impacting the flow rate through the cutter, while also suggesting a way to minimize the creation of stresses inside the eye. Tradi-

tionally actuated cutters increase cut speed almost entirely by adjusting the amount of time spent in the fully open position, but this is not necessarily the best strategy. There seems to be a connection between the opening speed of the guillotine and a reduction in the stress-affected area. By opening the cutter more quickly, an optimized design can not only minimize the appearance of far-reaching stresses, but also increase its duty cycle, and thus, its flow rate. Because of the many factors that changed between the studies performed on 20- and 23-gauge cutters, more testing is needed to have complete confidence in these design guidelines.

As previously discussed, it seems that a faster opening speed is desirable to minimize the appearance of far-reaching stresses; however, if this leads to reducing the amount of fragmentation, it has the potential to objectionably reduce the flow rate. Since these studies assume all the vitreous has a chopped consistency, this trade off is not modeled correctly. Further study, potentially with the spatially-varying rheology previously described, has the potential to better solidify understanding of the relationship between stress, flow rate, and surgical variables.

4.2 Future Work

Although many of the objectives set forth in Section 1.4 have been achieved, there is still room to extend these viscoelastic models to create a fuller picture of the physics of vitrectomy.

One of the most important assumptions presented in this document was the choice to model the entire computation domain, both inside and outside the cutter, with the rheological properties of chopped vitreous. During an actual vitrectomy, the highly elastic intact vitreous is drawn in through the cutting port where it is eventually severed from the bulk by the chopping action of the guillotine. This transition to the chopped consistency results in a substance that behaves more like a liquid, and can be smoothly aspirated from the eye. In order to fully account for this spatially-varying rheology, it would be necessary to introduce some sort of tracking algorithm to mark and follow the evolving interface between chopped and un-chopped regions. This tracking routine would inform the solver as to which nodes should be treated with the rheological properties corresponding to the highly elastic un-chopped vitreous, with its long time scales, and which nodes should be assigned the rheological properties of the liquid-like chopped vitreous, which exhibits much shorter time scales as well as a small degree of shear thinning.

Where to make this distinction is still something of an open question. Certainly once the guillotine has stopped its cutting motion, everything in the tube should be considered

chopped. How to treat the vitreous as it's being chopped (while the guillotine is closing) is less straightforward. The simplest, although arguably ad hoc, solution may be to consider that the front between chopped and un-chopped moves directly along with a vertical line defined by the edge of the guillotine. Numerically speaking, dealing with this very sharp interface between regions with two vastly different time scales will likely require some care to avoid instability. A "transition" zone may be necessary, in which the vitreous moves smoothly from the intact state to the chopped state. This is likely the most physically accurate, since the vitreous near the cutter likely doesn't experience a sudden "jump" in rheology, but rather undergoes a smooth transition to more liquid-like behavior. Again, the choice of how to define such a region is not clear at this time.

The impedance-matching addition to the traction boundary condition is not as robust as hoped. In certain situations, the feedback loop connecting the instantaneous flow rate and the vacuum pressure is extremely slow to converge, sometimes not converging at all. Despite many efforts in this area, it still has the potential to cause problems for simulations. Isolating this feature with an appropriate test case would help determine the root of the problem, which would help future simulations move more smoothly.

There are still some geometric features of the vitreous cutter geometry based on best assumptions and/or convenience. For example, the resting position of the cutter in the open state is not viewable in the high-speed film of Hubschman et al. [18]. Because this location determines the span the cutter must eventually travel, it in turn affects

the calculation of the guillotine velocity, which was shown to be very important for both flow rate and potential cell damage. It would be beneficial to replace these values with their real-world counterparts, in an effort to make future studies as immediately clinically relevant as possible. With such a model, an in-depth parameter study would be more directly helpful. Results like those presented in this document are certainly valuable, but don't reveal much toward optimizing the current instrumentation if there are fundamental misrepresentations of the basic geometry and dynamics. Once these potential sources of error are eliminated or reduced, the effects of aspiration pressure, cut rate, and duty cycle need to be characterized in a systematic way to fully meet all the objectives presented in Section 1.4.

Time-average flow rates remain an important metric in classifying cutter performance, and should continue to be calculated as a function of the cut rate and duty cycle variables. Previous studies have shown the importance of a high duty cycle and cut rate, but indicate that as cut rate continues to rise, the mean flow rate begins dropping due to a lower duty cycle [19, 37]. A particularly interesting point is that this effect differs depending on the actuation mechanism of the cutter: pneumatic versus electric. It would be interesting to obtain cutting durations for electrically-actuated cutters and compare the performance to the pneumatically-actuated cutters presented in this document. Finding an optimal balance of these two parameters, duty cycle and cut rate, based on currently available guillotine technology is certainly a worthwhile effort.

A parameter study performed that accounts for these issues has the potential to eluci-

date even further connections between surgical variables, and will indicate an optimal combination or trend to guide future instrument design and operation guidelines. As previously shown, novel geometries or cutting rates are easily implementable within the framework of the method described here. These findings have the potential to benefit both surgeons and patients with improved outcomes.

Bibliography

[1] Eye anatomy, glaucoma research foundation. http://www.glaucoma.org/glaucoma/anatomy-of-the-eye.php, August 2012.

[2] Manuel A. Alves, Paulo J. Oliveira, and Fernando T. Pinho. Benchmark solutions for the flow of Oldroyd-B and PTT fluids in planar contractions. *Journal of Non-Newtonian Fluid Mechanics*, 110:45–75, December 2003.

[3] R. Aris. *Vectors, Tensors, and the Basic Equations of Fluid Mechanics.* Dover Publications, Inc., 1962.

[4] E. Balaras. Modeling complex boundaries using an external force field on fixed Cartesian grids in large-eddy simulations. *Computers and Fluids*, 33(3):375–404, 2003.

[5] R. B. Bird, R. C. Armstrong, and O. Hassager. *Dynamics of Polymeric Liquids*, volume 1. Wiley-Interscience, 1987.

[6] B. J. Boersma. A numerical investigation on the effect of the inflow conditions on the self-similar region of a round jet. *Physics of Fluids*, 10(4):899–909, 1998.

[7] B. J. Boersma. Entrainment boundary conditions for free shear flows. *International Journal of Computational Fluid Dynamics*, 13(4):357–363, 2000.

[8] C. H. Bruneau and P. Fabrie. Effective downstream boundary conditions for incompressible Navier–Stokes equations. *International Journal for Numerical Methods in Fluids*, 19(8):693–705, 1994.

[9] Henrik Bruus. *Theoretical Microfluidics*. Oxford University Press, USA, 2007.

[10] H. C. Choi, J. H. Song, and J. Y. Yoo. Numerical simulation of the planar contraction flow of a giesekus liquid. *Journal of Non-Newtonian Fluid Mechanics*, 29(1-3):347–379, 1988.

[11] C. Eckardt. Transconjunctival sutureless 23-gauge vitrectomy. *Retina-The Journal of Retinal and Vitreous Diseases*, 25(2):208–211, 2005.

[12] S. F. Frisken and R. N. Perry. Designing with distance fields. In *ACM SIGGRAPH 2006 Courses*, pages 60–66, 2006.

[13] G. Y. Fujii, E. De Juan, M. S. Humayun, D. Pieramici, T. Chang, E. Ng, A. Barnes, S. Wu, and D. Sommerville. A new 25-gauge instrument system for transconjunctival sutureless vitrectomy surgery. *Ophthalmology*, 109(10):1807–1812, 2002.

[14] H. Giesekus. A simple constitutive equation for polymer fluids based on the con-

cept of deformation-dependent tensorial mobility. *Journal of Non-Newtonian Fluid Mechanics*, 11(1-2):69–109, 1982.

[15] P. M. Gresho. Incompressible fluid dynamics: some fundamental formulation issues. *Annual Review of Fluid Mechanics*, 23(1):413–453, 1991.

[16] P. M. Gresho and R. L. Sani. On pressure boundary conditions for the incompressible Navier-Stokes equations. *International Journal for Numerical Methods in Fluids*, 7(10):1111–1145, 1987.

[17] J. P. Hubschman. Comparison of different vitrectomy systems. *Journal Francais D Ophtalmologie*, 28(6):606–609, 2005.

[18] J. P. Hubschman, J. L. Bourges, I. Tsui, S. Reddy, F. Yu, and S. D. Schwartz. Effect of cutting phases on flow rate in 20-, 23-, and 25-gauge vitreous cutters. *Retina-The Journal of Retinal and Vitreous Diseases*, 29(9):1289–1293, 2009.

[19] J. P. Hubschman, A. Gupta, D. H. Bourla, M. Culjat, F. Yu, and S. D. Schwartz. 20-, 23-, and 25-gauge vitreous cutters-performance and characteristics evaluation. *Retina-The Journal of Retinal and Vitreous Diseases*, 28(2):249–257, 2008.

[20] J. Jeong and F. Hussain. On the identification of a vortex. *Journal of Fluid Mechanics*, 285(2):69–94, 1995.

[21] M. Jiang and R. Machiraju. Detection and visualization of vortices. In *The Visualization Handbook*, pages 295–309. Academic Press, 2005.

[22] T. A. Johnson and V. C. Patel. Flow past a sphere up to a Reynolds number of 300. *Journal of Fluid Mechanics*, 378(1):19–70, 1999.

[23] T. Juan. *A computational study of the flow through a vitreous cutter*. PhD thesis, University of California Los Angeles, 2011.

[24] T. Juan, J. P. Hubschman, and J. D. Eldredge. A computational study of the flow through a vitreous cutter. *Journal of Biomechanical Engineering*, 132(12):121005–121013, 2010.

[25] P. K. Kaiser. Advanced vitreous cutter offers duty cycle control. *Retinal Physician*, February 2009.

[26] D. Kasner, G. R. Miller, W. H. Taylor, R. J. Sever, and E. W. Norton. Surgical treatment of amyloidosis of the vitreous. *Transactions of the American Academy of Ophthalmology and Otolaryngology*, 72(3):410–417, 1968.

[27] D. B. Khismatullin and G. A. Truskey. Three-dimensional numerical simulation of receptor-mediated leukocyte adhesion to surfaces: Effects of cell deformability and viscoelasticity. *Physics of Fluids*, 17(3), March 2005.

[28] J. Kim, D. Kim, and H. Choi. An immersed-boundary finite-volume method for simulations of flow in complex geometries. *Journal of Computational Physics*, 171(1):132–150, 2001.

[29] J. Liu. Open and traction boundary conditions for the incompressible Navier-Stokes

equations. *Journal of Computational Physics*, 228(19):7250–7267, 2009.

[30] R. Machemer. Vitrectomy: a pars plana approach. *Transactions of the American Academy of Ophthalmology and Otolaryngology*, 75(4):813–820, 1971.

[31] R. Machemer. New concept for vitreous surgery 7: Two instrument techniques in pars-plana vitrectomy. *Archives of Ophthalmology*, 92(5):407–412, 1974.

[32] R. Machemer. The development of pars plana vitrectomy: a personal account. *Graefe's Archive for Clinical and Experimental Ophthalmology*, 233(8):453–468, August 1995.

[33] E. N. Marieb and K. Hoehn. *Human Anatomy & Physiology*. Pearson Benjamin Cummings, 7 edition, 2007.

[34] R. Mittal. A Fourier-Chebyshev spectral collocation method for simulating flow past spheres and spheroids. *International Journal for Numerical Methods in Fluids*, 30(7):921–937, 1999.

[35] R. Mittal, H. Dong, M. Bozkurttas, F. M. Najjar, A. Vargas, and A. von Loebbecke. A versatile sharp interface immersed boundary method for incompressible flows with complex boundaries. *Journal of Computational Physics*, 227(10):4825–4852, 2008.

[36] R. Mittal and G. Iaccarino. Immersed boundary methods. *Annual Review of Fluid Mechanics*, 37(1):239–261, 2005.

[37] Jr. O. Magalhaes, L. Chong, C. Deboer, P. Bhadri, R. Kerns, A. Barnes, S. Fang, and M. Humayun. Vitreous dynamics-vitreous flow analysis in 20-, 23-, and 25-gauge cutters. *Retina-The Journal of Retinal and Vitreous Diseases*, 28(2):236–241, 2008.

[38] Jr. O. Magalhaes, M. Maia, E. B. Rodrigues, L. Machado, E. F. Costa, A. Maia, M. N. Moares-Filho, E. Dib, and M. E. Farah. Perspective on fluid and solid dynamics in different pars plana vitrectomy systems. *American Journal of Ophthalmology*, 151(3):401—405.e1, 2011.

[39] C. O'Malley and R. M. Heintz. Vitrectomy with an alternative instrument system. *Annals of Ophthalmology*, 7:585–588, 591–594, 1975.

[40] S. Osher and R. Fedkiw. *Level Set Methods and Dynamic Implicit Surfaces*. Springer, 2003.

[41] A. Palmer. *Linear Stability Analyses of Poiseuille Flows of Viscoelastic Liquids*. PhD thesis, The University of Wales, 2007.

[42] C. S. Peskin. Flow patterns around heart valves: A numerical method. *Journal of computational physics*, 10(2):252–271, 1972.

[43] A. Poux, S. Glockner, and M. Azaiez. Improvements on open and traction boundary conditions for Navier-Stokes time-splitting methods. *Journal of Computational Physics*, 230(10):4011—4027, 2011.

[44] A. Raisi, M. Mirzazadeh, A. S. Dehnavi, and F. Rashidi. An approximate solution for the Couette-Poiseuille flow of the Giesekus model between parallel plates. *Rheologica Acta*, 47(1):75–80, 2008.

[45] S. Rizzo and F. Barca. Twenty-seven-gauge sutureless microincision vitrectomy surgery: a new frontier? *Retina-The Journal of Retinal and Vitreous Diseases*, pages 37–40, April 2013.

[46] R. L. Sani, J. Shen, and P. M. Gresho. Pressure boundary condition for the time-dependent incompressible Navier–Stokes equations. *International Journal for Numerical Methods in Fluids*, 50(6):673–682, 2006.

[47] P. Sharif-Kashani. *Biomechanics of Vitreous Gel.* PhD thesis, University of California Los Angeles, 2012.

[48] P. Sharif-Kashani, J. P. Hubschman, D. Sassoon, and H. P. Kavehpour. Rheology of the vitreous gel: Effects of macromolecule organization on the viscoelastic properties. *Journal of Biomechanics*, 44(3):419–423, 2011.

[49] O. K. Smith. Eigenvalues of a symmetric 3×3 matrix. *Communications of the ACM*, 4(4):168–168, 1961.

[50] A. Sohankar, C. Norberg, and L. Davidson. Low-reynolds-number flow around a square cylinder at incidence: study of blockage, onset of vortex shedding and outlet boundary condition. *International Journal for Numerical Methods in Fluids*, 25(1):39–56, 1998.

[51] C. Taylor, J. Rance, and J. O. Medwell. A note on the imposition of traction boundary conditions when using the FEM for solving incompressible flow problems. *Communications in Applied Numerical Methods*, 1(3):113–121, 1985.

[52] Z. Tomic, N. Jadidi Gili, and I. Theocharis. Comparison between 25-gauge and 23-gauge sutureless vitrectomy techniques. *Retina Today*, 4(1), 2007.

[53] Y. H. Tseng and J. H. Ferziger. A ghost-cell immersed boundary method for flow in complex geometry. *Journal of Computational Physics*, 192(2):593–623, 2003.

[54] C. H. K. Williamson. Vortex dynamics in the cylinder wake. *Annual Review of Fluid Mechanics*, 28:477–539, 1996.

[55] J. Yang and E. Balaras. An embedded-boundary formulation for large-eddy simulation of turbulent flows interacting with moving boundaries. *Journal of Computational Physics*, 215(1):12–40, 2006.

[56] J. Y. Yoo and H. C. Choi. On the steady simple shear flows of the one-mode giesekus fluid. *Rheologica Acta*, 28(1):13–24, 1989.

[57] Y. Zang, R. L. Street, and J. R. Koseff. A non-staggered grid, fractional step method for time-dependent incompressible navier-stokes equations in curvilinear coordinates. *Journal of Computational Physics*, 114(1):18–33, 1994.